# ANNEALING OF COLD ROLLED AND SWAGED AZ31 MAGNESIUM ALLOY

A THESIS SUBMITTED TO
THE GRADUATE SCHOOL OF NATURAL AND APPLIED SCIENCES
OF
MIDDLE EAST TECHNICAL UNIVERSITY

BY

BENSU TUNCA

IN PARTIAL FULFILLMENT OF THE REQUIREMENTS
FOR
THE DEGREE OF MASTER OF SCIENCE
IN
METALLURGICAL AND MATERIALS ENGINEERING

NOVEMBER 2014

Approval of the thesis:

**ANNEALING OF COLD ROLLED AND SWAGED AZ31 MAGNESIUM ALLOY**

submitted by **BENSU TUNCA** in partial fulfillment of the requirements for the degree of **Master of Science in Metallurgical and Materials Engineering Department, Middle East Technical University** by,

Prof. Dr. Gülbin Dural Ünver _____
Dean, Graduate School of **Natural and Applied Sciences**

Prof. Dr. C. Hakan Gür _____
Head of Department, **Metallurgical and Materials Engineering**

Prof. Dr. Şakir Bor _____
Supervisor, **Metallurgical and Materials Engineering Dept. METU**

**Examining Committee Members:**

Prof. Dr. Şakir Bor _____
Metallurgical and Materials Eng. Dept., METU

Assoc. Prof. Dr. Arcan Fehmi Dericioğlu _____
Metallurgical and Materials Eng. Dept., METU

Assoc. Prof. Dr. Y. Eren Kalay _____
Metallurgical and Materials Eng. Dept., METU

Assist. Prof. Dr. Mert Efe _____
Metallurgical and Materials Eng. Dept., METU

Dr. Kaan Pehlivanoğlu _____
Advanced Material Technologies Div.
TÜBİTAK - SAGE

**Date:** 21.11.2014

**I hereby declare that all information in this document has been obtained and presented in accordance with academic rules and ethical conduct. I also declare that, as required by these rules and conduct, I have fully cited and referenced all material and results that are not original to this work.**

Name, Last name : Bensu Tunca

Signature :

# ABSTRACT

ANNEALING OF COLD ROLLED AND SWAGED AZ31 MAGNESIUM ALLOY

Tunca, Bensu
MS., Metallurgical and Materials Engineering
Supervisor: Prof. Dr. Şakir Bor

November 2014, 122 pages

Magnesium alloys are extensively used in electronics, automotive and aerospace industries due to their low densities and high specific strengths; however limited deformability of magnesium alloys at room temperature restricts the applications. Grain refinement as a result of recrystallization can be used to enhance the deformability of these alloys. In this dissertation, recrystallization behavior of cold rolled and swaged AZ31 alloy is investigated at different temperatures in the range of 100°C - 300°C. Effects of unidirectional and complex deformation modes on recrystallization behavior and microstructure development were studied. Microstructural analyses consisted of the examination of the grain structure and twinned regions by using optical and scanning electron microscopes. The volume fraction of recrystallized grains is determined by quantitative analysis methods and supported by the micro hardness measurements. X-Ray Diffraction method is used for texture analysis.

**Keywords:** AZ31, annealing, cold rolling, swaging, recrystallization.

# ÖZ

AZ31 MAGNEZYUM ALAŞIMININ SOĞUK HADDELEME VE RADYAL DÖVME SONRASI TAVLANMASI

Tunca, Bensu
Yüksek Lisans,Metalurji ve Malzeme Mühendisliği Bölümü
Tez Yöneticisi: Prof.Dr. Şakir Bor

Kasım 2014, 122 sayfa

Magnezyum alaşımları düşük yoğunlukları ve yüksek özgül dayançları sebebiyle elektronik, otomotiv ve havacılık sektörlerinde sıklıkla kullanılmaktadırlar. Oda sıcaklığında sahip oldukları sınırlı deforme edilebilirlikleri sebebi ile kullamı çeşitli uygulamalar ile sınırlıdır. Yeniden kristallenme ile tane boyutu inceltme methodu AZ31'in şekillendirilebilirliğini arttırmak amacı ile kullanılabilir. Bu tez kapsamında yapılan çalışmalarda AZ31'in soğuk haddeleme ve radyal dövme sonrası 100°C - 300°C sıcaklık aralığında tavlama işlemleri ile yeniden kristallenme davranışı incelenmiştir. Haddeleme ile sağlanan deformasyon ile radyal dövme ile sağlanan karmaşık deformasyonun malzemenin yeniden kristallenme davranışına olan etkisi gözlemlenmiştir. İçyapı analizleri optik ve taramalı elektron mikroskopu ile ile yapılmış, tane boyutu ve ikizleme yapılarındaki farklılıklar takip edilmiştir. Kristallenme oranları mikroyapı görüntülerinden elde edilen nicel analizler ile belirlenmiş, mikro sertlik ölçümleri ile desteklenmiştir. Doku incelemeleri için X-Işını Kırınım analizleri yapılmıştır.

**Anahtar Kelimeler:** AZ31, tavlama, soğuk haddeleme, radyal dövme, yeniden kristallenme.

**To my family,**

# ACKNOWLEDGEMENTS

I would like to express my deepest appreciation to Prof. Dr. Şakir BOR for his supervision, guidance, support and patience throughout the study.

I am grateful to Assoc. Prof. Dr. Arcan DERİCİOĞLU, Assist Prof Dr. İpek NAKAŞ and Assist Prof. Dr. Ziya ESEN for their continuous supports. I owe many thanks to Assist. Prof. Dr. Mert EFE and Dr. Kaan PEHLİVANOĞLU for their advices and comments.

I would like to thank Dr. Elif TARHAN BOR for her guidance, support and efforts throughout the study.

I would like to thank all the staff of the Department of Metallurgical and Materials Engineering and everyone for their effort and help.

I would specially thank to my lab mates and friends Emin Erkan AŞIK, Aylin GÜNEŞ, Ezgi BÜTEV and to Bilge SÜRÜN and many other friends for their support.

I am grateful to Çağatay ALTINTAŞ, Şensu TUNCA and to my parents and grandparents for their endless support, encouragements and love.

# TABLE OF CONTENTS

# LIST OF TABLES

# LIST OF FIGURES

# CHAPTER 1

# INTRODUCTION

As a necessity of today's world, where resources are running out, many researchers are focusing on new energy sources and more efficient ways for energy utilization. While studies on energy sources and storage technologies continues, ways to substitute conventional materials with lightweight materials for weight reduction and fuel efficiency purposes are also on going. Magnesium as a lightweight metal is considered as a promising element to replace its rivals in many structural applications especially in transportation industry. Weight reduction, fuel efficiency and reduced carbon monoxide emissions are the goals of many researchers, however there are difficulties preventing common usage of magnesium alloys in industry.

When the utilization of magnesium in the world is considered, it is seen that most of the magnesium produced is used as an alloying element for aluminum based alloys [1]. Cast and wrought applications follows as the second common usage area and smaller percentages are used for other applications, including desulfurization of iron and steel. Within the structural applications almost more than 99% of the utilization of magnesium and its alloys is through casting and only the remaining small percentage represents the utilization of wrought alloys [2]. Examples of cast magnesium alloy applications can be given as gearboxes, seat and steering wheel frames, door and roof frames, wheels and transmission cases in automotive industry and mobile phone, camera and notebook casings in electronics industry [1]. High

castability, high specific strength, good heat dissipation and electromagnetic shielding properties are some of the many important properties of magnesium alloys that promote their usage. Examples for wrought magnesium alloy applications are rather limited compared to castings, due to higher costs of wrought magnesium alloys and difficulties in their forming processes. Some examples of wrought alloy applications can be given as hoods, door inner panels and consoles in automobiles [1].

Main reason of the limitations in the usage of wrought magnesium alloys in structural applications is their poor formability and insufficient strength. The most common strengthening methods used are recrystallization for grain size and texture control. More research in this field is necessary to develop low cost alloys with better mechanical properties.

While there are many promising Mg-RE alloys that have the necessary mechanical properties for certain applications, high costs of magnesium and particularly the rare earth elements is a hindering factor for the common usage of such alloys. Without the usage of rare earth elements, magnesium alloys are considered as insufficient in terms of yield strength expectations for many structural applications. From the industrial perspective, they have not yet reached the level to substitute aluminum alloys in terms of both mechanical properties and cost [2].

In order to increase the mechanical properties such as formability and strength of magnesium alloys without alloying with rare earth elements, focus of this and many other studies is on the conventional metallurgical processes that can give strength to magnesium through recrystallization and grain refinement methods.

Being the most common wrought alloy [3], AZ31 was selected for the studies of this dissertation. This alloy belongs to ‘AZ’ group of alloys where ‘A’ stands for aluminum and ‘Z’ stands for Zinc with weight percentages 3% and 1% respectively. AZ31 alloy suffers from the most common problems of magnesium alloys, such as low deformability at room temperature and corrosion. In this study, in order to

increase the formability of AZ31, priority was given to understanding its deformation mechanism and successive annealing processes in order to control grain size. Due to limited deformability of HCP structured magnesium, effects of different modes of deformation and the annealed structures were examined. Rolling, a rather simple mode of deformation, and swaging, a more complex mode of deformation were selected and their effects on the deformability and microstructure were investigated. Preferential sites for nucleation upon annealing and kinetics of recrystallization were examined considering the effects of different deformation methods like rolling and swaging. Findings were used to develop a more efficient method to obtain fine grained material to increase the maximum deformation limit to fracture.

# CHAPTER 2

# THEORETICAL BACKGROUND

## 2.1.Magnesium and Magnesium Alloys

Magnesium is a light weight element with a density of 1.74 g/cm$^3$ and has high specific strength, good heat dissipation, damping and electromagnetic shielding properties [4-6]. In addition, magnesium is the most abundant light metal available on earth. It is the most abundant fifth element in ocean and eighth in earth's crust. It is produced either by reducing the oxide compounds with processes like pidgeon process or by electrolysis of saline water [7].

Apart from its favorable properties, it has low corrosion resistance, poor formability at room temperature and low creep resistance at high temperature [4,8]. Due to its low corrosion resistance, application areas of magnesium alloys in automotive industry is limited to the interior parts. Corrosion occurs by the dissolution of $Mg^{2+}$ ions and then $Mg(OH)_2$ forms which is an oxide that is only stable at certain conditions, at pH values above 10.5, in other situations oxide layer is porous and not protective.

Magnesium alloys in use can be separated into two groups, as the cast and wrought alloys. Cast magnesium alloys are commonly preferred due to their excellent fluidity and high castability to difficult or thin walled geometries. They represent the highest

portion in the industry. Applications of cast magnesium alloys started with their usage in engines, crank cases and housings. However, as the performance expectations from powertrain components increased, so did the operation temperatures and loads to levels that existing alloys cannot bear. As a result, applications in structural powertrain components in automobile industry almost completely stopped for a while [9]. As new alloys developed, such as AZ91 or AM60, magnesium prices became unfavorable for its further usage. Today many research is ongoing, expanding the usage of magnesium alloys to automobile interior (seat frames, steering wheels, etc.), body parts (door, roof frames etc.), chassis (racing wheels, brake pedal brackets etc.) and powertrain (engine block, transmission cases etc.) components [1]. Application areas of magnesium alloys in the field of aerospace are limited to non-structural parts due to corrosion problem, however being recyclable, good in vibration dampening, easily machinable and good in magnetic shielding these alloys are commonly used in portable electronics.

### 2.2. AZ31 Magnesium Alloy

AZ31 (3wt%Al-1wt%Zn-Mg) is one of the most common wrought alloy. It is a single phase alloy above around 200°C, under which $Mg_{17}Al_{12}$ precipitation can be observed. Commercial alloys may contain manganese which causes Al-Mn precipitations. At high temperatures these precipitates create pinning effect and retard the grain growth. Phase diagram is given in Figure 2.1.

a)

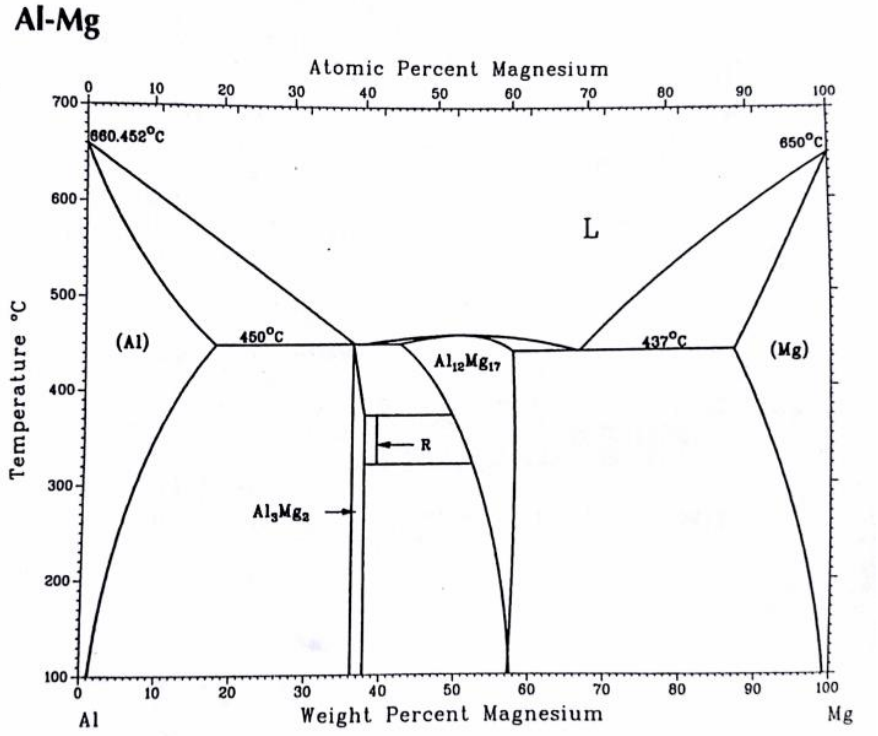


b)

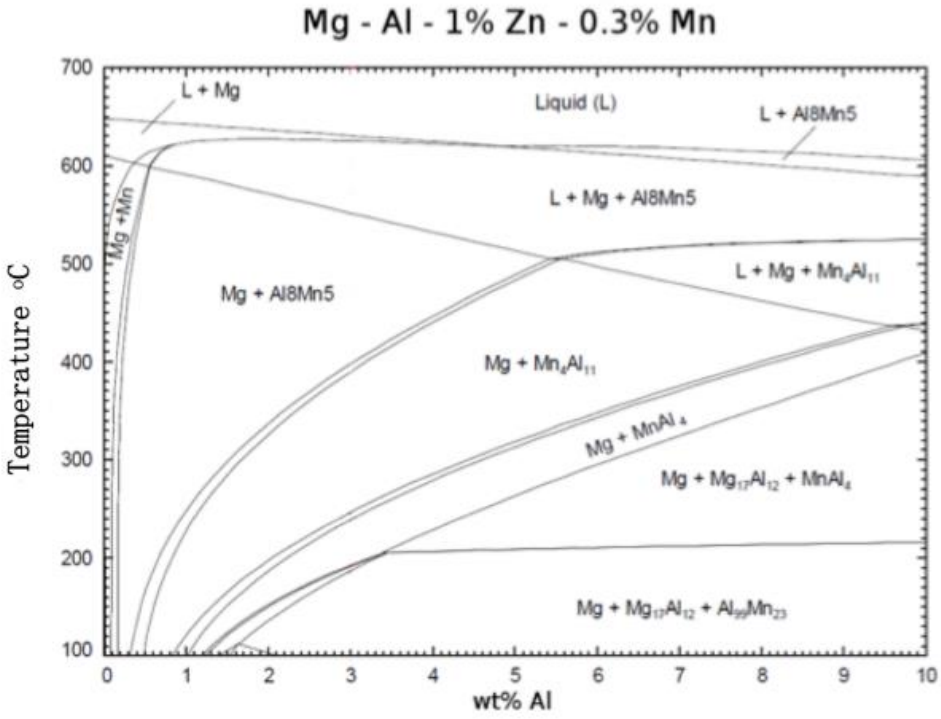


**Figure 2.1** Binary phase diagram for Mg-Al [10, 11].

## 2.3. Deformation of AZ31

Slip and mechanical twinning are the most common deformation mechanisms in magnesium alloy and shear banding is visible after larger deformation values. The most common slip and twinning mechanisms in Mg are basal, pyramidal, prismatic slip and extension and contraction twinning. Activity of each system depends on its critical resolved shear stress (CRSS), texture/orientation of grains under load and Schmid factor (m).

Equations 2.1 and 2.2 for CRSS and Schmid factor 'm' can be referred to the schematic Figure 2.2,

$$\sigma_{0.2} = \left(\frac{1}{m}\right) \tau_{CRSS} \quad \text{.....(2.1)}$$

$$m = \cos\alpha . \cos\theta \quad \text{.....(2.2)}$$

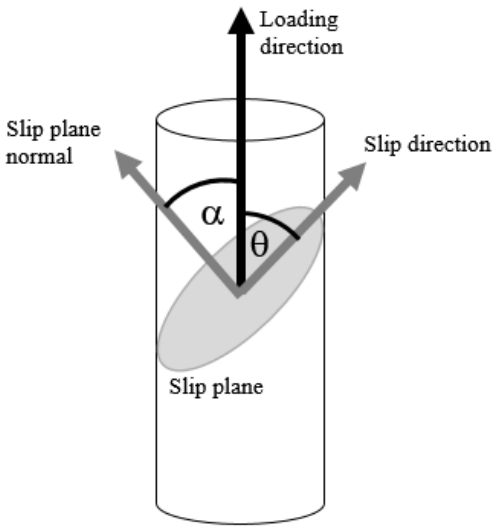


**Figure 2.2** Schematic drawing showing the angular relationships for the determination of Schmid factor "m".

In equation 2.1, $\sigma_{0.2}$ is the stress that needs to be applied to reach the critical resolved shear stress $\tau_{CRSS}$ of a certain deformation mechanism. In equation 2.2 'm' value is the Schmid factor, $\alpha$ is the angle between loading direction and slip plane normal, $\theta$ is the angle between loading direction and slip direction. Schmid factor states the geometrical relation between applied load and available system.

When the resolved shear stress component of the force applied on a crystal or grain reaches the critical resolved stress value (CRSS) of that particular slip/twin system, deformation starts. Deformation systems with the smaller CRSS values are easier to activate in general because they are the systems that require the least stress for dislocation glide. An activated or mobile deformation mechanism may get saturated after a while and a new deformation mechanism with relatively higher CRSS can also contribute to the deformation process. This process continues till the applied stress can activate enough mechanisms to compensate necessary changes and strain.

### 2.3.1. Slip Systems

Magnesium has four slip mechanisms: <a> slip on basal {0001}, prismatic {10-10} and pyramidal {10-11} planes and <a+c> slip in again pyramidal planes, as in Figure 2.3 and Table 2.1. <a> and <a+c> correspond to operative burgers vectors. Due to geometrical availabilities basal and prismatic slip system have three variants while others have six variants.

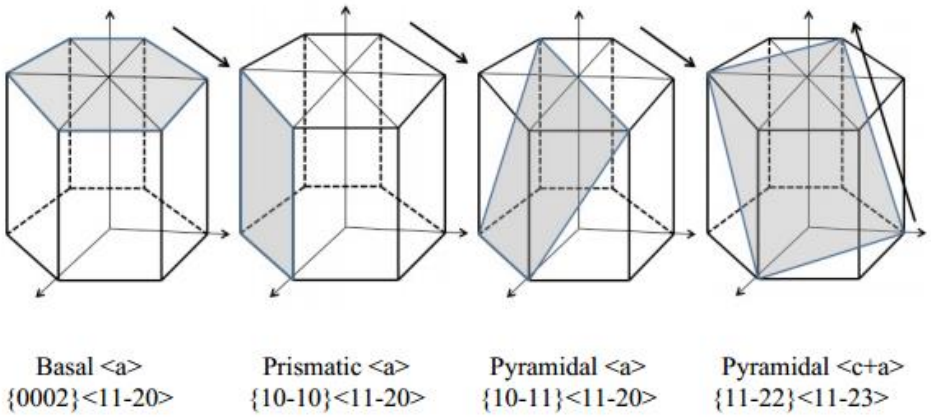


**Figure 2.3** Basal, prismatic and two pyramidal slip systems in magnesium [12].

**Table 2.1**: Slip systems of Magnesium [13].

| | | | | | |
|---|---|---|---|---|---|
| ( 0 0 0 1 ) | [ 2 -1 -1 0 ] | Basal <a> | ( 1 0 -1 0 ) | [ -1 2 -1 0 ] | Prismatic <a> |
| ( 0 0 0 1 ) | [ -1 2 -1 0 ] | | ( 0 -1 1 0 ) | [ 2 -1 -1 0 ] | |
| ( 0 0 0 1 ) | [ -1 -1 2 0 ] | | ( -1 1 0 0 ) | [ -1 -1 2 0 ] | |
| ( 1 -1 0 1 ) | [ 1 1 -2 0 ] | Pyramidal <a> | ( 1 1 -2 2 ) | [ -1 -1 2 3 ] | Pyramidal <c+a> |
| ( 1 0 -1 1 ) | [ -1 2 -1 0 ] | | ( 1 -2 1 2 ) | [ -1 2 1 3 ] | |
| ( 0 1 -1 1 ) | [ -2 1 1 0 ] | | ( -1 2 -1 2 ) | [ 1 -2 1 3 ] | |
| ( -1 1 0 1 ) | [ -1 -1 2 0 ] | | ( 2 -1 -1 2 ) | [ -2 1 1 3 ] | |
| ( -1 0 1 1 ) | [ 1 -2 1 0 ] | | ( -2 1 1 2 ) | [ 2 -1 -1 3 ] | |
| ( 0 -1 1 1 ) | [ 2 -1 -1 0 ] | | ( -1 -1 2 2 ) | [ 1 1 -2 3 ] | |

### 2.3.2. Twinning

Mechanical twinning is important for the deformation of magnesium and its alloys. They have two twinning modes called as extension and contraction twinning according to their effect on c axis. As shown in Figure 2.4, extension/tension twins occur on {10-12} planes and cause extension along the c axis while contraction twins occur on {10-11} planes and cause contraction. Shape of contraction twins are known to be more like a lens shape.

Both twinning mechanisms have six variants and shear does not operate in two directions reversibly as it is expected in regular slip mechanism. Possible twin systems are given in Table 2.2.

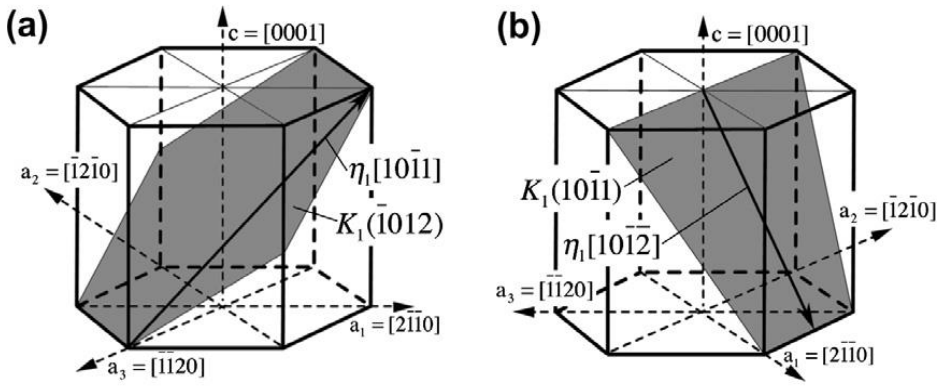


**Figure 2.4** Twinning systems in magnesium a) extension b) contraction twinning [14].

**Table 2.2** Twinning Systems in Magnesium [13].

| | Plane | Direction | | Plane | Direction |
|---|---|---|---|---|---|
| | (10-12) | [-1011] | | (1-101) | [1-102] |
| | (01-12) | [0-111] | | (10-11) | [10-1-2] |
| Extension | (-1102) | [1-101] | Contraction | (01-11) | [01-1-2] |
| Twinning | (-1012) | [10-11] | Twinning | (-1101) | [-110-2] |
| | (0-112) | [01-11] | | (-1011) | [-101-2] |
| | (1-102) | [-1101] | | (0-111) | [0-11-2] |

Studies show that during cold rolling of the samples at room temperature twins appear at the initial stages and as the deformation increases, amount of twining also increases [15]. Increasing temperature and decreasing strain rates are factors that prevent twinning [16-20].

Grain size of the material is also important for twinning in the sense that larger grain size promotes twinning. It was found that twinning is not observed in magnesium with grain sizes less than 1 μm [21].

Twinning can compensate the lack of sufficient number of active slip systems especially for c-axis deformation. The orientation of the twinned regions changes by 86.3° in extension twins and 56° in contraction twins. The change in the orientation

of these twinned regions creates opportunity for further slip. Twins are known with their ability to offer new and independent modes for deformation in cases where there is a lack of independent slip system [22]. During the deformation of magnesium {10.1} contraction twins and {10.1}-{10.2} double twins orient themselves to orientations that are more favorable for <a> slip on basal planes than the matrix they formed in. As a result, twins themselves deform to a great extent and there may be incompabilities between the highly deformed twin and the other parts of the grain. This behavior was interpreted as the reason of shear fractures occurring on the planes parallel to thin twin bands of {10.1} contraction twins and {10.1}-{10.2} double twins, which were more commonly found in coarse grain samples [23-27]. Apart from the effect of twinning on ductility, for a long while it was also a debate subject whether twins can be associated with fracture [22].

As a general approximation, at room temperature magnesium alloys' deformation limit to failure is about 10% elongation even though they do not satisfy the von Misses criterion. Although HCP crystal structure of magnesium alloys have limited active slip systems, less than that is required to preserve integrity along grain boundaries, twinning mostly compensates this lack of slip systems.

### 2.3.3. Shear Banding

Shear bands are localized regions with relatively more intense shear levels. In rolling these bands appear at approximately 35° to the rolling plane and parallel to the transverse direction [12]. Generation of shear bands was found not to increase the ductility of the material; but it was also observed that shear bands were the first sites to crack. Figure 2.7 shows the shear banding after 10% thickness reduction in pure Mg sample. Shear band generation may not be prevented at high strains but it can be delayed by applying multi-axial deformation and by creating more homogeneous microstructure [28, 29]. With this purpose a deformation method like swaging was selected in the present study to see the effect of multidirectional deformation.

In literature non-homogeneous microstructure and shear banding was observed in samples with 22% reduction [15]. After 22% reduction, crack initiations were observed and interpreted as the result of shear bands. The reason of the shear band formation was explained as the secondary {10-12} twinning of former {10-11} twins and fine recrystallized grain formation was noted in these shear bands [30].

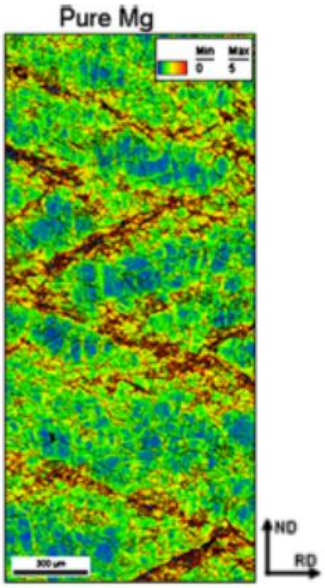


**Figure 2.5** Shear bands after cold rolling to 10% thickness reduction [31].

In samples rolled to 16% reduction the (0002) pole intensity was at its peak value since the (0002) planes of most of the grains become parallel to the rolling plane. Schmid factor for basal slip in those grains become nearly zero, which makes further deformation difficult with the existing basal slip, yet the deformation continues which is taken as a result of fine grains formed in shear bands. Normally being a difficult process, pyramidal <c+a> slip was seen to become possible as the grain size decreases in magnesium [32].

### 2.3.4. Critical Resolved Shear Stress in Magnesium

Critical resolved shear stress values of AZ31 and magnesium, gathered from literature in the study of Hutchinson and Barnett [33] are given in Table 2.3 and

more examples on relative CRSS ratios from literature are given in Figure 2.6. Temperature dependency of CRSS values can also be seen in Figure 2.7.

As can be seen in Figure 2.7, at room temperature CRSS value of basal slip is much lower than prismatic <a> or pyramidal <c+a> slip. These values indicate that basal slip at room temperature is the dominant deformation mechanism and it is followed by the twinning mechanism. Other slip systems are relatively difficult to get activated. After the basal slip system gets saturated, extension twinning and then non-basal slip systems step in.

**Table 2.3** Slip CRSS values measured for single-crystal and estimated for polycrystal magnesium alloy AZ31 [33].

| | CRSS Values in Mpa | | |
|---|---|---|---|
| Material | Basal <a> | Prismatic <a> | References |
| AZ31 Polycrystal | 45 | 110 | [34] |
| AZ31 Polycrystal | 10 | 55 | [35] |
| AZ31 Polycrystal | 20 | 90 | [36] |
| AZ31 Polycrystal | 30 | 90 | [37] |
| AZ31 | 50 | 100 | [38] |

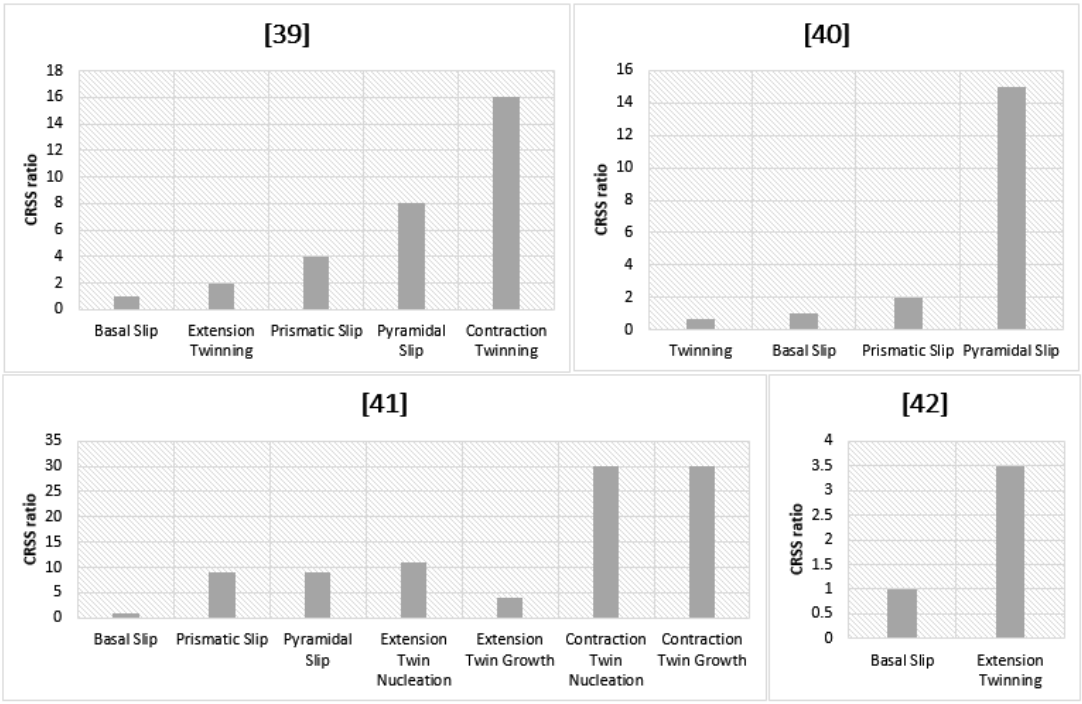


**Figure 2.6** Ratio of CRSS values with respect to basal slip from different studies conducted on magnesium [39-42].

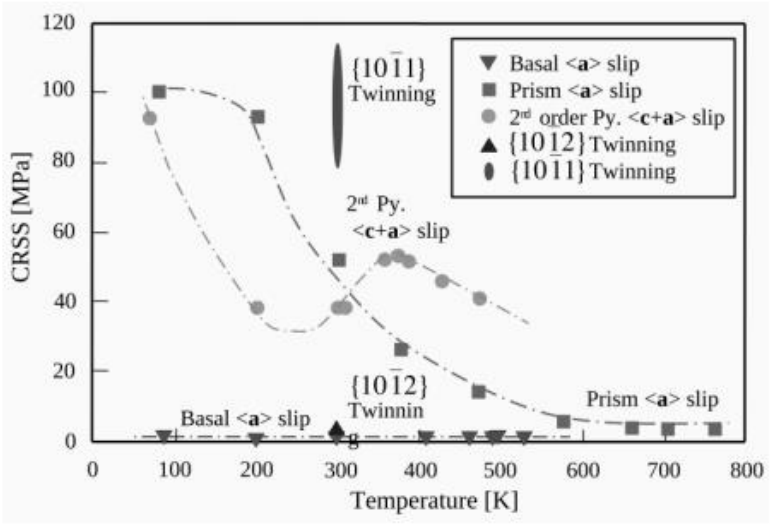


**Figure 2.7** CRSS values plotted against temperature, showing the active slip systems in Mg [43].

While the data in Table 2.3, Figure 2.6 and 2.7 give an idea about the sequence of the deformation process based on relative and actual CRSS values of each mechanism, texture is also important to understand which mechanism is actually possible. Even if the CRSS value of a system is low, that does not mean that, that particular system will be active in each grain throughout the sample. For a system to be mobile the texture/orientation of the grain should be geometrically suitable to generate the required stress component (CRSS) of the main load acting on the material. Schmid factor is useful in determining the potential mechanism according to the loading condition and the texture of the material. As the Schmid factor increases, necessary load to reach CRSS decreases. In a case where 'm' is zero no stress under given conditions can activate that mechanism.

Texture data of the samples are highly important in order to understand the deformation behavior of magnesium under stress, whether it is being compressed as in rolling or exposed to complex stress states as in radial forging processes. If the texture of the material is precisely known, Schmid factors for crystals under different loading conditions can be calculated. These calculated Schmid factors can be used to explain which deformation mechanisms can be activated when a sample with a known texture is being deformed under a known direction of load. Calculated Schmid Factors for the deformation mechanisms of magnesium are given in Figure 2.8 [13], where $\theta$ is the angle between loading direction and c axis and $\lambda$ is the angle between loading direction and $a_1$, which is <2-110> . In that study while $\theta$ was varried in the range 0 to 90, $\lambda$ values where taken as 0°, 15° and 30° creating stresses like $\sigma_1$, $\sigma_2$ and $\sigma_3$, as in Figure 2.8.a,. Schmid factors of (a) basal <a>, (b) prismatic <a>, (c) pyramidal <a> and (d) pyramidal <c+a> slips and (e) extension and (f) contraction twinning as a function of the angles ($\theta$) between the c-axis and the loading directions are also shown

When deformation caused by slip is being considered, absolute values of the Schmid factors in Figure 2.8.b,c,d and e can be taken into consideration since slip mechanism can work in two directions. Twins on the other hand are polar

mechanisms which work in only one direction. When θ is zero or close, <a> slip is does not get activated and extension twins can operate only if the applied forces are in tension. But when applied forces are in compression, as in the case for rolling an already (basal) textured as received sample, pyramidal <a+c> and contraction twinning (m=0.415) can be activated.

In table 2.4. all the schmid factors shown in Figure 2.8 were tabulated by Nan et.al, [13] and the maximum Schmid factors are written in bold.

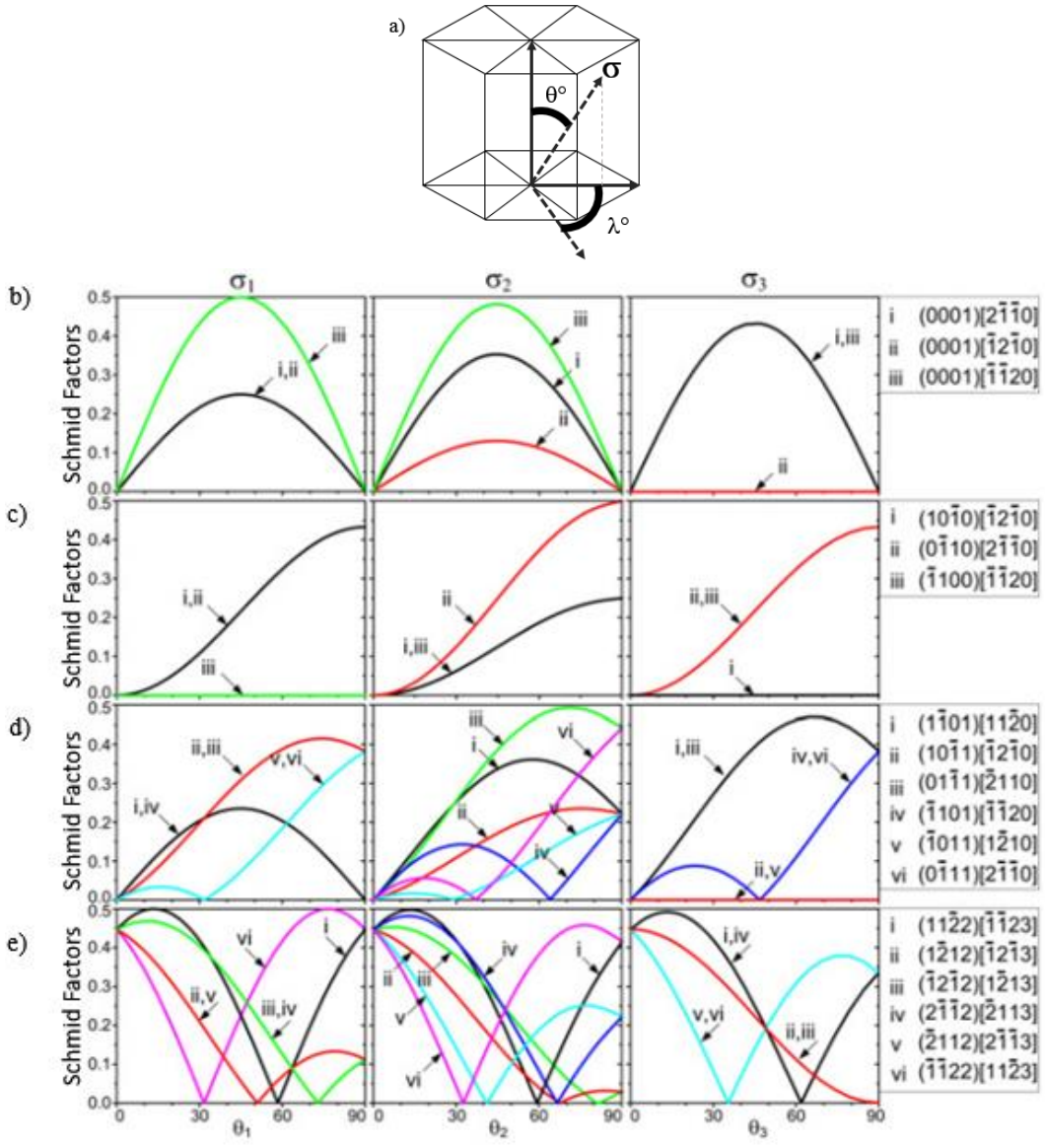


**Figure 2.8** (Continued)

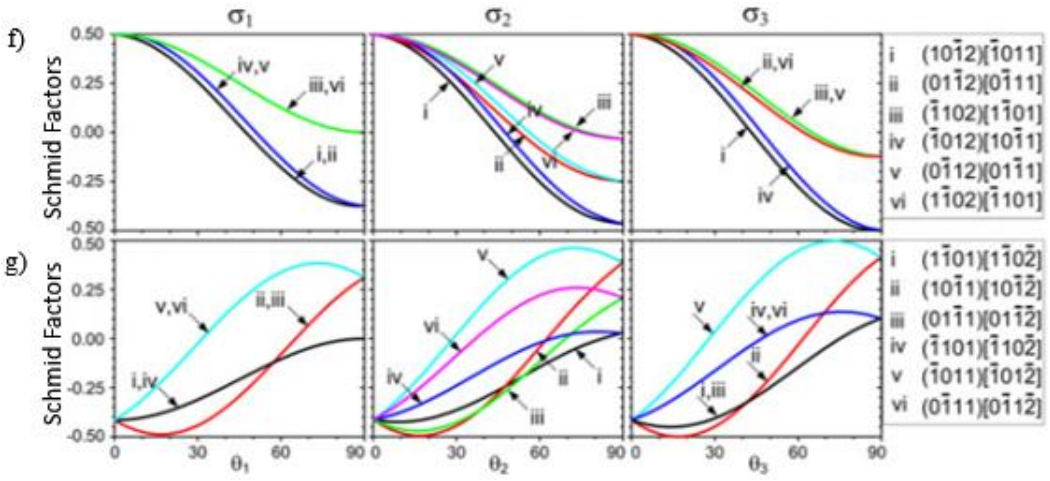


**Figure 2.8** Calculated Schmid factors for θ in the range 0 to 90 degrees and λ=0, 15 and 30° creating stresses like $\sigma_1$, $\sigma_2$ and $\sigma_3$, as in (a). Schmid factors of (a) basal <a>, (b) prismatic <a>, (c) pyramidal <a> and (d) pyramidal <c+a> slips and (e) extension and (f) contraction twinning as a function of the angles (θ) between the c-axis and the loading directions [13].

**Table 2.4** The highest m values in three basal <a> and prismatic <a> or six pyramidal <a>, pyramidal <a+c>, (10-12) extension twinning and (10-11) contraction twinning variants upon loading from three directions ($\sigma_1, \sigma_2, \sigma_3$), with angles between the c-axis and loading directions varying from 0 to 90° [13].

| $\theta$ (°) | Basal ⟨a⟩ | | | Prismatic ⟨a⟩ | | | Pyramidal ⟨a⟩ | | | Pyramidal ⟨c + a⟩ | | | Extension twinning | | | Contraction twinning | | |
|---|---|---|---|---|---|---|---|---|---|---|---|---|---|---|---|---|---|---|
| | $\sigma_1$ | $\sigma_2$ | $\sigma_3$ | $\sigma_1$ | $\sigma_2$ | $\sigma_3$ | $\sigma_1$ | $\sigma_2$ | $\sigma_3$ | $\sigma_1$ | $\sigma_2$ | $\sigma_3$ | $\sigma_1$ | $\sigma_2$ | $\sigma_3$ | $\sigma_1$ | $\sigma_2$ | $\sigma_3$ |
| 0 | 0 | 0 | 0 | 0 | 0 | 0 | 0 | 0 | 0 | 0.447 | 0.447 | 0.447 | **0.499*** | **0.499*** | **0.499*** | | | |
| 5 | 0.087 | 0.083 | 0.075 | 0.003 | 0.004 | 0.003 | 0.041 | 0.041 | 0.383 | 0.479 | 0.478 | 0.474 | 0.495 | 0.497 | 0.497 | | | |
| 10 | 0.171 | 0.165 | 0.148 | 0.013 | 0.015 | 0.013 | 0.080 | 0.084 | 0.081 | **0.497*** | **0.495*** | **0.490*** | 0.484 | 0.486 | 0.486 | | | |
| 20 | 0.322 | 0.311 | 0.278 | 0.051 | 0.058 | 0.051 | 0.151 | 0.172 | 0.175 | 0.487 | 0.485 | 0.480 | 0.441 | 0.442 | 0.436 | | | |
| 30 | 0.433 | 0.418 | 0.375 | 0.108 | 0.125 | 0.108 | 0.204 | 0.254 | 0.272 | 0.418 | 0.419 | 0.420 | 0.374 | 0.373 | 0.357 | | 0.019 | 0.034 |
| 40 | 0.492 | 0.475 | 0.426 | 0.179 | 0.207 | 0.179 | 0.274 | 0.346 | 0.358 | 0.327 | 0.327 | 0.316 | 0.293 | 0.287 | 0.257 | 0.122 | 0.181 | 0.202 |
| 45 | **0.5*** | **0.483*** | **0.433*** | 0.217 | 0.250 | 0.217 | 0.309 | 0.387 | 0.395 | 0.280 | 0.271 | 0.251 | 0.249 | 0.241 | 0.203 | 0.189 | 0.255 | 0.278 |
| 50 | 0.492 | 0.475 | 0.426 | 0.254 | 0.293 | 0.254 | 0.340 | 0.423 | 0.425 | 0.300 | 0.274 | 0.204 | 0.206 | 0.195 | 0.149 | 0.249 | 0.321 | 0.346 |
| 60 | 0.433 | 0.418 | 0.375 | 0.325 | 0.375 | 0.325 | 0.388 | 0.475 | 0.463 | 0.418 | 0.389 | 0.308 | 0.125 | 0.107 | 0.045 | 0.339 | 0.420 | 0.449 |
| 70 | 0.322 | 0.311 | 0.278 | 0.382 | 0.442 | 0.382 | **0.413*** | **0.497*** | **0.468*** | 0.487 | 0.455 | 0.369 | 0.058 | 0.034 | | **0.382*** | **0.467*** | **0.497*** |
| 80 | 0.171 | 0.165 | 0.148 | 0.420 | 0.485 | 0.420 | 0.411 | 0.485 | 0.440 | **0.497*** | **0.465*** | **0.378*** | 0.015 | | | 0.372 | 0.455 | 0.485 |
| 85 | 0.087 | 0.083 | 0.075 | 0.430 | 0.496 | 0.430 | 0.400 | 0.466 | 0.414 | 0.479 | 0.448 | 0.363 | 0.004 | | | 0.348 | 0.428 | 0.457 |
| 90 | 0 | 0 | 0 | **0.433*** | **0.5*** | **0.433*** | 0.382 | 0.441 | 0.382 | 0.447 | 0.417 | 0.335 | 0 | | | 0.311 | 0.387 | 0.415 |

Values in bold type with "*" are the highest $m_1$ values.

### 2.3.5. Progress of Deformation

To simply cover the deformation of magnesium, progress of different mechanisms can be summarized as shown in schematic Figure 2.9: at room temperature first the basal slip starts, at a strain level close to 0.1%, twinning steps in and further deformation continues with their simultaneous action [44-48]. After a short period of time basal slip saturates while twinning is still operating. It is noted that when the Schmid factor for non-basal slip systems becomes 1.5-2 times that of basal slip, both types of slip system can operate collectively. When the dislocations in a severely deformed AZ31 with 8 μm grain size was examined, it was seen that approximately 40% of the dislocations were non-basal [49]. This can be related to the necessity to preserve the continuity along the grain boundaries. In order to compensate the strain and not to cause a separation at the grain boundaries, together with basal slip systems operating, non-basal dislocations were also observed. Figure 2.10 schematically explains this necessity. During their TEM studies, Kobayashi et al. revealed substantial dislocation activity on non-basal planes in a 2% elongated sample [50].

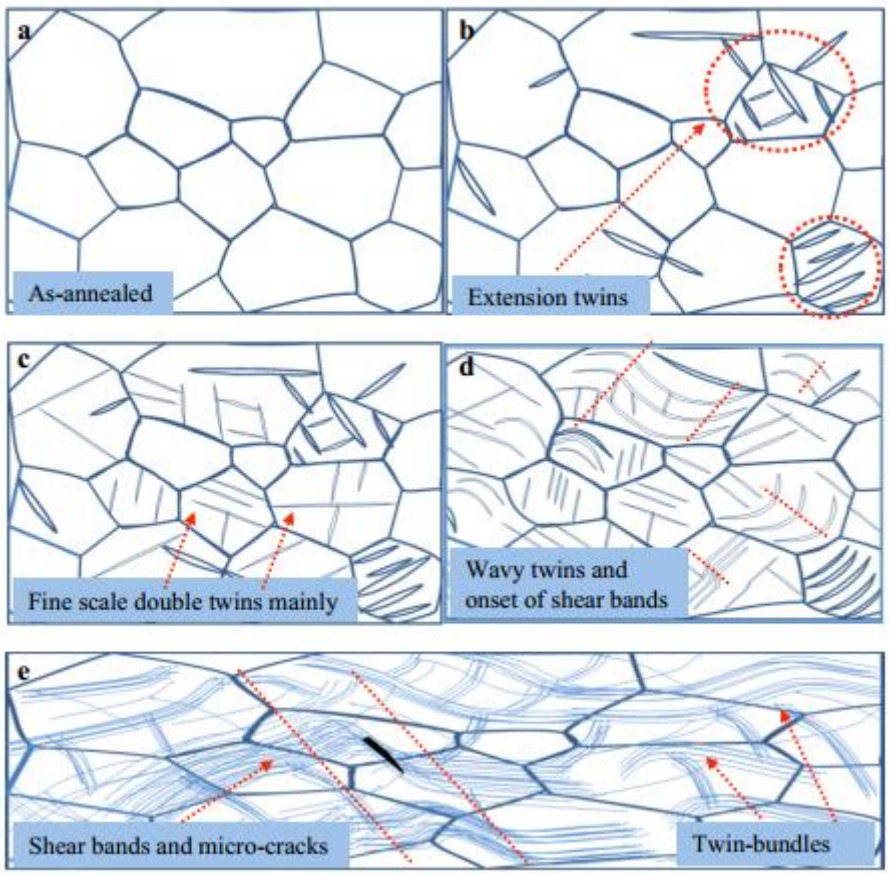


**Figure 2.9** Schematic illustration of progress of deformation in AZ31 [12].

According to the findings of the study of Brown et al. [44], 42% of the deformation was provided by the twinning activity, when the deformation in the parent structure was only 14% and when the matrix was deformed by 14%, 80% of the volume was already comprised by twinned regions.

It was also confirmed by other researchers that, by the time matrix reaches an 8% deformation, twins got saturated [46, 51, 17]. Some of the twinned areas correspond to hard orientations for further slip, and they only deform elastically, but some of the twins correspond to favorable orientations for further non basal slip (which requires higher CRSS) and also for secondary twinning [45, 46].

In their study on compression of extruded AZ31, Clausen et.al, predicted the relative deformation contribution of different mechanisms as shown in Figure 2.11, where the thick dashed lines are for the parent grains and the thin solid lines are for the twin grains [52].

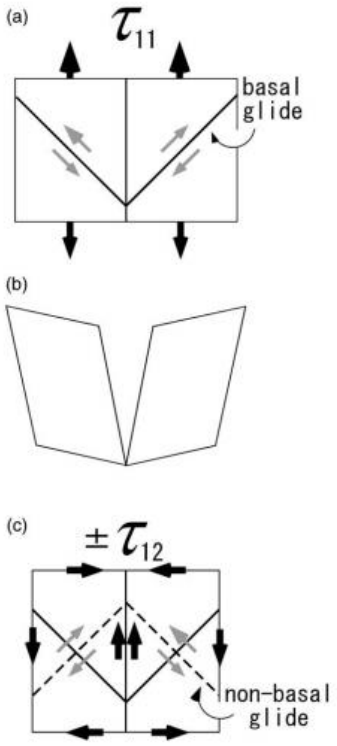


**Figure 2.10** Schematic drawing of two crystals under stress: a) before deformation, b) deformed condition without bonding at the grain boundary, c) possible stress state to maintain contact between two grains [16].

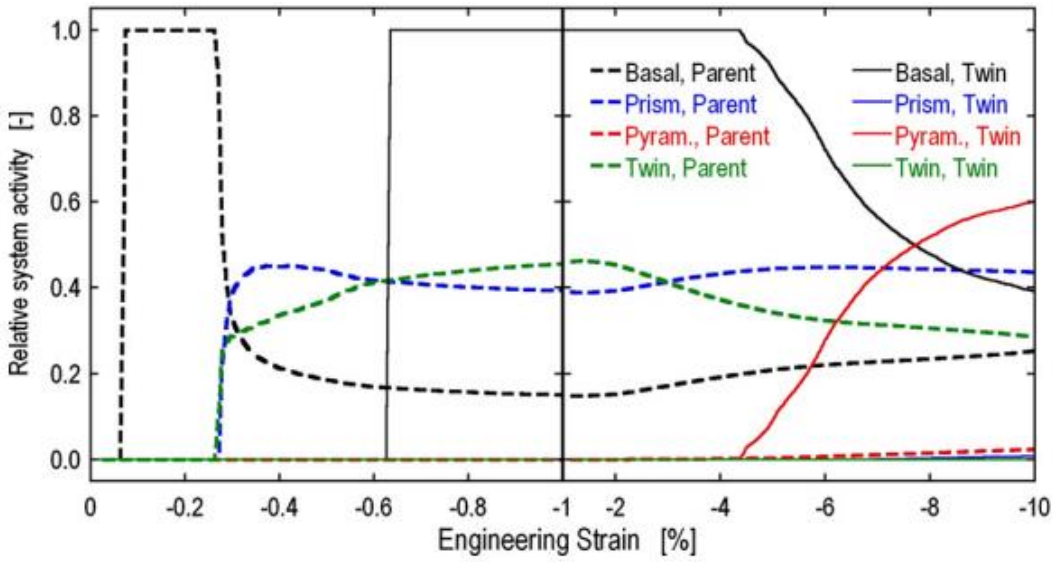


**Figure 2.11** Predicted relative system activity during compression of an extruded AZ31 according to the model by Clausen [52]. The thick dashed lines are for the parent grains and the thin solid lines are for the twin grains. Note the bi-linear strain axis; the first half of the plots highlights the initial range from 0% to 1% strain, and the last half of the plots show the range from 1% to 10% strain.

## 2.4.Grain Size and Its Effects on Deformation

Both slip and twin mechanisms are highly dependent on grain size. It was proposed that grain boundaries contain geometrically necessary dislocations to accommodate the plastic incompatibility generated between distinctly oriented grains [53]. While the interior parts of the grains deforms by relatively easier mechanisms (low CRSS), the grain boundary regions require harder mechanisms to be activated. Studies in which non-basal slip was only observed around grain boundaries of pure magnesium support this model [54]. TEM studies of AZ31 alloys also reveal that non basal slip was noticed at the grain boundary regions [49]. Grain size dependency of hard mechanisms is more prominent than it is for easy slip mechanisms. As a result, it is expected to see that the basal slip operation is more dominant in coarse grained magnesium.

Hall Petch equation which relates the yield strength to grain size, is given in Equation 2.3 where $\sigma_y$ is the yield strength, $\sigma_0$ is the strength required to move a dislocation, $k$ is the strengthening coefficient (material constant) and d is the grain diameter. Yielding results from the combination of many deformation mechanisms and those deformation mechanisms show different dependencies to grain size. Determination of the Hall Petch slope does not clarify the relation of each distinct mechanism and grain size, it rather gives the relation of grain size and the combined effect of many deformation mechanisms [55]. The yielding behavior and the rate of yielding is controlled by the hardest mechanism; in the case of deformation of magnesium this rate controlling mechanism was prismatic slip, since it requires higher CRSS [35, 36].

$$\sigma_y = \sigma_0 + \frac{k}{\sqrt{d}} \quad \text{.....(2.3)}$$

Twinning also depends on the grain size of the material, studies show that as the grain size increases twin volume fraction also increases upon deformation [55]. This relation between twinning mechanisms and grain size was also mentioned in other studies [21], in which as the grain size of the magnesium alloy decreases, so does the twinning as it is more dependent on the grain size. This behavior can also be seen in the Hall-Petch relation as well. To satisfy this relation two k factors might be necessary. In magnesium alloys yield strength versus 1/d plots show a transition since twinning is not active in fine grains and thus deformation mechanism changes as grain size change [56, 57].

However, Hall Petch studies conducted over a grain size regime of 13 to 140 μm revealed that one single slope fits well to the Hall Petch plot of yielded AZ31 and authors concluded that grain size in 13-140 μm range does not affect the relative activities of deformation mechanism much. Probably the difference in the slopes can be seen when smaller grained samples are included to studies. In literature, 1 μm grain size was given as the threshold grain size for twinning since no record of twinning observation below that limit size exists [12]. In addition to above findings,

it was also observed that above 30 μm grain size ductility of samples decreased severely [55].

In order to increase the deformability of magnesium, two methods that can be applied are elevated temperature forming and grain size control. Grain refinement is an effective method to improve mechanical properties. It was seen that reducing the grain size of extruded AZ31 from 22 μm to 3 μm doubled the compressive yield strength [23].

The most common method of grain refinement in magnesium and its alloys is the dynamic recrystallization (DR) during hot deformation [58]. For DR, process temperature is an important parameter which directly affects the activity of slip systems. Magnesium and its low stacking fault energy (SFE) enables easy DR resulting in fine and equiaxed grains [59]. With DR during hot deformation 3-5 μm sized grains were achievable [60], however some researchers also highlighted that any subsequent annealing or slow cooling after hot deformation may cause grain growth which may deteriorate the mechanical properties [61-65]. In the present study in order to better control or monitor grain growth cold deforming and subsequent annealing procedures were applied.

### 2.5. Recrystallization of AZ31

Recrystallization being an effective method to control grain size can be divided into two types: static and dynamic recrystallization. The term static recrystallization is used when deformation and recrystallization occurs separately and dynamic recrystallization refers to cases when these two processes occur simultaneously.

Stacking fault energy of a slip system is important in determining the recrystallization behavior of a material. When the SFE values are high as it is in aluminum alloys, recovery process is possible. Dislocations do not dissociate into partials which create stacking faults and become less mobile; instead they move and rearrange to form cellular like subgrain structure which then promotes nucleation of

new strain-free grains during the recrystallization process. This situation, in which both recovery and recrystallization occurs together is called as Continuous Recrystallization. Cases where SFEs are low and recovery stage is hindered are called as Discontinuous Recrystallization.

SFEs of magnesium depends on many parameters including temperature and solute content. But in general studies show that SFE of basal slip system is lower than those of prismatic and pyramidal slip systems (Table 2.5).

Due to the variation of SFE in magnesium with deformation mechanism, recovery and recrystallization behavior of magnesium also has a variation. In situations where deformation is mainly by basal slip one can expect to have stacking faults since it requires lower energy and thus easy to form. As a result rearrangement of dislocations or defects to reduce the stored deformation energy might not be possible due to immobile stacking faults and recovery may not be observed.

**Table 2.5** Stacking fault energies of magnesium in mJ/m2.

| **Planes** | **SFE values in mJ/m$^2$** | | | | | | |
|---|---|---|---|---|---|---|---|
| Basal | 44 | 36 | 34 | 140 | 32 | 78 | <50 |
| Prismatic (10-10) | | 265 | 354 | | 255 | | |
| Prismatic (11-20) | | | 1224 | 250 | | | |
| Pyramidal (10-11) | | 344 | 496 | | | | |
| Pyramidal (11-22) | | | 452 | 221 | | | |
| **Reference** | [66] | [67] | [68] | [69] | [70] | [71] | [72] |

For the cases where lots of non-basal slip are operating, one can expect to see conventional recovery and subgrain formation since dislocations are rather mobile and no stacking faults are formed. This variation in the behavior was also mentioned in literature, while recovery was stated as a step not commonly observed in certain studies [21]. Elsewhere it was stated that recovery was observed in the non-recrystallized regions and limited the growth of recrystallized nuclei [73]. These can be interpreted as the effect of deformation type on recrystallization through SFE.

Activity of slip/twin systems also affect the recovery or recrystallization of magnesium. While contraction twin boundaries are sinks for basal dislocations, extension twins are known to repel basal dislocations and create dislocation pile ups at extension twin boundaries. These dislocation pile ups lead to recovery and recrystallization especially in large grained structures. A micrograph as an example to recrystallization on a twin can be seen in Figure 2.12 [74]**,** and similar structures were also observed throughout the present study as well. Dislocation pile ups in the un-twinned matrix at the close vicinity of the extension twin boundaries also supply enough driving force for the twin boundary to be mobile and to be able to expand [75].

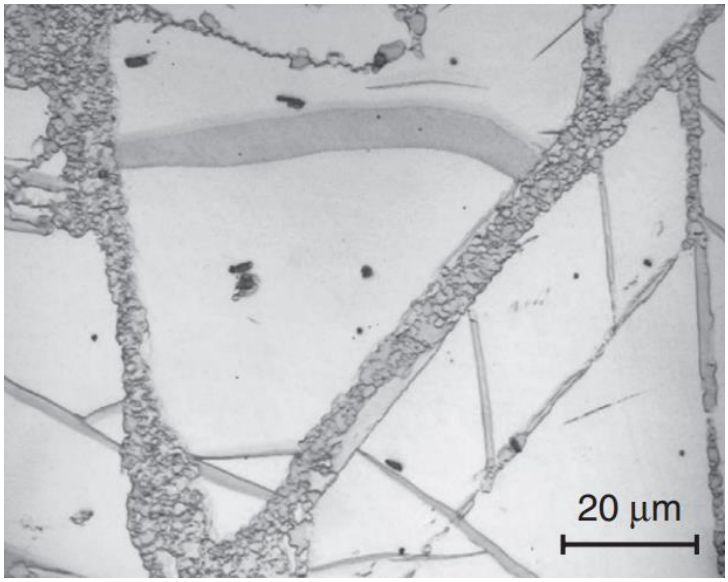


**Figure 2.12** Recrystallization along twin boundaries [74].

In the study conducted by Liang et. al. [73] AZ31 sheet specimens were cold rolled to 0.10 and 0.30 strains, annealed at 250°C and examined with EBSD. Nucleation was found to be highly heterogeneous due to the heterogeneities in the as-deformed microstructure. Preferential nucleation sites were given as twin/grain boundaries and twin/twin boundaries. At 0.30 strain nucleation was visible at grain boundaries and grain interiors as well. The aim of their study was to investigate the orientation of recrystallization nucleation and their role in the developing texture. However studies

reveal that recrystallization does not weaken the deformation texture to great extends.

### 2.6. Texture

Due to HCP crystal structure of magnesium and the lack of active slip systems at room temperature, magnesium alloys in general are processed at 250-300°C and at slow speeds [76]. When deformation is applied via rolling, this creates a strong texture with basal planes parallel to the rolling plane. However the grains with their basal plane parallel to rolling plane (ND) are randomly oriented with respect to rolling direction (RD) and transverse direction (TD), Figure 2.9 [77], which also shows that the initial basal texture is stronger in fine grain material than that in large grain size sample. After applying tension along rolling direction the only change observed is the slight increase of the basal texture.

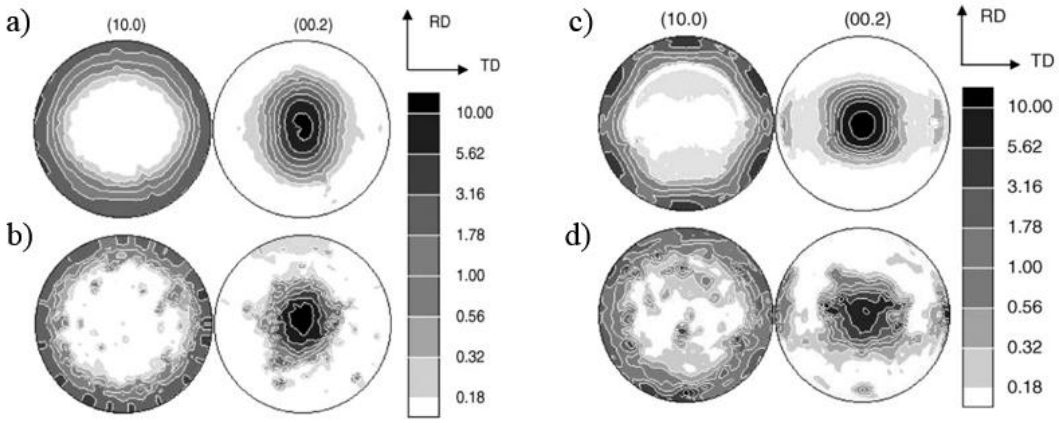


**Figure 2.13** Initial (a) , (b) and after applying tension along rolling direction (RD) (c) , (d) textures for sample with grain sizes (a), (c) 13 μm and (b), (d) 35 μm [77].

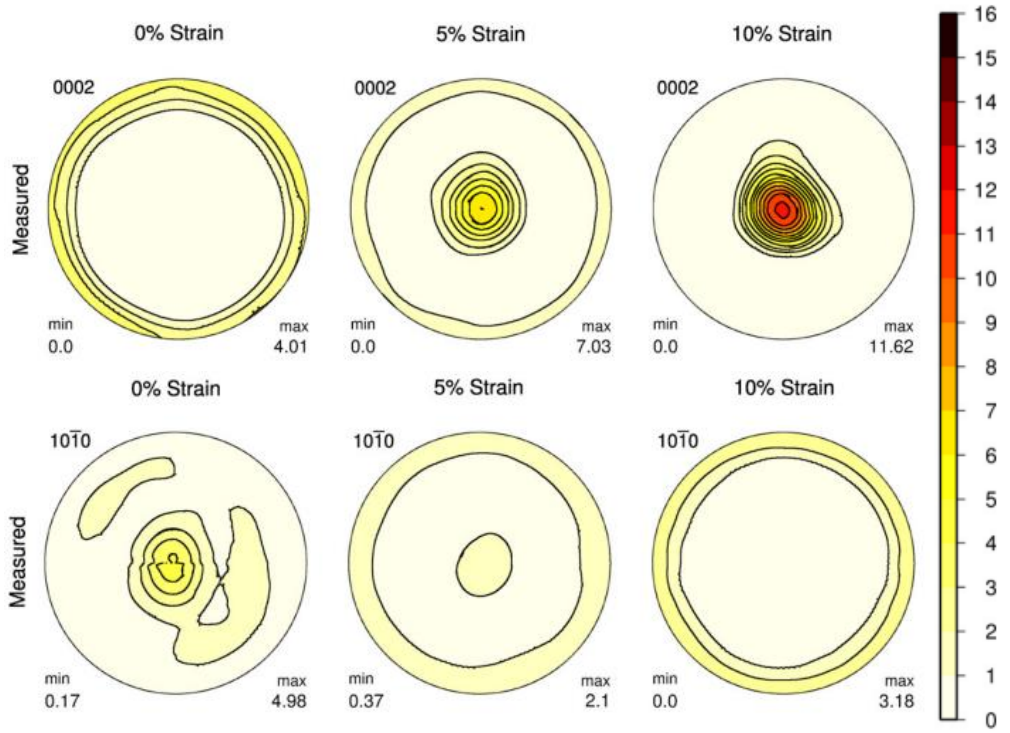


**Figure 2.14** [0002] and [10-10] pole figures for extruded AZ31 before (first row) and after (second row) compression tested by 0%, 5% and 10% along the extrusion direction [52].

During a study conducted by Gehrmann, AZ31 samples were deformed at temperatures below 200°C and it was shown that reducing the initial basal texture increases the ductility [79]. There are studies focusing on weakening of the strong deformation textures via static recrystallization. However, strong texture similar to that of deformation observed upon hot deformation was attributed to the subsequent straining of new grains that form during dynamic recrystallization which restore the deformation texture again [80].

In the previous sections, Schmid factor calculations from literature was given to predict most probable deformation modes during loading of a sample with known texture. The texture of the sample at the initial state changes as deformation mechanism gets activated. Especially twins are capable of changing the orientation extensively, rotating the areas in which they form. Since the texture continuously

changes during deformation, it is necessary to make Schmid factor calculations specific to these newly twinned and rotated areas in order to understand how these new orientations effect further deformation.

These rotated planes inside the twins can accommodate many slip and twin modes just as the un-twinned parent matrix does. Again, to understand which deformation modes are more probable, Schmid factor calculations can be done for the newly generated twin volumes. When the angular relationship between the twin and parent grain's coordinate system is known, one can calculate the physical transformation of crystallographic directions and planes after twinning. In the study of Niewczas [14], which is summarized in Appendix, to see the correspondence of directions and planes in the new, twinned slip/twin systems to the old coordinate system, transformation matrices for magnesium were calculated and used. The correspondence matrix method represents an essential tool in predicting the physical transformation of crystallographic directions and planes formed after twinning. For detailed information about transformation matrices one can refer to Niewczas's [14] work. Below Figure 2.15 shows a simple sketch of a rotated twinned region.

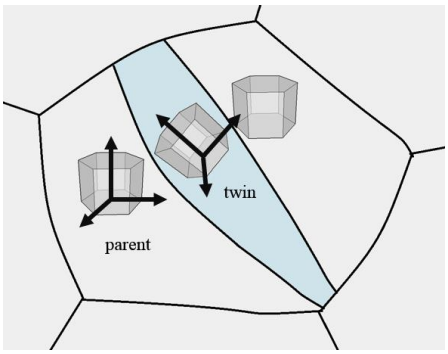


**Figure 2.15** Schematic illustration of the rotated crystal structure inside twin.

By using the re-indexation matrix which is also given in the work of Niewczas [14] one can calculate the correspondence of a known loading direction in terms of the twin notation. Due to the rotation of the twinned region, the angle between slip or twin plane normal and directions changes. Re-indexation matrix can be used to re-

index a known loading direction for twinned region and then with Schmid factor calculations of twinned regions, one can reveal the activity of successive deformation mechanism such as; slip inside a twin, or twin inside a twin so on.

# CHAPTER 3

# EXPERIMENTAL PROCEDURE

In the present study deformation and annealing response of AZ31 alloy subjected to two different types of room temperature deformation, namely rolling and swaging, is characterized. Annealing temperatures and times in the range of 100°C-300°C and 1 min to 20 days, respectively were covered. Microstructural examinations were done with the use of optical, polarized and scanning electron microscopy including quantitative analysis. Micro hardness measurements were taken from each sample produced. Chemical analysis were done with OES and EDS especially at the early stages of the study, mainly to characterize raw material, but repeated when believed necessary (after certain heat treatments). X-Ray Diffraction data was used to comment on texture.

## 3.1. Raw Material

7 mm thick AZ31 alloy sheets with a composition of 2.5wt% Al-1wt%Zn-Mg were used. AZ31 sheet was cut into strips with approximately 8 mm width. Early metallographic studies involved microstructure examination and micro hardness measurements of the as received samples. Three cross-sections were prepared and examined: cross-section perpendicular to the rolling direction, perpendicular to

transverse direction and the rolled surface. Optical and scanning electron microscopy studies and EDS analysis revealed that the alloy consisted of a single Mg alpha phase with equiaxed grains, Figure 3.1.

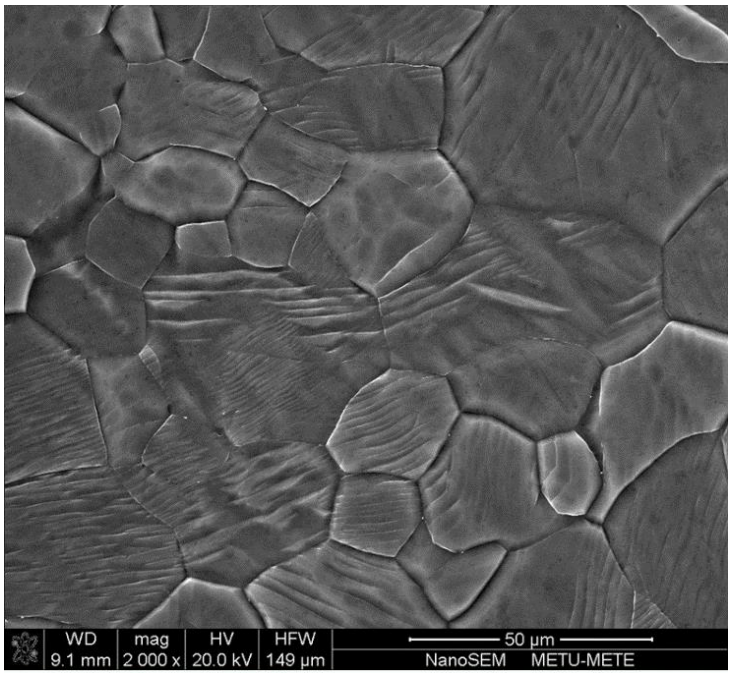


**Figure 3.1** Microstructure of the as received AZ31 alloy.

### 3.2. Chemical Analysis

Chemical analysis of the AZ31 sheets was performed by Optical Emission Spectroscopy (OES) and Energy-Dispersive X-ray Spectroscopy (EDS). OES examinations were conducted at Atılım University. EDS examinations were conducted in NOVA NanoSEM430 (FEI Company, OR, USA). Chemical analysis was done to as received samples prior to each deformation and annealing process.

### 3.3. Deformation Processes

#### 3.3.1. Rolling

As received AZ31 sheet cut to 7mm x 8mm x 185 mm pieces were rolled to various strains by 0.2 mm reduction in thickness at each pass. Strain values were recorded

in terms of both thickness reduction and also percent elongation. True strain values were calculated according to Equation 3.1.

$$\in = \boldsymbol{ln}\left(\frac{\boldsymbol{L}}{\boldsymbol{L_0}}\right) = \boldsymbol{ln}\left(\frac{\boldsymbol{A_0}}{\boldsymbol{A}}\right) \quad \text{.....(3.1)}$$

Where $\in$ is true strain, $L_0$ and L initial and final length, $A_0$ and A initial and final cross-section area. Samples were rolled to obtain 0.05, 0.1, 0.16, 0.22, 0.29, 0.36 true strain values.

### 3.3.2. Swaging

During room temperature swaging of the samples, a swager with 4 forging molds was used. Molds had a cylindrical cavity with diameters of 6 mm, 8.8mm, and 11 mm. Figure 3.2 shows the front view of a swager in which the samples are fed.

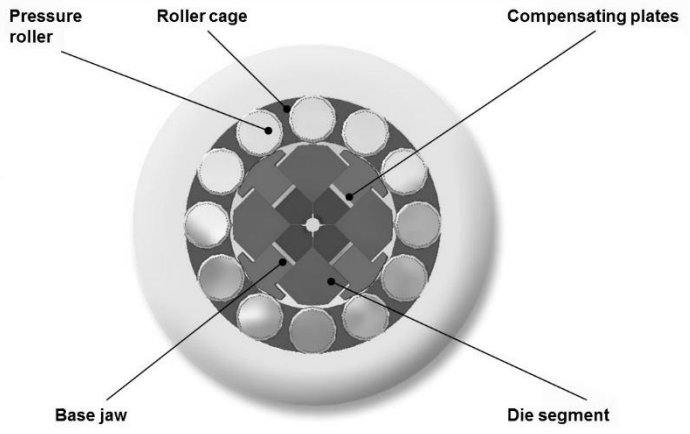


**Figure 3.2** Swaging with the mold cavity in the middle and the working mechanism [81].

Since the raw samples with square or rectangular cross-sections were not able to compensate the shape change generated during swaging, cracks were initiated and spalling was observed. As a result, raw samples cut from the sheets were turned to cylindrical forms prior to any swaging. Initial diameter, length and weight values of

the turned samples were recorded before deformation in order to calculate the resultant true strain.

During the swaging processes, heating was observed but not measured. Few seconds of air cooling was enough to hold the specimens.

Different from the regular rolling process, swaging offers a multi directional deformation as it can be seen from Figure 3.3. During swaging, the sample is held fixed with a claw, while forging molds rotate around it. In certain cases when the mold cavity dimensions were not suitable to obtain the desired strain values, samples were placed inside copper pipes and then swaged accordingly. This method enabled to achieve high strain levels but also resulted in cracking of samples. True strain values calculated according to Equation 3.1 were 0.1, 0.22, 0.63 and 0.69.

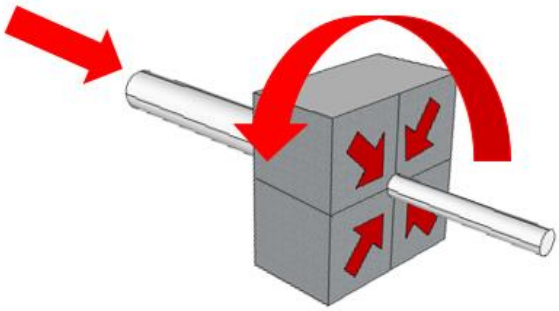

**Figure 3.3** Schematic swaging process.

### 3.4. Annealing

Deformed samples were cut into 3-4 mm thick slices with rolled ones having rectangular cross-sections and swaged ones having circular cross-sections. Cutting was done by a precision cutter at 3000 rpm, with a feed rate of 2 mm/min by using oil based coolant to prevent heating. For the efficient use of time, samples with different strain amounts were bundled with copper wires to form packages and exposed to the same heat treatment. Packages were placed in a furnace which is at

the target temperature. Each package/set was removed from the furnace at a different time, enabling each sample to represent unique conditions with different strain and time values. After the sample sets are removed from the furnace they are immediately water quenched. An illustration of general annealing procedure is given in Figure 3.4. Separate annealing treatments for certain specimens were applied when necessary. Annealing parameters are given in Table 3.1.

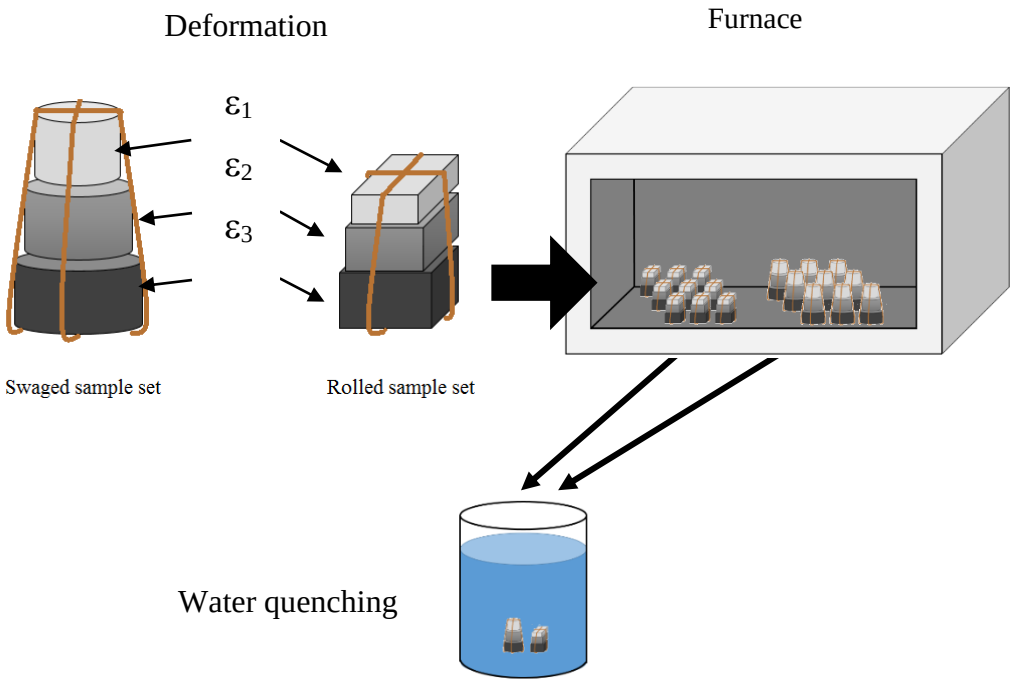


**Figure 3.4** Schematic illustration of annealing procedure for both swaged and rolled samples. Each pair of sample packages leaves the furnace at the same time.

**Table 3.1** Annealing parameters regardless of the deformation type.

| Temperature | 60 s | 100 s | 180 s | 200 s | 300 s | 400 s | 500 s | 600 s | 700 s | 800 s | 900 s | 1000 s | 1200 s | 1500 s | 1800 s | 2000 s | 3000 s | 1 h | 2 h | 6 h | 1 day | 2 day | 5 day | 10 day | 20 day |
|---|---|---|---|---|---|---|---|---|---|---|---|---|---|---|---|---|---|---|---|---|---|---|---|---|---|
| **100°C** | | | | | | | | | | | | | | | | | | | | | ✓ | ✓ | ✓ | | |
| **150°C** | | | | | | | | | | | | | | | | | | | | | ✓ | ✓ | | ✓ | ✓ |
| **185°C** | | ✓ | | ✓ | ✓ | ✓ | ✓ | | ✓ | ✓ | ✓ | ✓ | | | | ✓ | | | | | | | | | |
| **200°C** | | | ✓ | ✓ | ✓ | ✓ | | ✓ | ✓ | ✓ | ✓ | | ✓ | ✓ | ✓ | | ✓ | ✓ | ✓ | | | | | | |
| **220°C** | | ✓ | | ✓ | ✓ | ✓ | ✓ | ✓ | ✓ | ✓ | ✓ | ✓ | | ✓ | | ✓ | | | | | | | | | |
| **250°C** | ✓ | ✓ | ✓ | ✓ | ✓ | ✓ | ✓ | ✓ | ✓ | ✓ | ✓ | | | ✓ | ✓ | | | ✓ | ✓ | | | | | | |
| **300°C** | ✓ | ✓ | ✓ | ✓ | ✓ | ✓ | ✓ | ✓ | ✓ | ✓ | ✓ | ✓ | ✓ | | ✓ | ✓ | | ✓ | ✓ | ✓ | ✓ | | | | |

### 3.5. Cyclic Deformation and Annealing

Cyclic deformation and annealing processes are applied to rolled samples to clarify the nature of deformation and recrystallization. Room temperature rolling was applied by 0.2 mm thickness reduction in each pass starting from 7 mm sheet. After a certain amount of strain value is attained (Table 3.2), a piece is cut out from the as rolled sample with a precision cutter to represent the as rolled state. Remaining part of the ribbon was heat treated, annealing periods were as tabulated in Table 3.2. Samples were annealed with no atmosphere control and water quenched after the heat treatment.

Time and temperature for these annealing treatments are determined according to prior trials so that the grain growth does not become dominant and fine recrystallized grains can be preserved. A sample was cut from the recrystallized sample for examination. The whole procedure mentioned above was repeated to generate products of three more cycles (Figure 3.5). Microstructure and hardness of all as rolled and as recrystallized samples were examined.

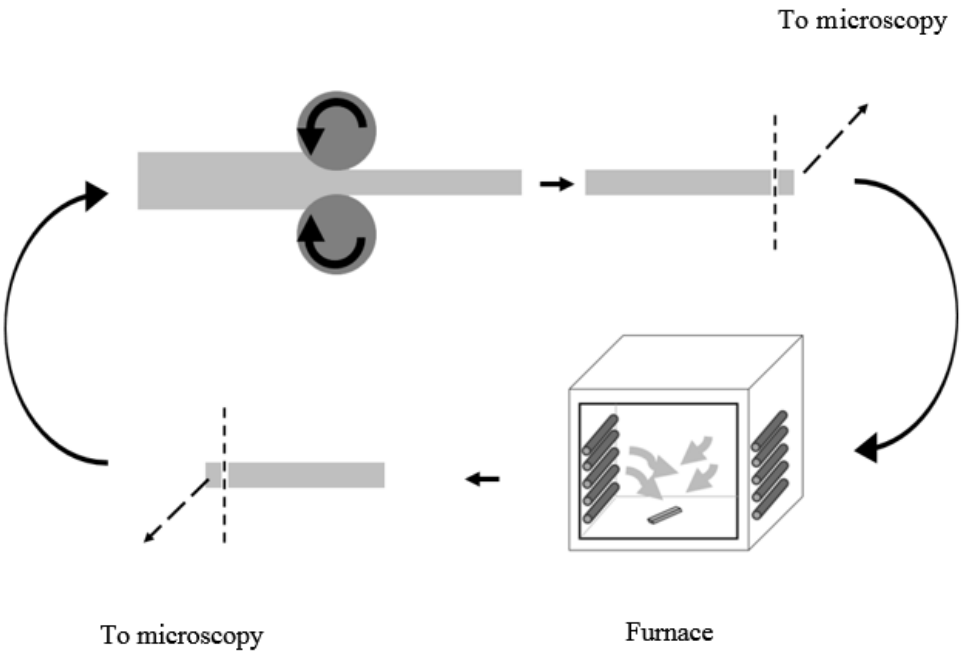


**Figure 3.5** Schematic sketch of one cycle of deformation and annealing.

**Table 3.2** Deformation and annealing parameters of cyclic recrystallization.

| **Cycle** | **1** | **2** | **3** | **4** |
|---|---|---|---|---|
| **True strain** | *0.18* | *0.1* | *0.1* | *0.08* |
| **Time at 200°C (min)** | *10* | *15* | *15* | *15* |

### 3.6. Sample Preparation for Optical and Scanning Electron Microscopy

For rolled samples; sections parallel to rolling direction and for swaged samples; section perpendicular to swaging axis were grinded with grit papers with grades ranging from 180 to 1200 and then polished using oil based diamond suspensions with 5, 3 and 1μm, respectively. 15-40 s of etching with acetic picral solution (4.2 g picric acid, 10 ml acetic acid, 70 ml ethanol, and 10 ml water) was applied as the final step. At the end of each step samples were cleaned with ethanol and dried.

For the SEM examination additional platinum or carbon coatings were applied when necessary due to the non-conducting nature of the mount material (Polyester).

### 3.7. Optical Microscopy Examinations

Optical microscopy examinations were performed on an OLYMPUS microscope equipped with a polarizer and an analyzer. For the image capture Motion Capture and Clemex software were used. Optical micrographs were used to measure grain size by line intercept method. Micrograph of a rolled and annealed sample is given in Figure 3.6.

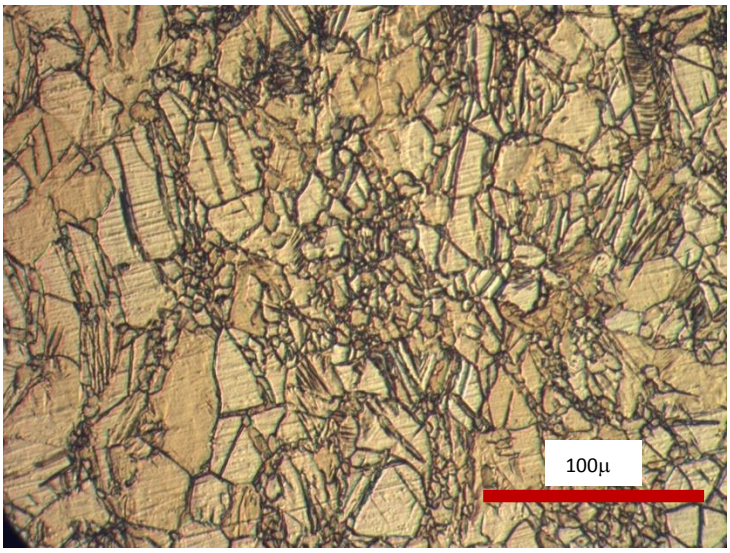


**Figure 3.6** Optical micrograph of 0.22 rolled sample annealed for 1 hr at 200°C.

Most of the examinations were done on the cross-section parallel to the rolling surface for the rolled samples to see the elongation of the grains after deformation and cross-section perpendicular to the swaging direction for the swaged samples (Figure 3.7).

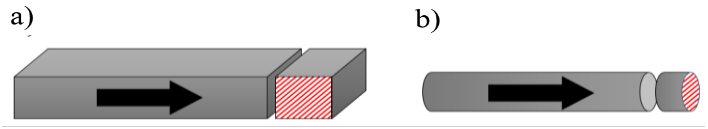


**Figure 3.7** Metallography and hardness examination surfaces for a) rolled, b) swaged samples.

### 3.8. Polarized Light Microscopy Examinations

Hexagonal closed packed structure and the resultant optical anisotropy of magnesium enabled the use of polarized microscopy with many benefits. Examinations were done before/after deformation and annealing processes. Colorful images were helpful in differentiating twinned areas or recently nucleated recrystallized grains. Figure 3.8 belongs to a swaged sample, twinned regions are easily differentiated and Figure 3.9 belongs to a sample which was rolled to 0.1 strain value and annealed at 220°C for approximately 33 minutes (2000 sec).

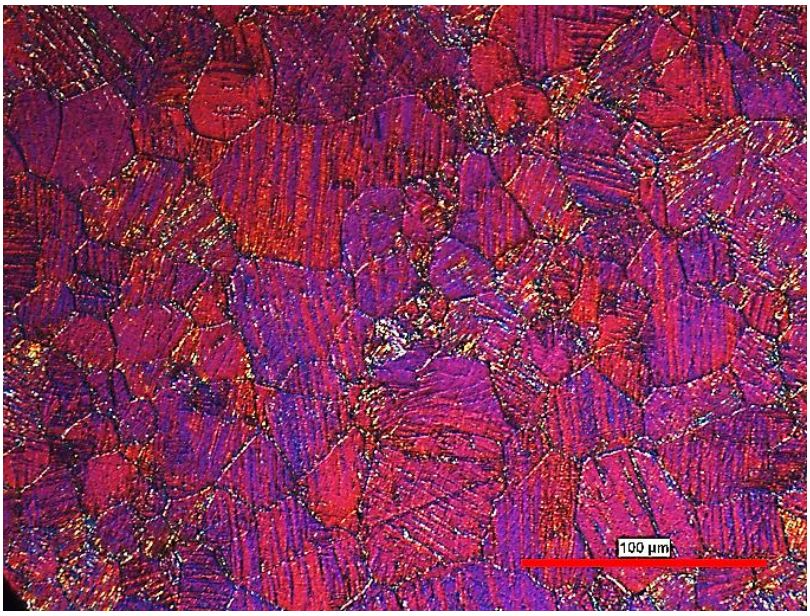


**Figure 3.8** Polarized microscopy image of a swaged sample.

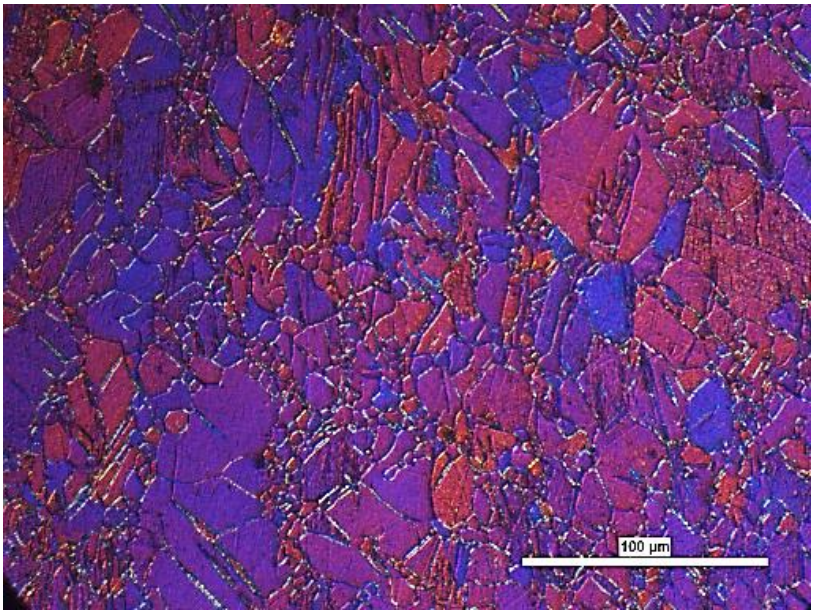


**Figure 3.9** Sample rolled to 0.1 strain value and annealed at 220°C for approximately 33 minutes (2000 sec).

### 3.9. Scanning Electron Microscopy

Scanning electron microscopy studies were performed on a NOVA NanoSEM430 (FEI Company, OR, USA) with 15 kV excitation voltage. In the examination of polyester mounted samples, platinum or carbon coating was sometimes applied to prevent charging and image vibrations. During SEM studies, EDS measurements were also taken in order to have an approximate chemical composition data.

SEM image of an as received AZ31 can be seen in Figure 3.10. SEM images were used for grain size determination with line intercept method and for recrystallization fraction measurements with point counting and area fraction calculation.

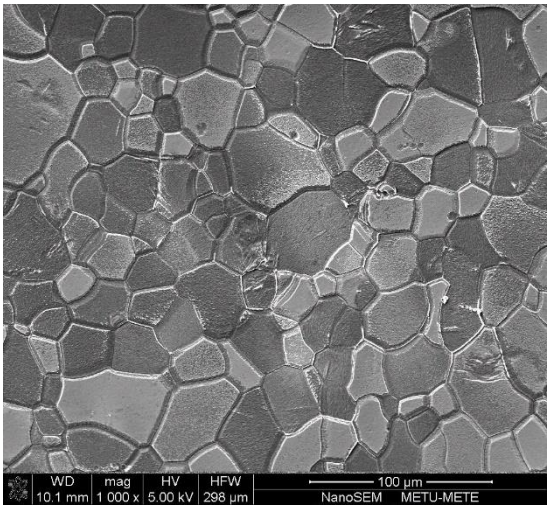


**Figure 3.10**. SEM micrograph of as received AZ31 alloy.

### 3.10X-Ray Diffraction Analysis

X-Ray diffraction analysis were conducted on Rigaku D/Max 220PC (Rigaku Corporation, Tokyo, Japan) diffractometer with 40 kV Cu Kα X-ray source. Continuous scans were performed between 30-90° with 2°/min scan rate.

### 3.11 Quantitative Analysis

Three methods were used for quantitative analysis of the microstructures: Line intercept method for grain size measurements, point counting and area fraction measurement for recrystallized fraction determination. Clemex and Image J softwares were used for these purposes and GIMP 2 software was used for image modifications.

For the grain size determinations done with line intercept method, grain count average of 20 lines were taken from each micrograph. For point counting, grids with 900-2970 points were used depending on the magnification of the micrographs which changed between 200X and 2000X. During point counting, recently recrystallized grains were counted until it was impossible to differentiate them from

the unrecrystallized matrix. Image analysis by area fraction calculations (using Image J Software) were done from time to time in order to check the results obtained from point counting. Area fractions were calculated by subtracting the unrecrystallized areas from the total area with the use of GIMP software. Since the results of the two methods were in accordance, point counting was preferred for its faster and easier application. Micrograph examples from point counting and image analyzing are given in Figure 3.11.

a) b)

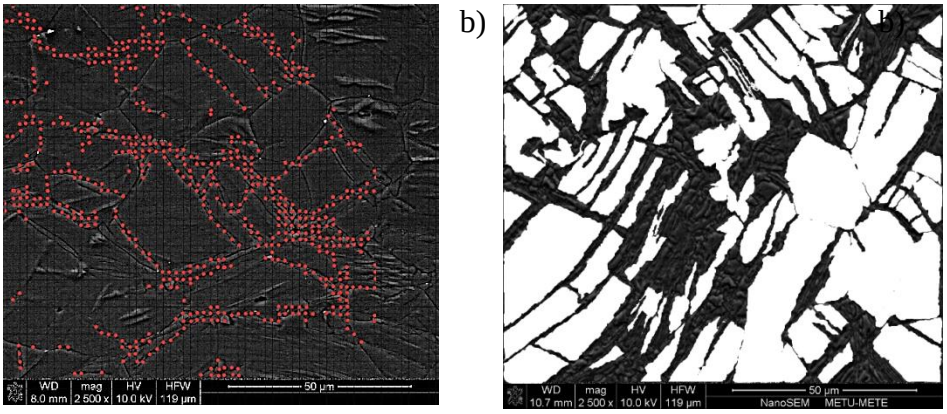


**Figure 3.11** Examples of application of a) point counting technique where the recrystallized regions are dotted, and b) image analysis in which the unrecrystallized regions are removed to calculate recrystallized area fraction.

### 3.12. Hardness Measurements

Since samples examined were of small size, the alloy was soft and grain size was rather small (less than 30μm), micro Vickers hardness testing was chosen for measuring hardness. Almost all examined samples, including as received, as received and annealed, deformed, deformed and annealed samples were hardness tested. Hardness measurements were taken from mounted samples, on polished and etched surfaces. Measurements taken from mounted or un-mounted samples were exactly the same. Etching prior to measurement was found to be advantageous for

relating the measured hardness value and the true microstructure under and around the indentation mark.

Hardness measurements were done by SHIMADZU HMV-2 (SHIMADZU Corporation, Tokyo, Japan) hardness tester. HV0.3 indentations were used with 300 grams of load and 10 seconds of indentation time. Indentations were applied to the same surface which was examined with optical and scanning electron microscopy formerly. For swaged samples a hardness change was noticed along the radius of the circular cross-section of the samples. This was taken as an indication of a non-uniform deformation and the relatively different strain hardening rate across the sample. In order to understand the effect of swaging in terms of non-uniform deformation and the related strain hardening differences, hardness measurements 0.5 mm apart were taken along the radius. Similar hardness data was also collected from the cyclic recrystallization and deformation sample sets. Softening of the recrystallized samples could be regarded as an approximate indication of the recrystallization fraction through the use of an equation given below.

$$Xh = \frac{\textit{Cold rolled hardness} - \textit{Recry. hardness}}{\textit{Cold rolled hardness} - \textit{Fully annealed hardness}} \quad \ldots\ldots\ldots\ldots\ldots\ldots\ldots\ldots (3.2)$$

To represent the fully annealed hardness value in the Equation 3.2, 48.2±2.9 value was used, which is the hardness value of a sample annealed at 400°C for 6 hours.

# CHAPTER 4

# RESULTS AND DISCUSSIONS

This chapter begins with the characterization of as received AZ31 sheet, covering the results of chemical, microstructural analysis and hardness measurements. Hardness and grain size measurements of annealed samples were given, in order to have a general understanding about samples' behavior under annealing prior to any deformation in terms of grain growth and softening. Following the raw material examinations, rolled samples were examined in the as deformed and as annealed states. Microstructure, hardness, recrystallization and texture data were collected. Parameters affecting the recrystallization was studied. Findings of the above mentioned studies were used for developing a method to obtain finer grain sized samples using the knowledge gained about preferential nucleation sites and kinetics of recrystallization.

After rolling, a more complex deformation method swaging and its effects on as deformed and annealed microstructure, micro hardness and recrystallization fraction were covered. Results of the examinations cover the effects of unidirectional versus multidirectional deformation, recrystallization of differently deformed or annealed AZ31 sheets and the reaction of AZ31 to cyclic recrystallization.

## 4.1. Raw material properties

### 4.1.1. Chemical composition

Chemical analysis were done to characterize the raw material, the as received AZ31. Optical Emission Spectroscopy (OES) and Energy-Dispersive X-ray Spectroscopy (EDS) results of the as received samples are given in Table 4.1. EDS analyses repeated during the SEM examinations of most samples gave the same compositional results, only in the samples annealed at 150°C for 10 days and 200°C for 10 minutes, increase in Zn wt% from 1.21 to 3.03 was observed.

**Table 4.1** EDS and OES results of AZ31 alloy.

| | **EDS** | **OES** |
|---|---|---|
| | wt% | wt% |
| **Aluminum** | 3.04 | 1.94 |
| **Zinc** | 1.21 | 0.9 |
| **Magnesium** | 95.75 | 97 |
| **Manganese** | - | 0.00358 |

### 4.1.2. Microstructure of the as received sample

As received AZ31 sheet (Figure 4.1) consisted of single phase equiaxed Mg ($\alpha$) alpha grains with approximate grain sizes of 20.9 ± 2.1 μm, 23.3 ± 1.4 μm and 24.7 ± 3.0 μm at rolled surface, surface perpendicular to transverse and rolling directions respectively.

Few twins were observed in the as received samples, origin of which might be the former sheet forming operations or the metallographic sample preparation operations like grinding.

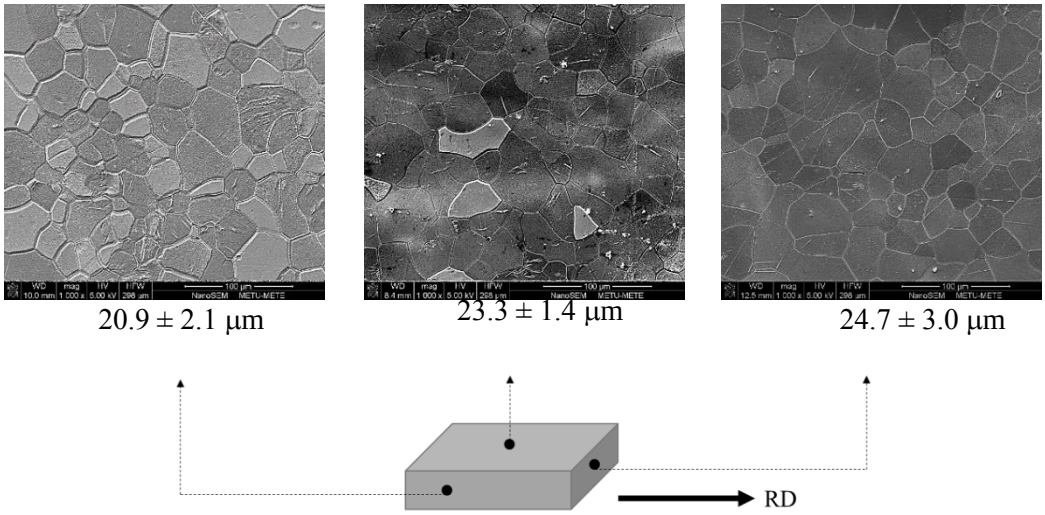


**Figure 4.1** Micrographs and grain sizes of three cross sections of AZ31 sheet.

### 4.1.3. Hardness

Hardness of the as received sample was measured from the rolled surface of the sheet. Pure Mg cast structure was also measured as a reference, in order to show the solute solution hardening effect of Al and Zn in Mg. Hardness of pure Mg casting was 33.2 ± 2.6 while hardness of as received AZ31 was 54.5 ± 0.4 HV0.3.

### 4.1.4. Texture

X-Ray Diffraction patterns of AZ31 from the rolled surface showed a dominant basal texture when compared to the powder magnesium diffraction data. X-Ray Diffraction pattern of as received sample can be seen in Figure 4.2.a and can be compared with the randomly textured powder data in Figure 4.2.b.

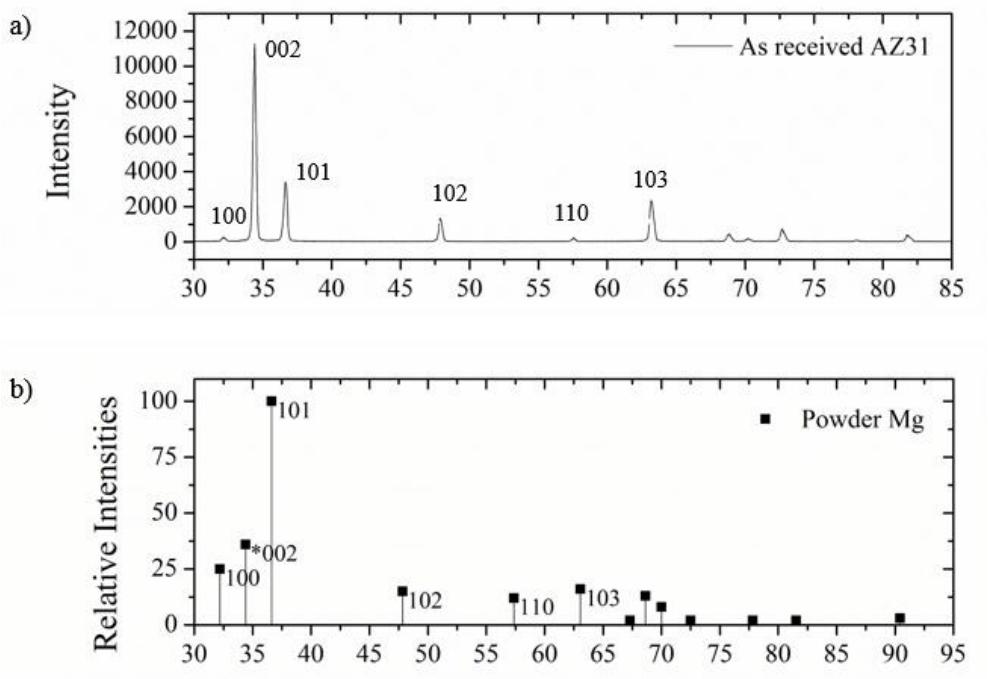


**Figure 4.2** a) X-ray diffraction patterns of a) as received AZ31 and b) powder magnesium with random orientation.

Diffraction patterns show that, in the as received sample, probably due to sheet forming procedures, there is a noticeable basal texture. It is expected and commonly observed in rolled magnesium.

### 4.1.5. Effects of annealing on as received samples

Prior to deformation and recrystallization studies, some of the samples were annealed at different temperatures to have a general understanding of possible effects of temperature on the as received microstructure and hardness. As it was expected samples annealed at high temperature like 400°C showed softening and grain growth as can be seen in Figure 4.3. Annealing at 100°C for 24 hours resulted in a hardening. That was taken as an indication of a possible $Mg_{12}Al_{17}$ (β) phase precipitation. Scanning electron microscopy examination conducted during the recrystallization studies revealed the precipitation like structures mainly at recrystallization sites.

a) b)

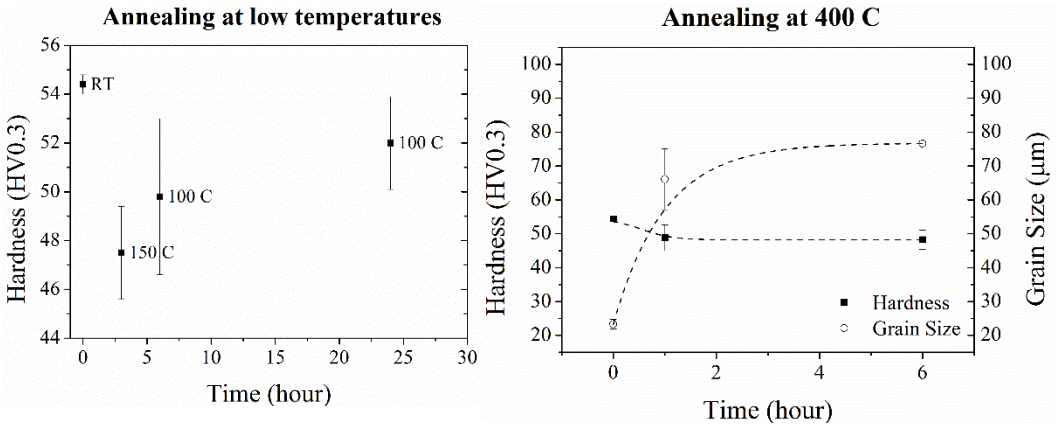


**Figure 4.3** a) Change in hardness in samples annealed at low temperatures like 100 and 150°C and b) hardness - grain size relation in samples annealed at 400°C.

Secondly when the ratio of integrated intensities, $I_{(002)}$ / $I_{(101)}$ were normalized according to that of powder magnesium and compared, it was seen that basal texture in the annealed sample was stronger than that of as received. Considering the fact that, grain size of annealed sample was almost 3 times larger than that of as received sample, one can assume that due to preferential growth, grains with their basal planes parallel to rolling plane were probably growing faster than others.

## 4.2. Examinations on Rolled Samples

### 4.2.1. Microstructure

After the rolling processes microstructure consisted of mainly twins with sharp and straight features as in Figure 4.4.b. Remaining of the matrix, namely un-twinned regions did not show much deformation indications observable with optical or scanning electron microscopy.

Samples rolled to 0.36 true strain contained micro cracks preventing further deformation, which resulted in complete fracture of the samples.

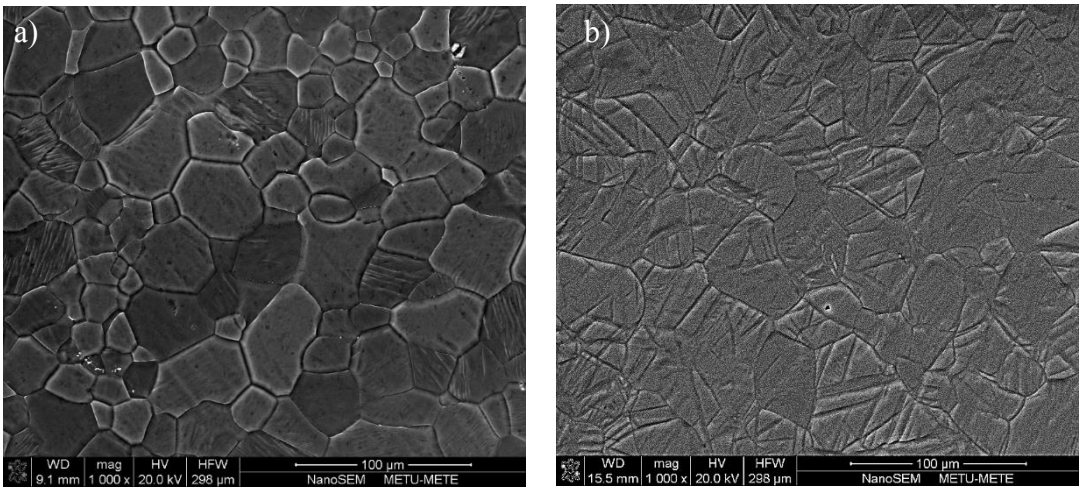


**Figure 4.4** a) As received AZ31 microstructure and b) same sample after 0.29 strain.

In the rolled samples most of the cracks were generated after 0.25 strain and they were observed to be 45° to the rolling surface. Highest strain attained upon rolling without fracture was 0.48; however this strain value was only possible with cyclic deformation and annealing treatments that will be covered later. At the strain value of 0.48, shear band structures became prominent as in Figure 4.5.

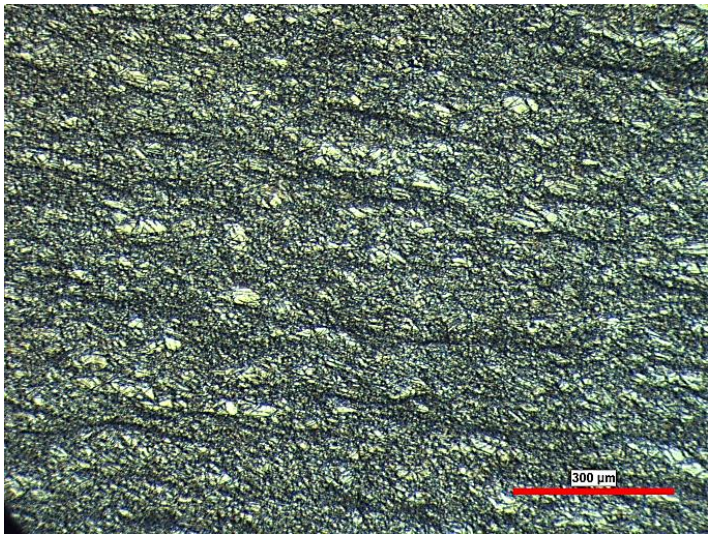


**Figure 4.5** Dark areas, shear bands in rolled samples after 0.48 true strain.

Even before the annealing processes, rolled samples were observed to have recrystallized nuclei, especially in twinned regions. As it can be seen in Figure 4.6 the sample rolled to 0.1 strain had already tiny nuclei inside some of the twins. These twins had a probably higher density of dislocation increasing the stored energy and creating sufficient driving force for nucleation of strain free grains. As the deformation levels increased more nuclei was observed again mostly inside twins and some at grain boundaries.

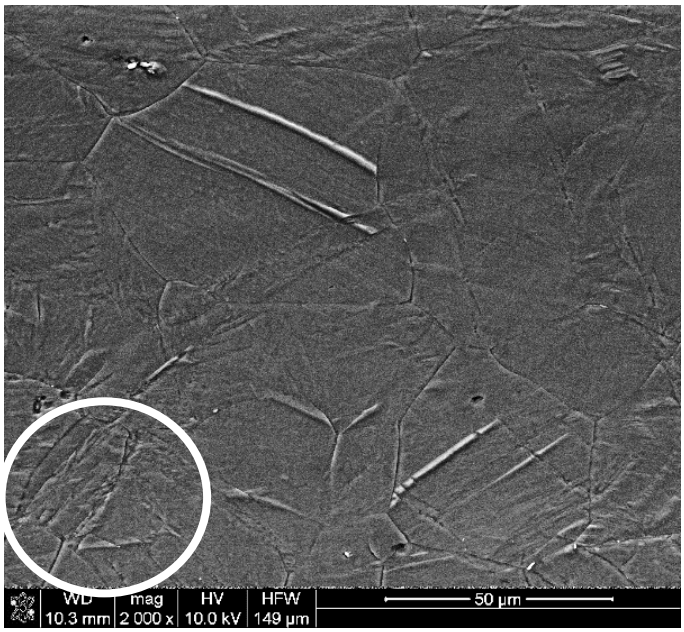


**Figure 4.6** Recrystallized nuclei in a 0.1 rolled sample are visible inside the white circle

### 4.2.2. Hardness

Hardness of the samples was increased as a result of rolling up to 0.36 strain, beyond which no strain hardening was observed, while micro cracks formed and further deformation resulted in complete fracture. After noticeable cracks formed rolling process was stopped. Thus hardness data of rolled samples was collected up to the initiation of fracture as can be seen in Figure 4.7. Around 0.60 strain complete fracture was observed in rolling.

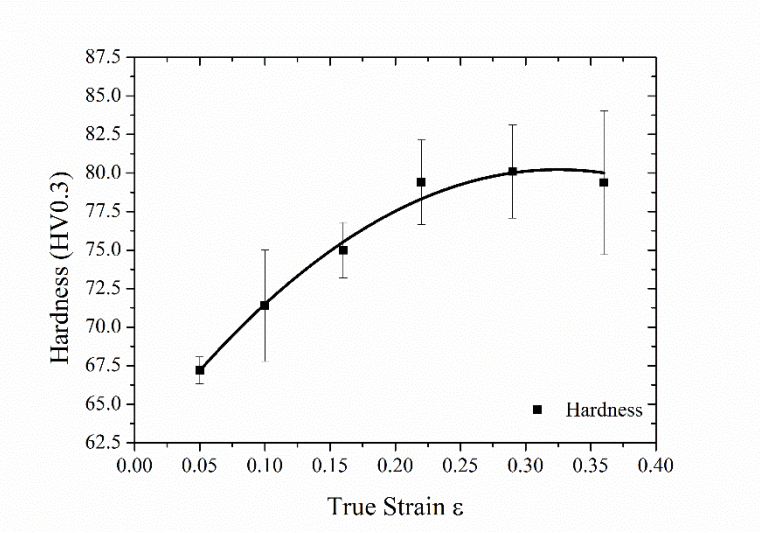


**Figure 4.7** Hardness versus strain levels in rolled samples. Hardness measurements were taken from the side section of the sheet, perpendicular to transverse direction.

When hardness distribution is considered, measured values were observed to be slightly higher at the rolled surface and also at the center of the sample's cross section. Average hardness of the 0.1 rolled sample was 75.5 ± 3.4 HV0.3.

### 4.2.3. Crack initiation and propagation in rolled samples

In rolled samples, cracks were oriented almost 45 degrees to the rolling direction as expected. Figure 4.8 and 4.9 below belong to a sample cracked after 0.22 strain by rolling. Samples rolled to 0.60 without intermediate anneals were fractured and broke apart.

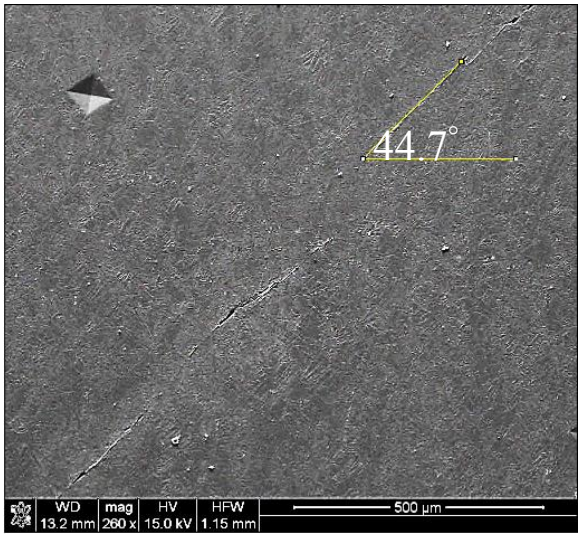


**Figure 4.8** Micrograph of 0.22 rolled sample, showing 45° oriented crack. Rolling direction is horizontal. Crack was initiated and propagated inside the sample.

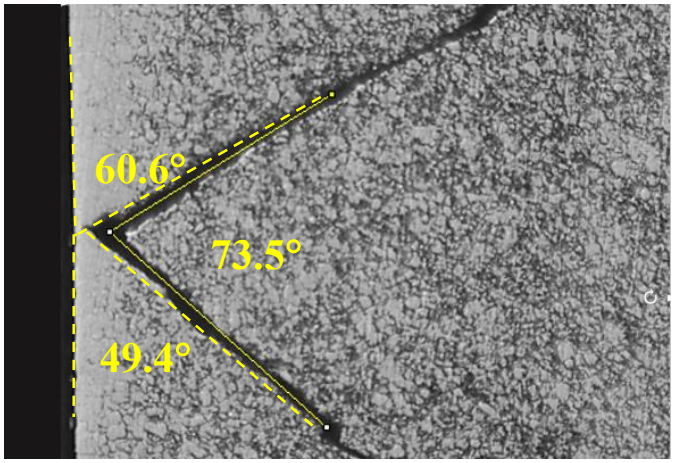


**Figure 4.9** Micrograph showing the side cracks of the sample in Figure 4.8.

### 4.2.4. Texture

X-ray diffraction pattern of 0.29 rolled sample and as received sample is compared in Figure 4.10. When the relative intensities of diffractions from (002) planes and (101) planes of as received and 0.29 rolled sample were compared, it was seen that rolled sample had a stronger basal texture than the former.

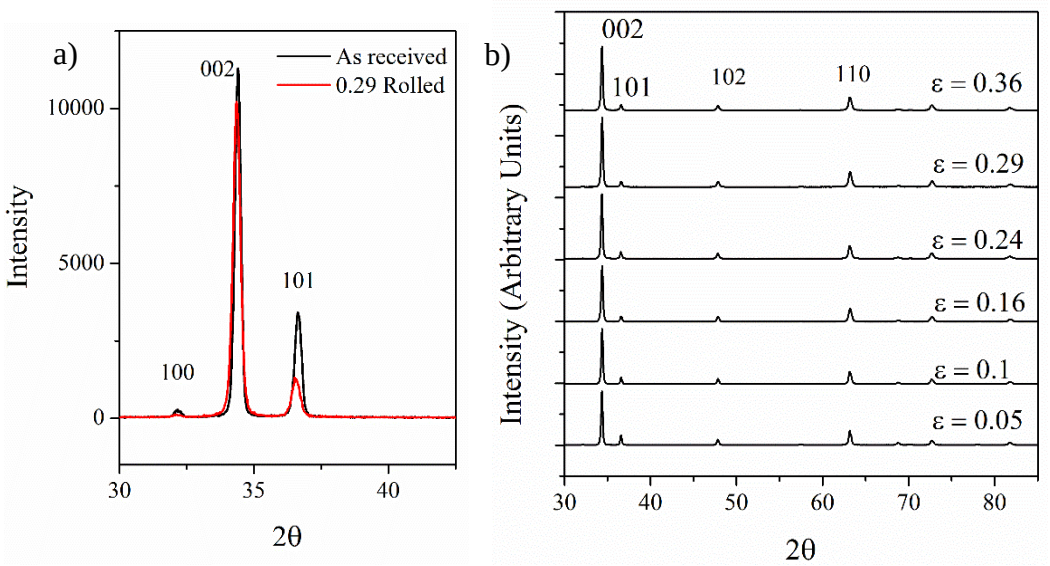


c)

| | Powder | As Received (ND) | ε=0.05 (ND) | ε=0.1 (ND) | ε=0.16 (ND) | ε=0.24 (ND) | **ε=0.24 (TD)** | ε=0.29 (ND) | ε=0.36 (ND) |
|---|---|---|---|---|---|---|---|---|---|
| Integrated Intensity Ratio $I_{(002)}/I_{(101)}$ | 0.36 | 2.81 | 4.74746 | 6.88734 | 7.59306 | 7.34985 | **0.09859** | 8.62669 | 7.225 |
| Normalized $\frac{Sample\ \frac{I(002)}{I(101)}}{Powder\ \frac{I(002)}{I(101)}}$ | 1 | 7.805556 | 13.18739 | 19.1315 | 21.09183 | 20.41625 | **0.27386** | 23.96303 | 20.06944 |

**Figure 4.10** a) XRD data of as received and 0.29 rolled sample and b) XRD patterns after rolling to different strain values, c) Normalized integrated intensity comparisons of samples with different strains. Bold values represent data from plane perpendicular to transverse direction (TD), whereas others are from plane perpendicular to normal direction (ND).

Since even in as received samples as given in Figure 4.10.c, there was basal texture when compared to powder. Further rolling enhanced the relative intensity of basal diffractions compared to diffractions from (101) planes. In Figure 4.10.b, diffraction patterns of rolled samples rolled to different strains are given and the variation of ratio of their (002) to (101) plane diffraction intensities can be seen in Figure 4.11.

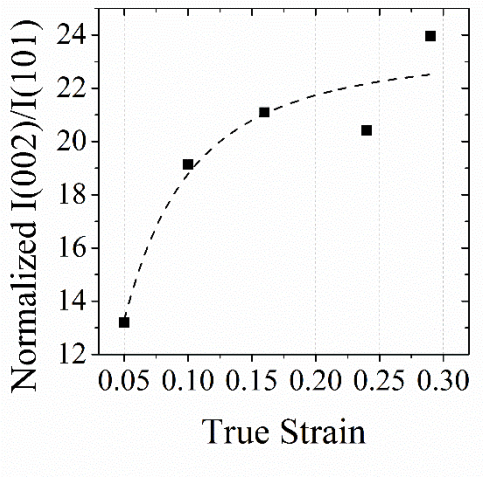


**Figure 4.11** Normalized intensity ratios of (002) and (101) diffractions showing the increase in the basal texture with strain.

When different cross-sections of a 0.24 rolled sample was investigated using X-Ray diffraction patterns, dominant basal texture was observed at the rolled surface while almost no basal diffraction was recorded from the longitudinal section (Figure 4.12).

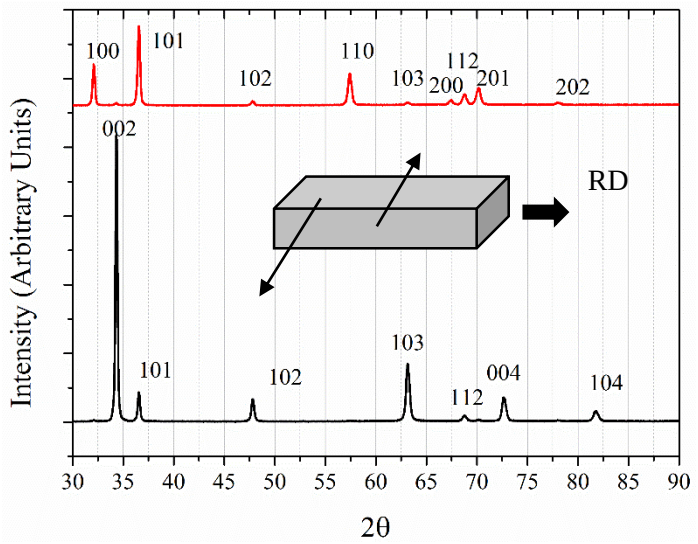


**Figure 4.12** X-Ray diffraction patterns of different cross-sections of a 0.24 rolled sample.

### 4.3. Examinations on Rolled and Annealed Samples

#### 4.3.1. Microstructure

Rolled samples were annealed at different temperatures for different durations. As mentioned before during the microstructure examinations of as deformed sample, some recrystallized nuclei were observed. Observations on optical and scanning electron microscopy implied that the nucleation process was in progress during the deformation step, probably due to exceeding a critical strain. Further annealing was mainly a growth phenomenon.

Most commonly observed microstructural feature was the partially recrystallized structure. Samples with relatively homogeneous grain size distribution was assumed to be completely recrystallized, however those cases may also be a result of the balance between recrystallized, new grown grains and un-recrystallized shrinking old grains. More detailed study focusing on the grain boundary curvature could be used to enlighten this fact, but it was not included in this thesis study.

Most of the recrystallization nuclei were observed inside twinned regions. As a result of the nucleation prior to annealing no incubation period was detected during the recrystallization studies. Examinations done with optical and scanning electron microscopy revealed that initial recrystallization fractions of 0.1 rolled and swaged samples were about approximately 9% and 13% respectively.

As stated in literature and also seen in this study most of the nuclei were located in the twinned regions, yet during the microstructural examinations, there were also cases in which in the same micrograph, nucleation was seen inside some twins while not inside the others as shown in Figure 4.13. Even though detecting twin types was beyond the scope of this study, it is possible to simply relate the different behavior of a twin to its specific type and orientation.

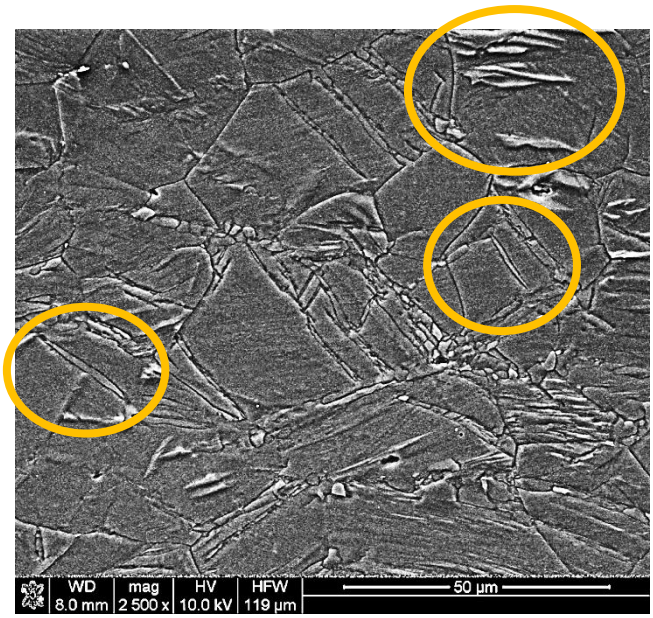


**Figure 4.13** Samples rolled to 0.1 and annealed at 185°C for 700 seconds (~12 min) selected areas indicates the twins with no nuclei.

Orientation of one type of twin might have created favorable conditions (higher Schmid factor) for slip, while the other twin type was not favorable for further slip inside it, thus no nucleation occurred due to the lack of stored energy. This may be true even for the same type of twin but with different initial orientation. One another reason of this fact could be that the twins that show no recrystallization might have been created mechanically during the specimen preparation step.

### 4.3.2. Hardness

When the softening of the annealed samples are calculated according to Equation 3.2 and plotted against time, two different patterns were observed. Samples annealed at temperatures higher than 185°C had higher slopes when compared to samples that were hold at low temperatures like 100 and 150°C for even days (Figure 4.14). Microstructure of the sample hold at 100°C for one day given in Figure 4.15.b and 4.15.c also support this behavior by showing not much sign of recrystallization. Microstructure showed tiny precipitates and nuclei of deformation origin but further annealing did not create much change in the microstructure. Softening was very

limited due to lack of recrystallization during annealing and due to formation of precipitates.

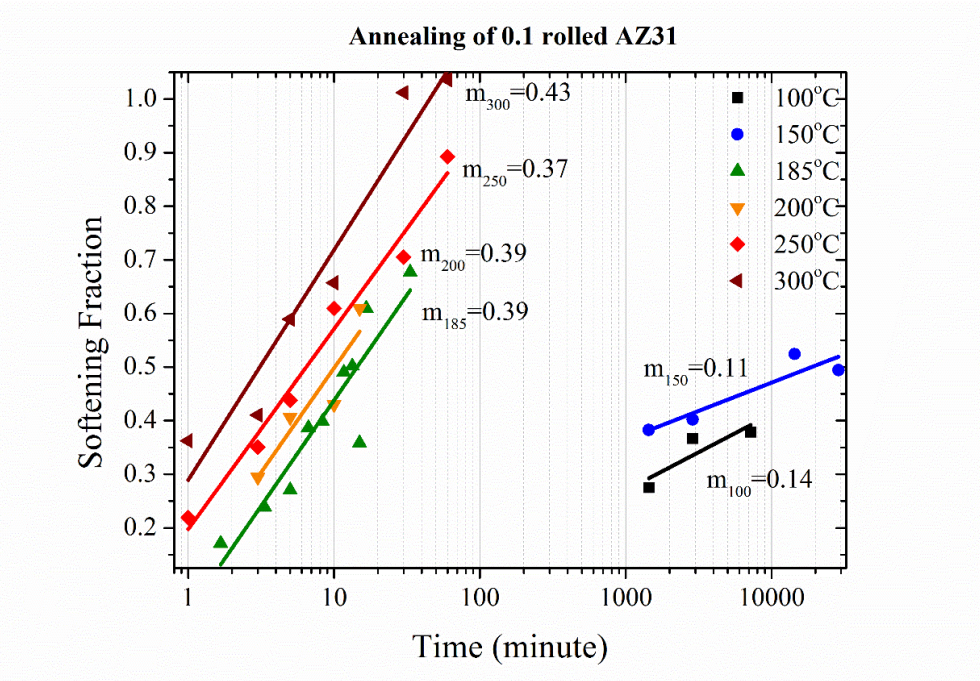


**Figure 4.14** Softening fraction of 0.1 rolled AZ31 calculated according to Equation 3.2.

Since complete recrystallization was not attained at low temperatures like 100°C and 150°C, hardness values of rolled samples did not decrease down to values of fully annealed sample. When samples 0.1 rolled and annealed at 300°C are considered, after 60 minutes sample reaches the hardness values of a sample held at 400°C for 6 hours.

a)

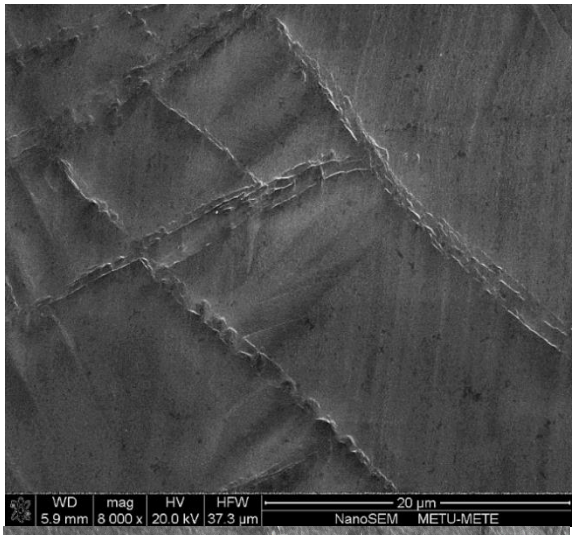


b)

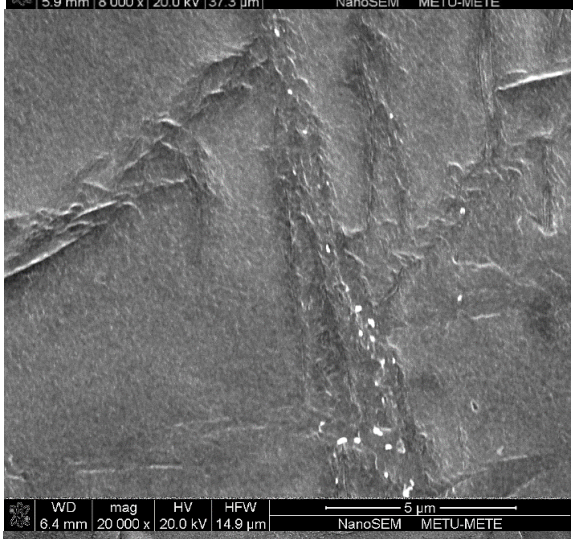


c)


**Figure 4.15** 0.16 rolled samples after a) 1 hour at 100°C, b) and c) 24 hours at 100°C.

### 4.3.3. Texture

When the texture of samples rolled ( to 0.22 and 0.36 strain ) and annealed at different temperatures for 1 hour were examined (Figure4.16.a and b), it was observed that as the annealing temperature increases the relative intensity of (002) plane to (101) plane decreases (Figure 4.16.c). Which implies that annealing also produces basal textured grains but the texture generated was not as strong as that of rolling.

a)

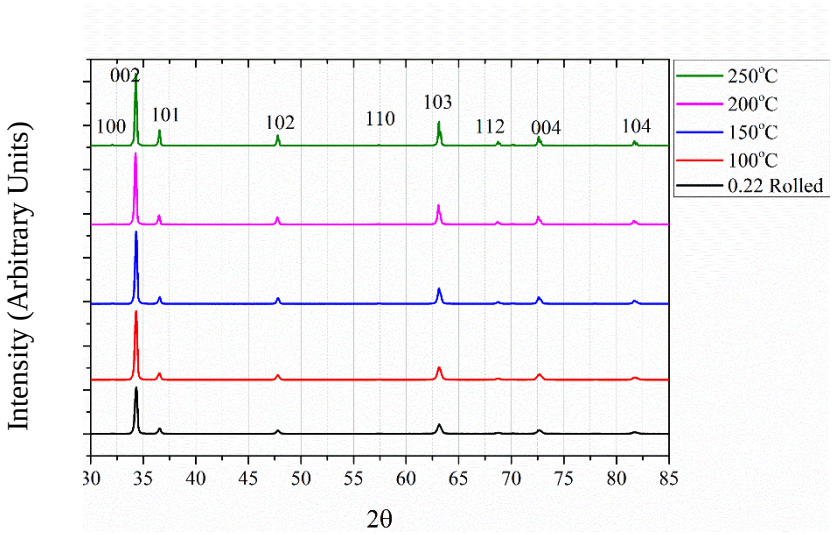


b)

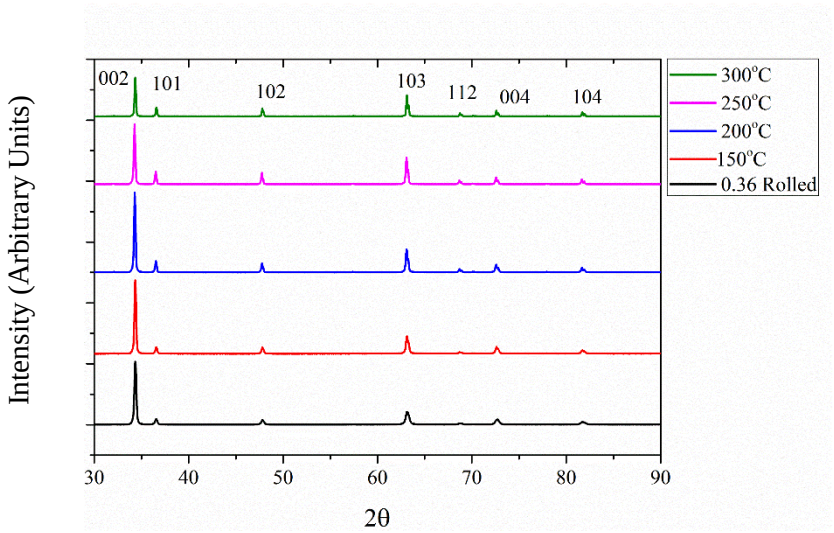


**Figure 4.16** (Continued)

c)

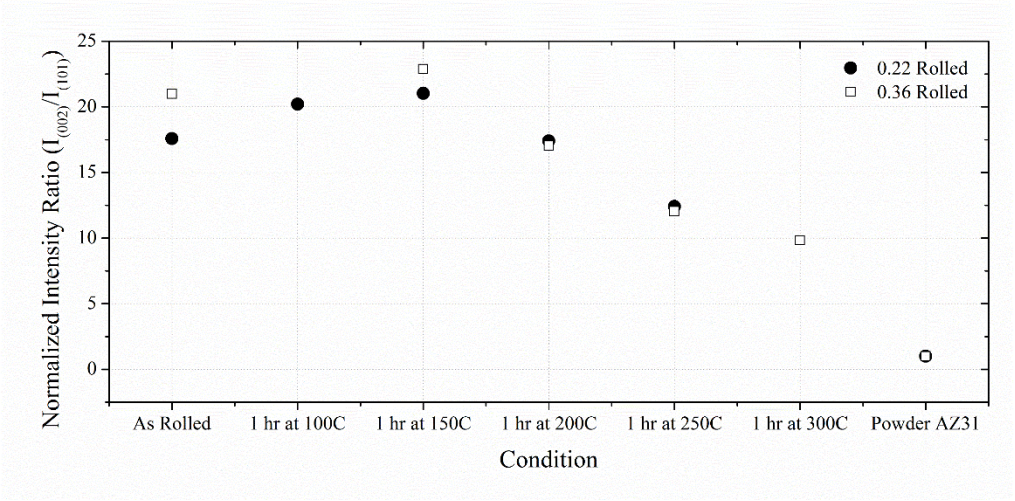


**Figure 4.16** XRD patterns of a) 0.22 and b) 0.36 rolled samples after annealing at different temperatures for 1 hr. c) Their $I_{(002)}/I_{(101)}$ ratios at different states.

### 4.3.4. Recrystallization

In general during almost all recrystallization experiments, most common route observed was as follows; nucleation at favorable sites, twins and grain boundaries, starts, then saturation of these sites occurs, no new nuclei appears from then on. It was thought that changes up to that point occur during deformation, before annealing. During annealing, rather than more nucleation, existing nuclei grow while consuming the remaining areas that did not get deformed to have enough stored energy for nucleation to start. Growth of new nuclei continues as those un-deformed areas shrink.

Samples even with the longest annealing time do not always get recrystallized completely. Growth of the existing nuclei continued but after the point where their size reached the size of the un-deformed remnant grains, it was not possible to differentiate either type. Actually, whether this should be considered as recrystallization or grain growth is questionable and could only be resolved from the direction of boundary motion, i.e., towards the concave or convex side of the boundary. Figure 4.17 summarizes the general course of recrystallization in AZ31, first sketch represents the twin formation state, second one shows the point at which

nucleation site saturation occurs mainly inside twins and the last sketch indicates the growth of existing nuclei. Completion of the recrystallization occurs when the blue areas are completely consumed however in this study it was found difficult to calculate the recrystallization fraction when the size of the growing nuclei and the shrinking old grains (blue areas) become similar in size and thus hard to differentiate. At this particular point the recrystallization fraction measurements were stopped in this study.

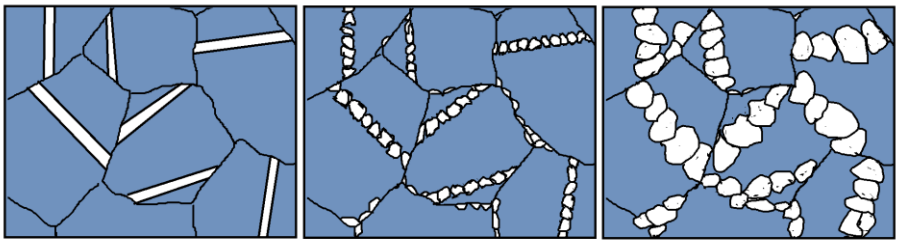

**Figure 4.17** General course of recrystallization in AZ31 alloy, transformation to strain free grains occurs by the consumption of blue areas.

Recrystallization fraction calculations were done by point counting method as explained in the previous chapter. For the determination of the kinetics of recrystallization ln(ln(1/(1-$X_{rec}$) versus ln(t) graphs plotted according to Avrami equation, Equations 4.1 and 4.2, where $X_{rec}$ was recrystallization fraction, k and n were Avrami constants. Determination of the activation energy for recrystallization was possible by plotting the lnk versus 1/T (°K) graph according to Equation 4.3 and 4.4 where slope gives the –Q/R value.

$X = 1 - \exp(-kt^n)$.....(JMAK) (4.1)

$\ln(\ln(1/(1-X))) = lnk + nlnt$..... (4.2)

$k = k_0 . \exp(-\frac{Q}{RT})$..... (4.3)

$$lnk = lnk_0\ (-\frac{Q}{RT})$$……..……..……..…..... (4.4)

Intercept value of JMAK (Johnson-Mehl-Avrami-Kolmogorov) plots, 'lnk' was used to draw 'ln k' versus 1/T (°K) graphs, slope of which gives the activation energy for recrystallization of AZ31; however activation energy calculations were intended to be covered in a future work. Observations showed that due to non-uniform deformation of AZ31, combination of many processes occur simultaneously during annealing and general behavior was rather complex to be represented with Avrami Equation only. Assumptions of Avrami Equation such as random nucleation and constant rate of nucleation and growth may not be true for AZ31.

Even at the as deformed state almost all samples had a small percentage of recrystallized nuclei inside them, as a result sigmoidal curves in the recrystallization fraction versus annealing time graphs did not start from zero and thus they might actually be corresponding to the growth of the already existing nuclei.

In the recrystallization studies conducted at very low temperatures like 100°C, complete recrystallization was never attained in the investigated time interval (1-5 days). Figure 4.18 shows the results of low temperature trials in samples rolled to different deformation levels. Even though increase in the deformation also increases the recrystallization amount, 5 days of annealing was not enough to completely recrystallize the structure. In Figure 4.19 and Figure 4.20 polarized light images of 0.36 rolled samples annealed at 100°C and 250°C can be compared to see the effect of annealing temperature. While the sample annealed at 100°C for 5 days did not reach complete recrystallization, the one annealed at 250°C for 2 hours shows fully recrystallized equiaxed microstructure.

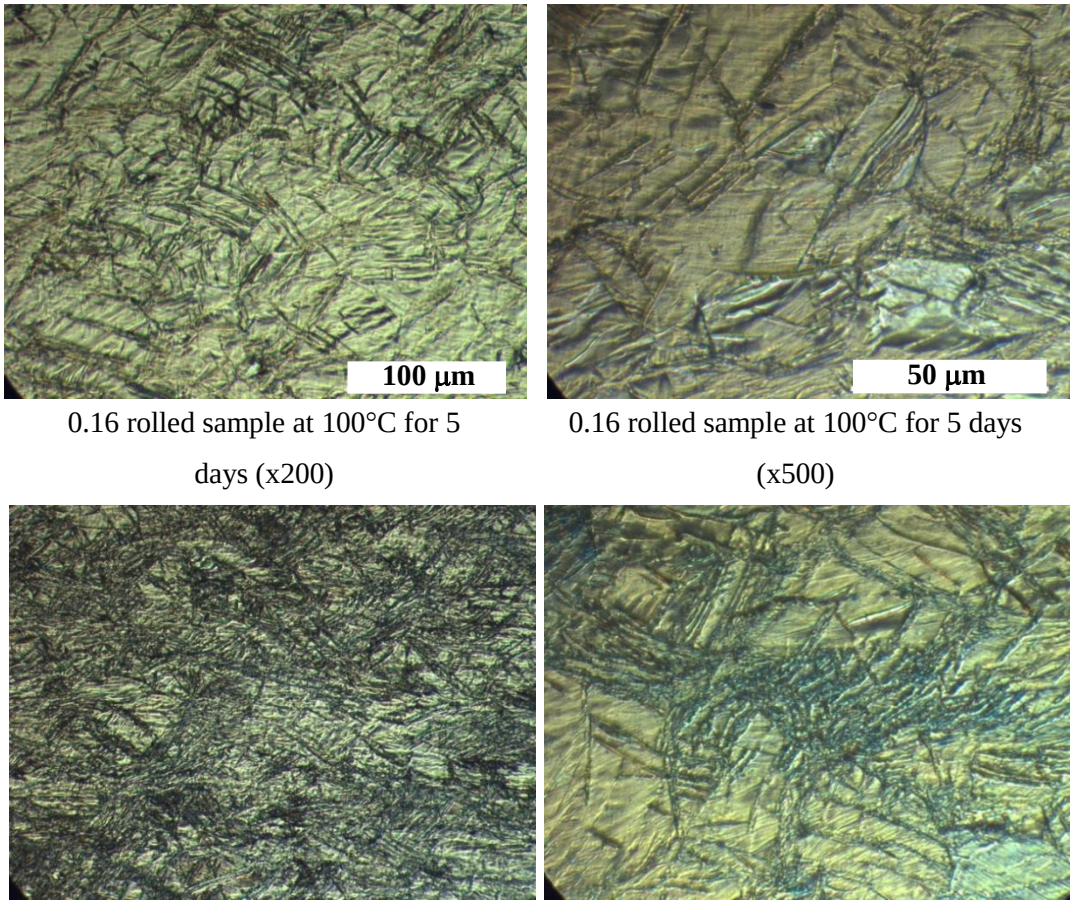


0.16 rolled sample at 100°C for 5 days (x200)

0.16 rolled sample at 100°C for 5 days (x500)

0.22 rolled sample at 100°C for 5 days (x200)

0.22 rolled sample at 100°C for 5 days (x500)

**Figure 4.18** Effect of increased deformation at low temperature recrystallization. Micrographs taken at x200 and x500 magnification.

One another effect of low temperature annealing was the potential of creating precipitation in the structure. SEM micrographs in Figure 4.15 show white precipitates, possibly the $Mg_{17}Al_{12}$ (β) phase as it was expected from the Mg-Al-1wt% Zn phase diagram.

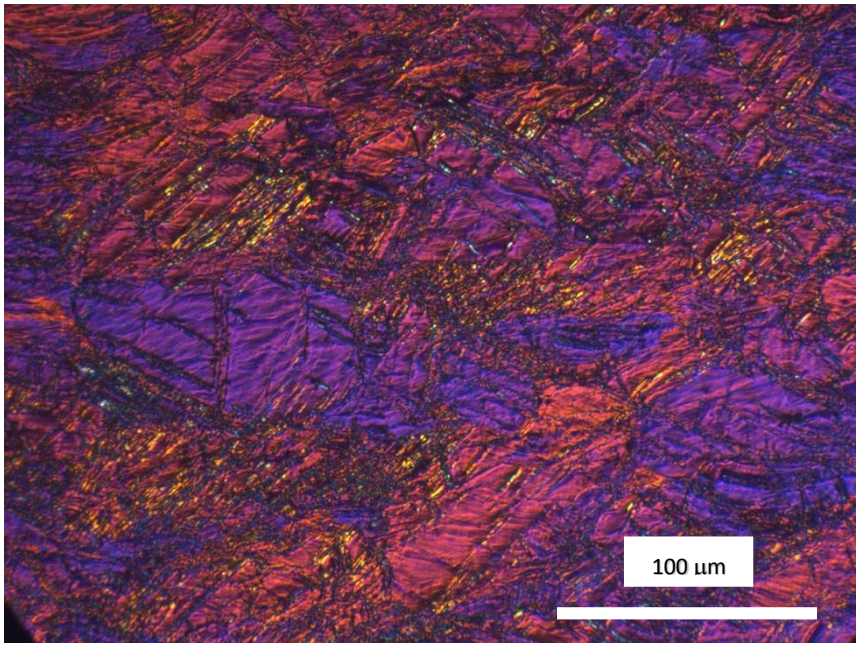


**Figure 4.19** 0.36 rolled and annealed at 100°C for 5 days.

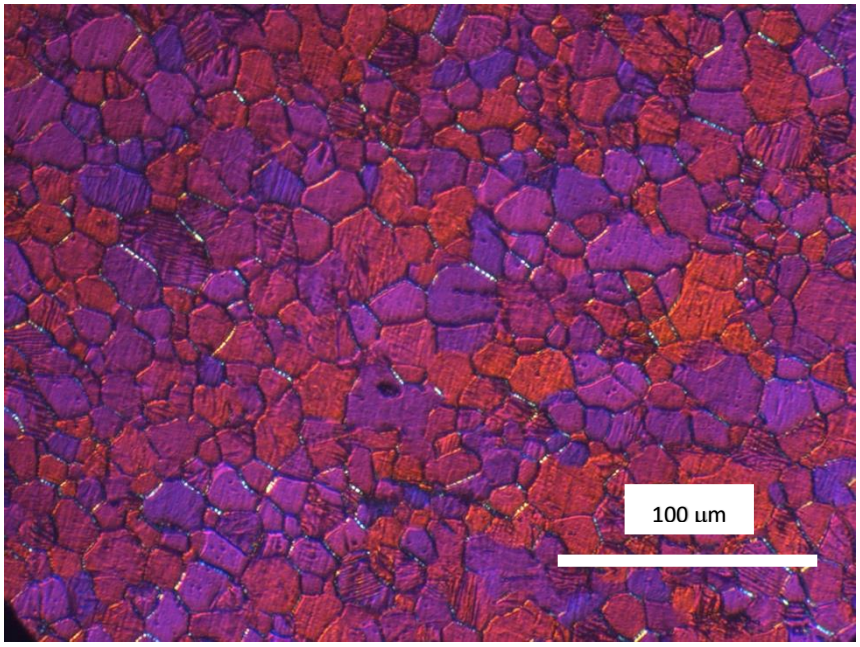


**Figure 4.20** 0.36 rolled and annealed at 250°C for 2 hrs.

Avrami plots in Figure 4.21, clearly show that as expected, recrystallization rate increased as the temperature increased from 185°C to 300°C. At temperatures

220°C and below, for samples rolled to 0.1 strain recrystallization was not completed at the investigated time interval and does not have a tendency to be completed even at much longer times. Not reaching complete recrystallization at low temperatures was explained by Figure 4.22, in which low deformation levels such as 0.1, requires high temperatures for complete recrystallization [82].

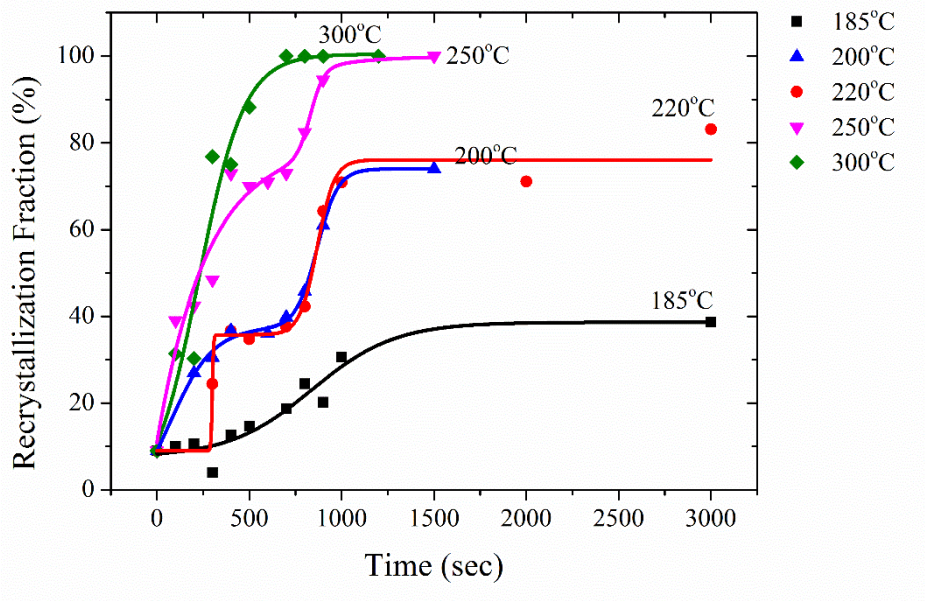


**Figure 4.21** Isothermal transformation graph for the recrystallization of 0.1 rolled samples.

In the Avrami plot (Figure 4.21) some of the recrystallization curves are not sufficiently extended because either it was not possible to differentiate recrystallized grains under the optical or scanning electron microscope, from the ones that did not or due to reaching steady almost horizontal plateau. At 185°C, even after 50 minutes recrystallization fraction does not exceed 39%. At 200, 220 and 250°C the data collected were best fitted with Biphasic Dose Response Function, which shows a two-step behavior for an unknown reason beyond experimental error.

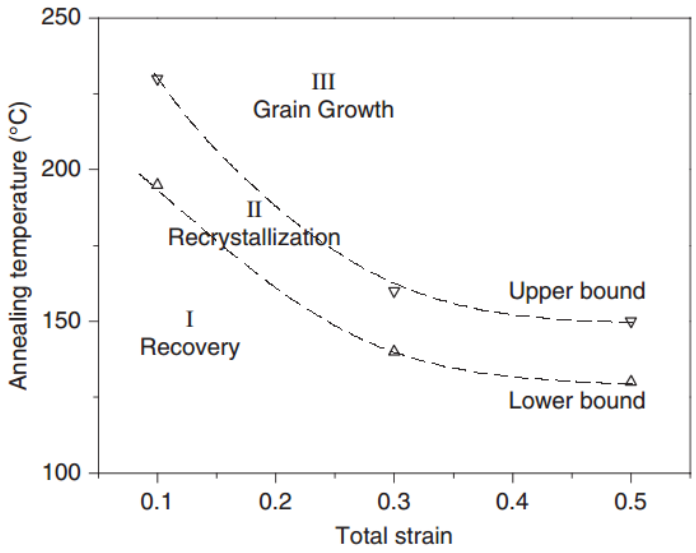


**Figure 4.22** Temperature and strain relation of isochronally annealed AZ31 [82].

Figure 4.23 shows the effect of temperature in general, each sample with a same initial deformation background, was annealed at a different temperature for comparison. Effect of higher temperature such as 200, 250 and 300°C is seen.

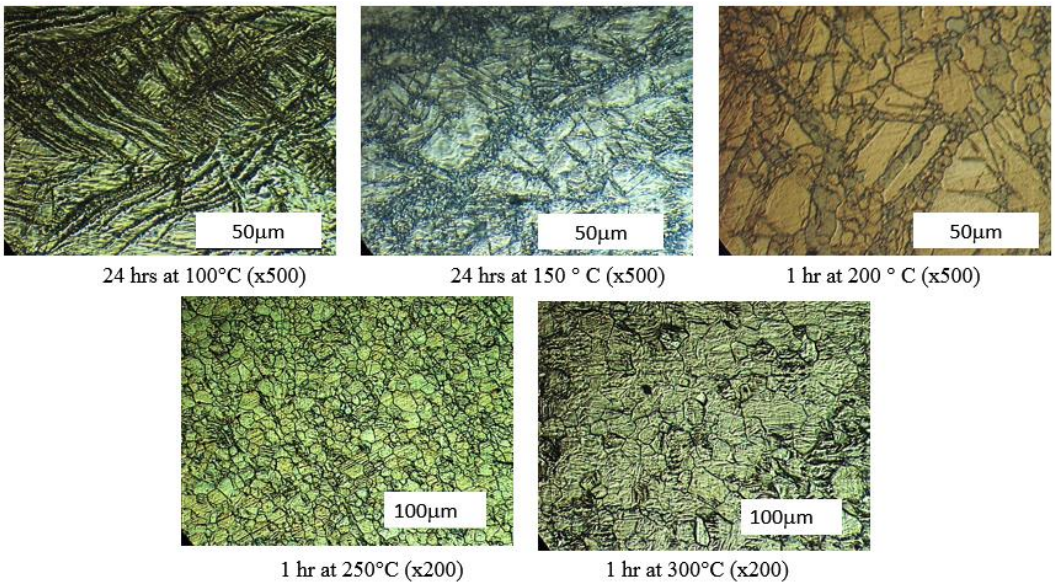


**Figure 4.23** A figure summarizing the effect of temperature on 0.22 rolled samples annealed at 100°C, 150°C, 200°C, 250°C and 300°C.

At higher temperatures like 300°C, for a 0.16 rolled sample recrystallization seems to be completed in 10 minutes. Micrographs in Figure 4.24 show the gradual progress of recrystallization, beginning with the nucleation stage and the subsequent growth.

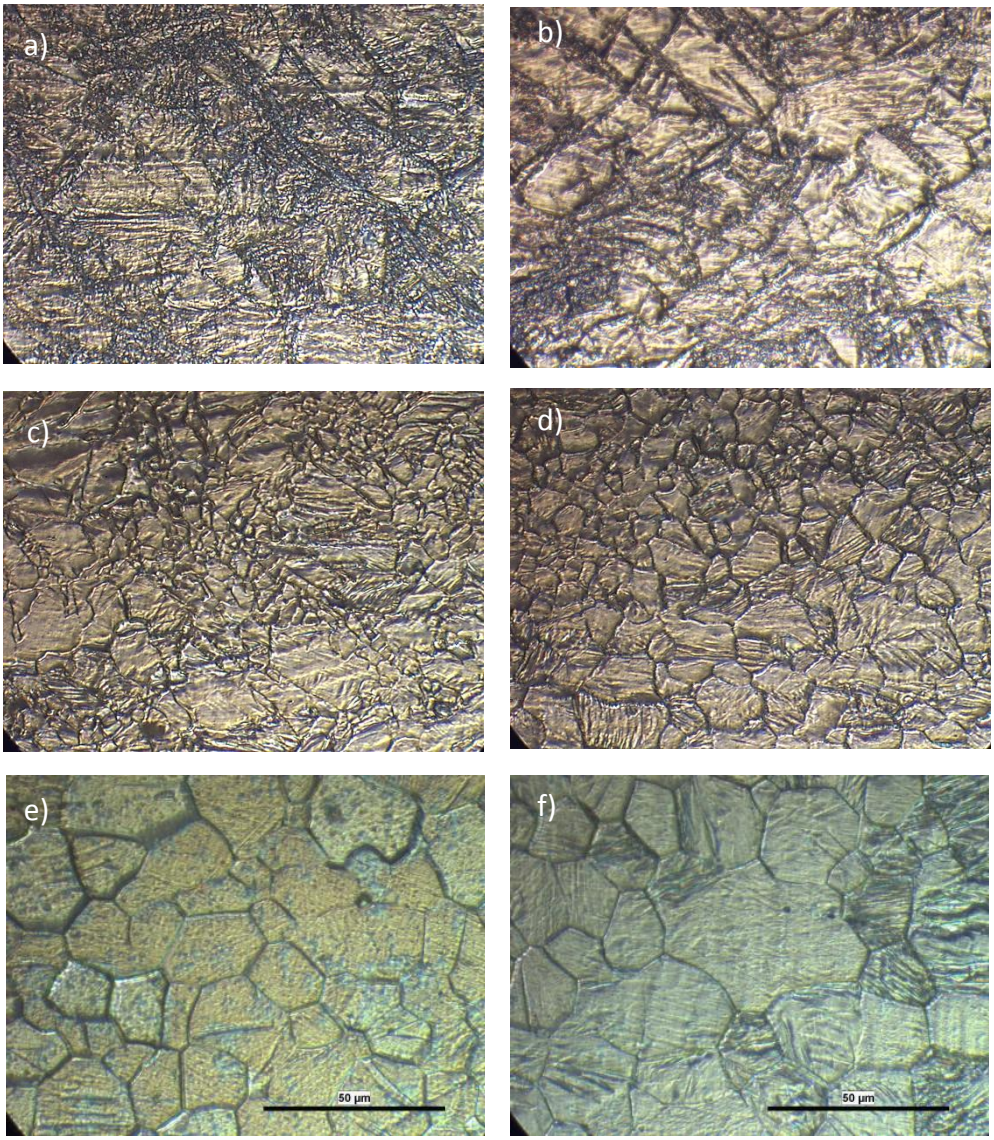


**Figure 4.24** Samples rolled to 0.16 strain and annealed at 300°C for a) 1min, b) 3 min, c) 5 min, d) 10 min, e) 30 min, f) 1 hr. All of the micrographs were taken at x500 magnification.

Linear JMAK graphs plotted according to Equation 4.2 are given in Figure 4.25. Low n values calculated will be discussed later in this chapter.

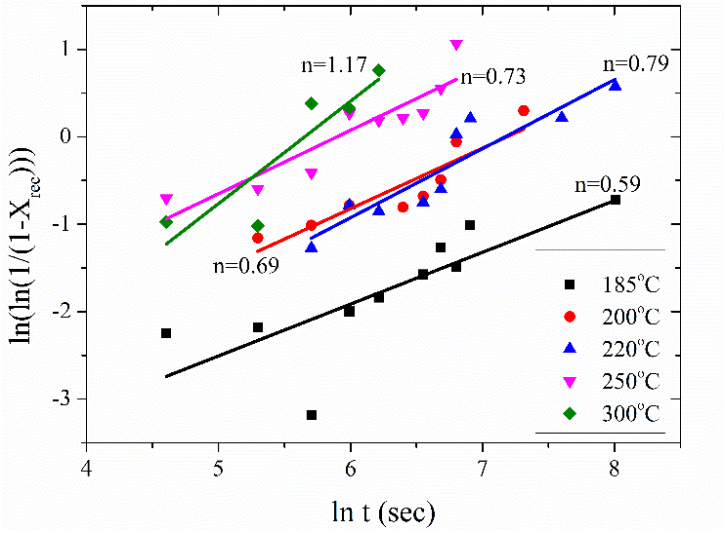


**Figure 4.25** JMAK plot of 0.1 rolled samples after recrystallization processes at different temperatures.

Deformation amount was found to be very effective in the determination of the final microstructure. Figure 4.26 shows two samples, one rolled to 0.16 true strain, and the other one to 0.22, both were annealed for 1 hour at 200°C.

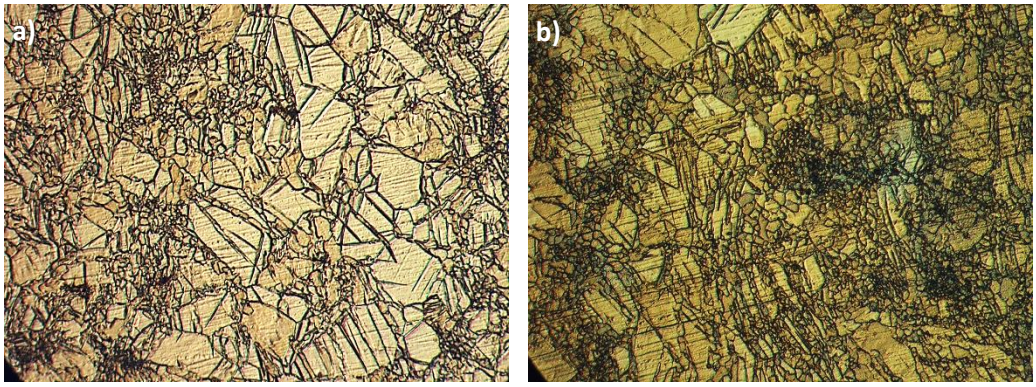


**Figure 4.26** Recrystallization after 1 hr at 200°C of 0.16 and 0.22 rolled samples (200x).

As can be seen, 0.22 rolled sample had more nuclei compared to the less deformed sample. Effect of a multidirectional deformation was expected to be even more pronounced than unidirectional deformation.

### 4.4 Cyclic Deformation and Annealing

During the static recrystallization studies it was observed that the nucleation almost always begins at twinned areas due to their high density of dislocations and then continues by consuming the relatively un-deformed/recrystallized matrix. Complete recrystallization was sometimes not possible and it was difficult to be sure, whether the recrystallized nuclei completely governed the structure or initial grains still remain. Microstructural examinations also revealed that, at the points close to complete recrystallization lack of uniformity in the grain size was also an issue. Uniformity in grain size distribution was only attained after a while of annealing with the expense of losing most of the fine sized grains in the process of grain growth.

As a method to reach completely recrystallized structure, without losing the small sized nuclei in the process of grain growth, interrupted deformation and annealing were applied. Grain growth was prevented by interrupting the annealing step and the un-deformed matrix was re-deformed, new twins were created and upon annealing, nucleation again started inside these newly formed twinned regions. A simple sketch in Figure 4.27 summarizes this behavior. With the use of this fact, cyclic deformation and annealing was done in order to continuously create twinning and thus successive nucleation.

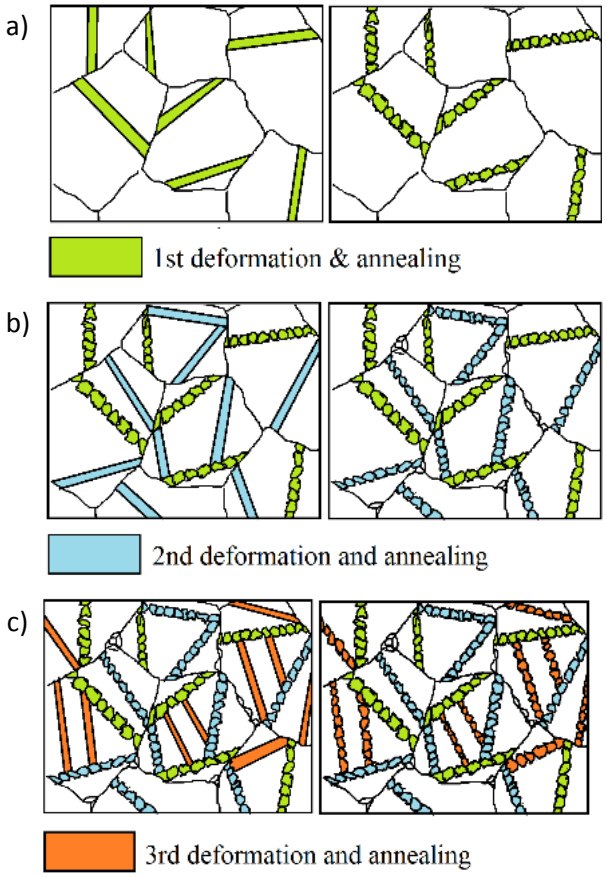


**Figure 4.27** Sketch showing three successive cycles (a,b,c) of deformation and annealing. Growth of nuclei was not shown in sketch but exists in reality.

All of the cyclic recrystallization studies were done by rolling and strain was again calculated according to the true strain equation in Equation 3.1. In the first cyclic recrystallization trials two cycles were applied; first one was with a deformation of 0.26 and a 30 minutes of annealing at 200°C, second cycle with 0.18 deformation and then a following 30 minutes of annealing at 200°C. Resultant microstructures are given in Figure 4.28. In Figure 4.28.a one can see the nuclei inside the first appearing twins and the secondary twinning that has just occurred in the second deformation step, difference of the Figure 4.28.b is just an additional annealing step, during which the sample partially recrystallizes for the second time. In Figure 4.28.b, nucleation of this new recrystallization cycle could be seen. New twins were replaced with the recrystallized nuclei while no excessive grain growth was detected

for the previously formed nuclei. In figure 4.28.b one can see the non-recrystallized areas as well, since the process was not completed.

a)

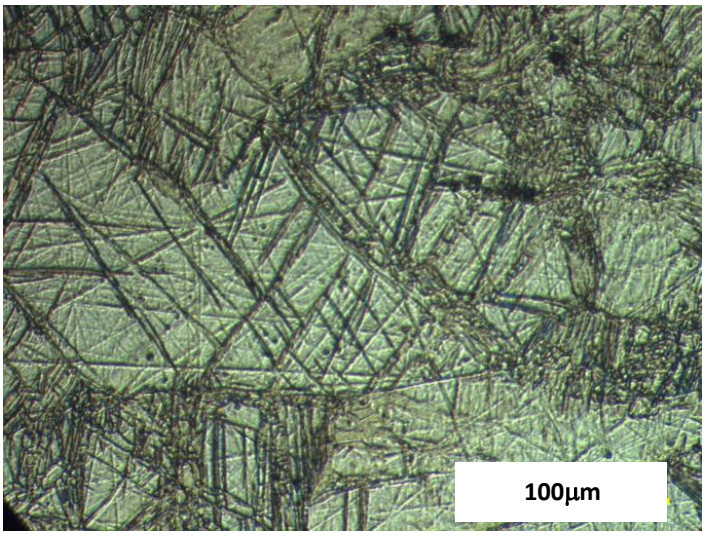


b)

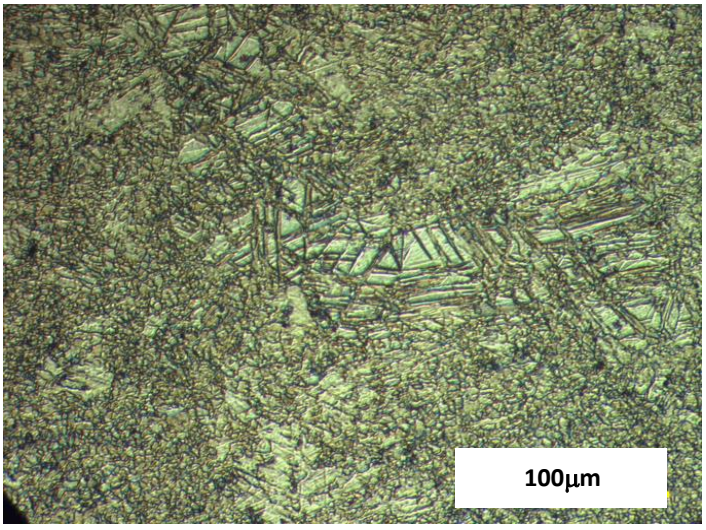


**Figure 4.28** Microstructures after a) 0.26 strain + 30 min at 200°C + 0.18 strain, b) 0.26 strain+ 30 min at 200°C + 0.18 strain + 30 min at 200°C. Recrystallizaiton not complete.

With reference to this first cyclic recrystallization study, a new cyclic recrystallization route was planned. In order to be able to reach higher deformation levels without cracking, deformation amounts in each cycle was reduced. Annealing periods were reduced as well to prevent grain growth. Cycle parameters are given in Figure 4.29.

Grain refinement was successfully achieved with low deformation and short annealing procedures. After each deformation and annealing step, optical micrographs and micro-hardness measurements were taken in order to follow the progress of recrystallization and the change in mechanical properties. As given in Figure 4.30, as the recrystallization approach completion, recrystallized grain size remained around 3 μm. In contrast to these samples, samples that had only one cycle of recrystallization with a comparable annealing treatment, did not reach 100% recrystallization level at the same time intervals and also could not retain their fine grain size.

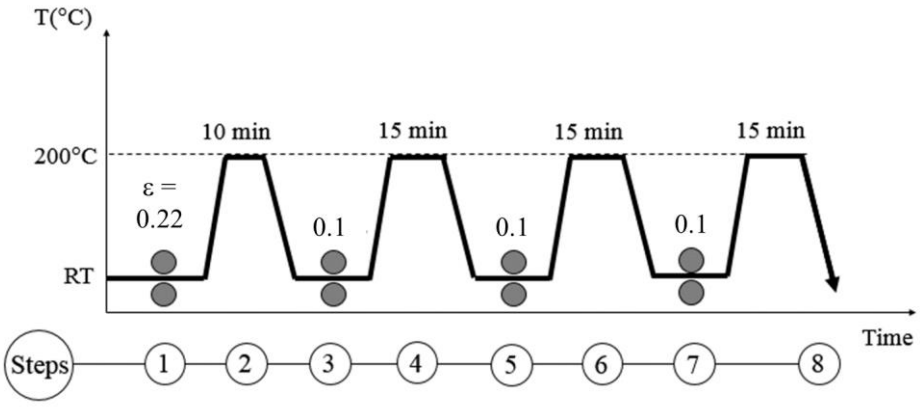


**Figure 4.29** Steps and parameters of cyclic recrystallization.

In Fıgure 4.31, resultant average hardness values can be seen after each step, namely deformation and annealing. The decrease in hardness of rolled worked structure upon each annealing process can be seen however as the number of cycles increase, cumulative hardness of the annealed structure seem to increase probably due to grain refinement.

Microstructural changes can be seen in Figure 4.32, as it is explained in Figure 4.27. As the grains got finer, twin formation was not observed instead structures like shear bands became visible as can be seen in the 5$^{th}$ and 7$^{th}$ steps in Figure 4.32.

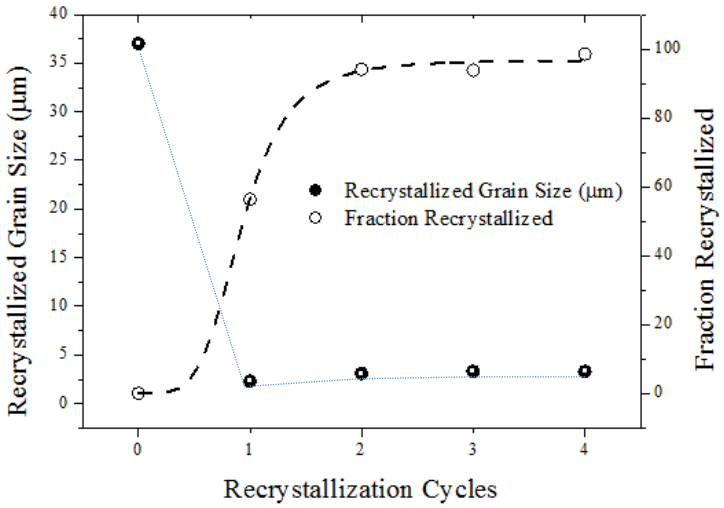


**Figure 4.30** Changed grain size and recrystallization fraction with the cycles. Each cycle consisted of deformation and a successive short annealing process.

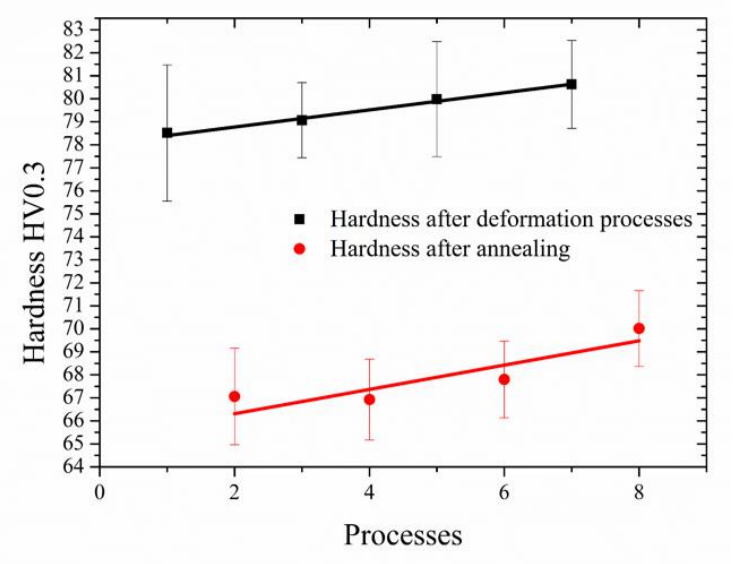


**Figure 4.31** Hardness after annealing and deformation cycles. Pattern of increasing hardness can be seen.

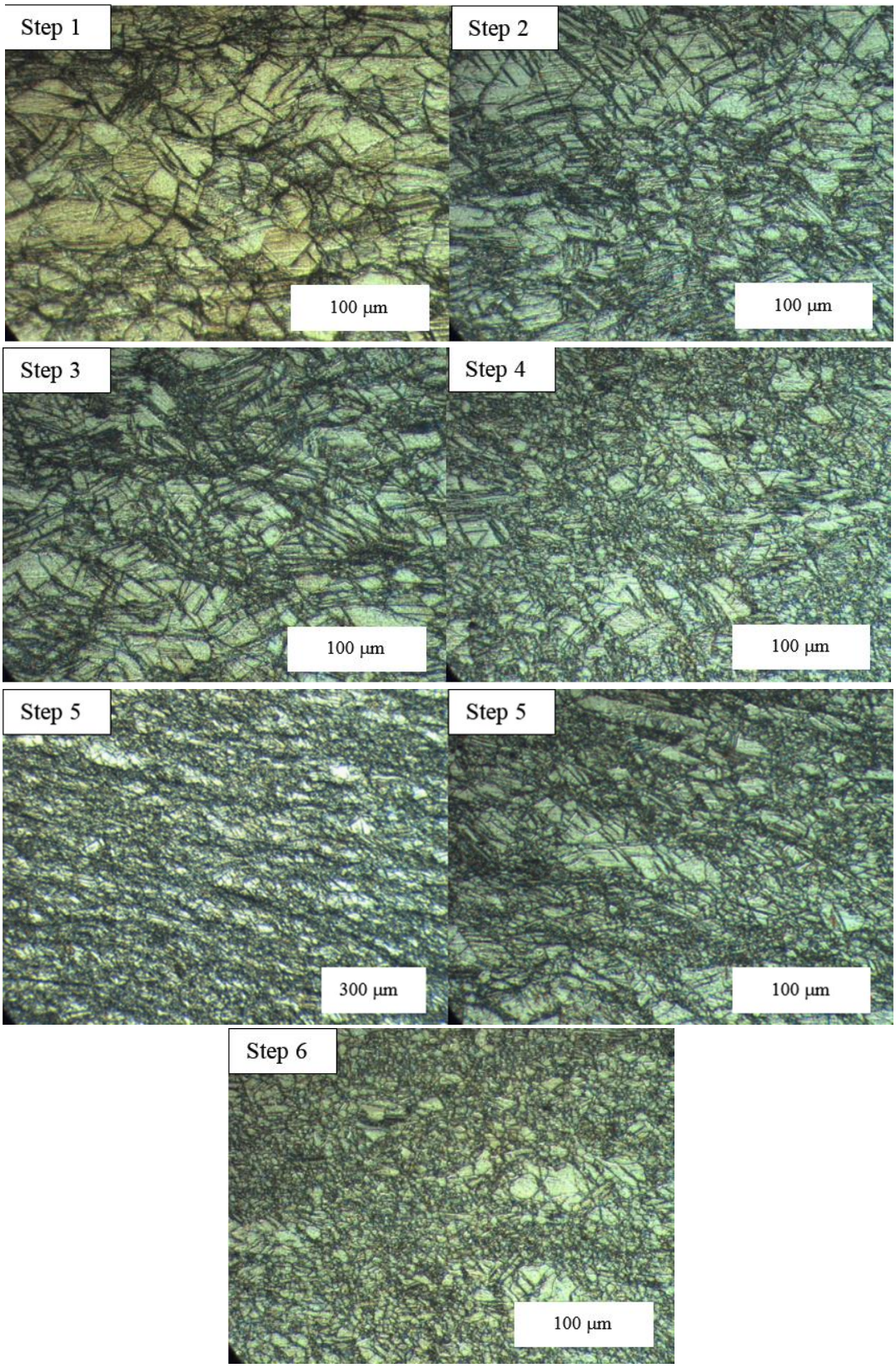


**Figure 4.32** (Continued)

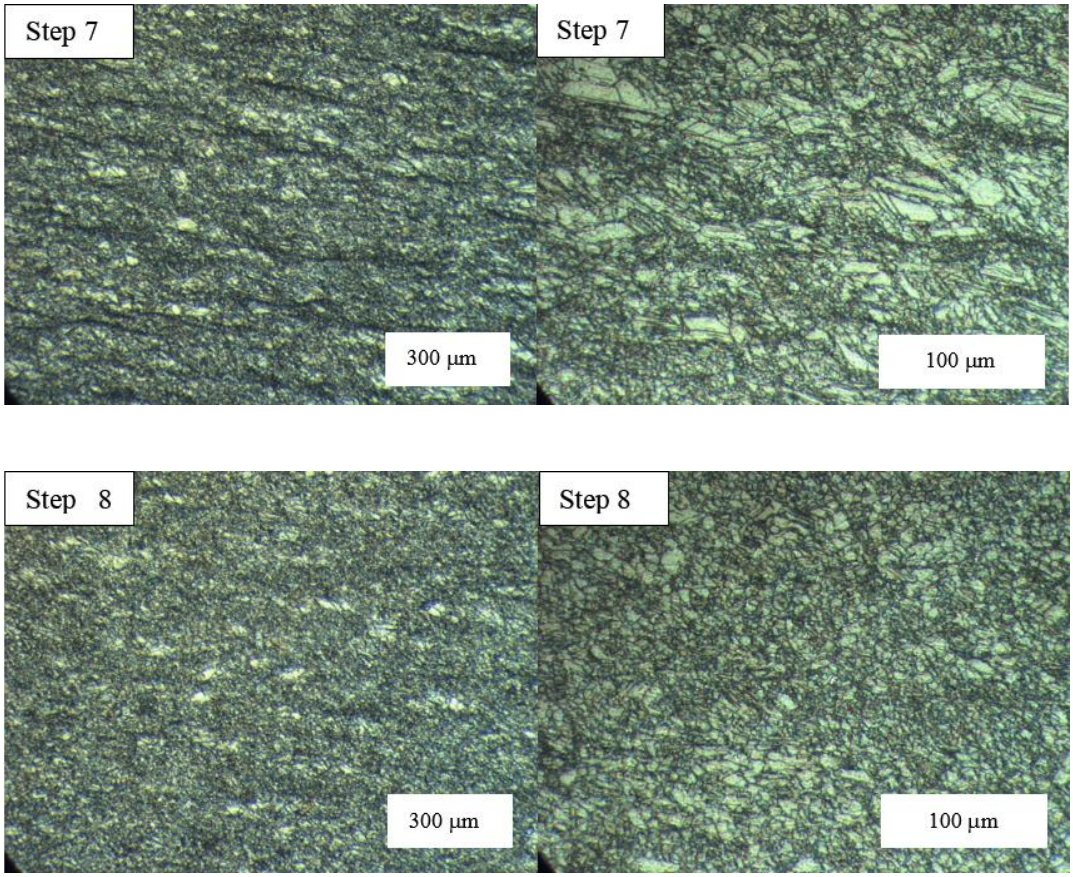


**Figure 4.32** Microstructures of each step of cyclic recrystallization.

When the time efficiency is considered cyclic recrystallization can be found more favorable. Comparing the Figures 4.33 and 4.34, 1 hour of annealing at 200°C was not enough for recrystallization to be completed in a 0.18 rolled sample; however 55 minutes was enough for all the matrix to be fully recrystallized in cyclic recrystallization. By the use of this method, since complete recrystallization can be achieved, more deformation could be applied and grain refinement was accomplished with a more homogeneous final grain size distribution.

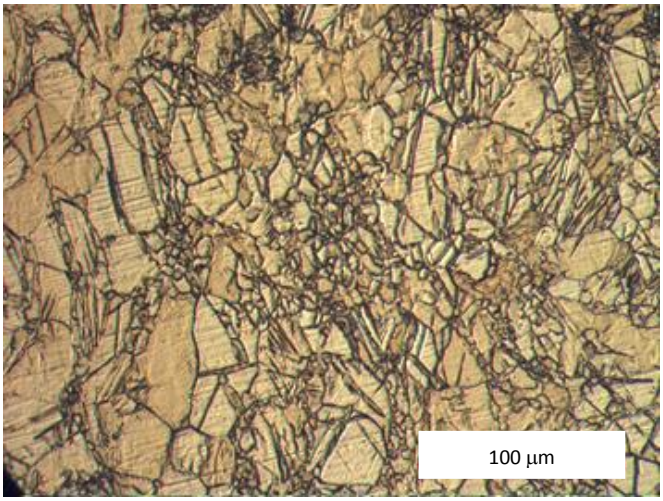


**Figure 4.33** Sample rolled to 0.18 strain value, annealed at 200°C for 1 hour and not got fully recrystallized (x200). Due to grain growth and also incomplete recrystallization, microstructure and grain size were not homogeneous.

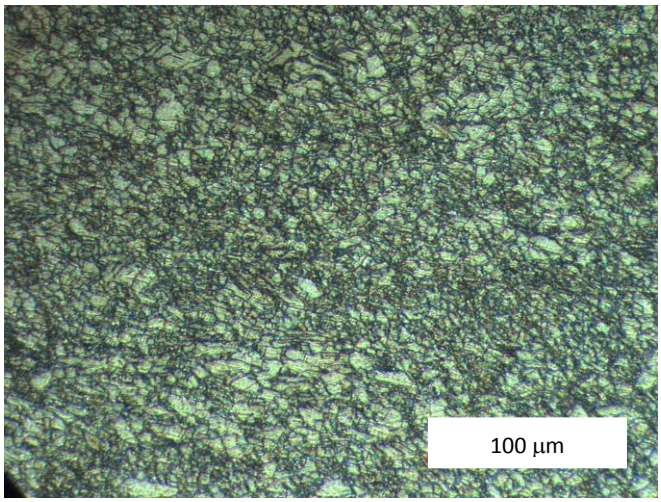


**Figure 4.34** Complete recrystallization after cycles of 0.18 strain + 200°C 10 min + 0.1 strain+ 200°C 15 min + 0.1 strain + 200°C 15 min + 0.1 strain + 200°C 15 min (x200). Total of 0.48 strain was obtained. Grain size was homogeneous.

### 4.5. Examinations on Swaged Samples

#### 4.5.1. Microstructure

Swaged microstructure was different from that of rolled in terms of twin structures, deformed grain shapes and nuclei of recrystallization. While rolled microstructure consisted of fewer and more straight, sharp twins; swaged microstructure was filled with twins with less straight features or even curved twins at certain places. Signs of deformation can be seen in swaged samples as if the grains had a completely twinned texture. Apart from the twinning, distortion of the grains are more pronounced compared to rolled grains. Figure 4.35 represents examples of the swaged microstructures.

The most apparent feature of swaged microstructure is the newly recrystallized nuclei inside the formerly generated twins, at the grain boundaries and in certain samples inside the grains. One of the reasons of this behavior can be the adiabatic heat generated during the swaging processes. Increasing the temperature of the sample might have triggered the recrystallization by supplying enough activation energy for new nuclei to form. Another reason can be the relatively higher strain values attained with swaging due to mold diameters and initial sample diameters; deformation lower than 0.1 was not applicable. As a result, higher amounts of stored deformation energy might have decreased the necessity to reach to higher temperatures in order to initiate the recrystallization. Heat generated during swaging or the deformation amount was sufficient to start nucleation.

Micrographs in Figure 4.35 show the microstructures of samples swaged to 0.1, 0.22, 0.63 and 0.69 true strain values where the strain is calculated according to Equation 3.1.

Comparisons of samples with different strain levels reveal two main features. First one is the increase in twin fraction, second one is the increasing number of recrystallized nuclei as the deformation increases. Nuclei were preferentially located inside the twinned areas, grain boundaries but in highly deformed samples nuclei

were also present in the grain interiors. Nucleation can be seen in Figures 4.36, 4.37 and 4.38.

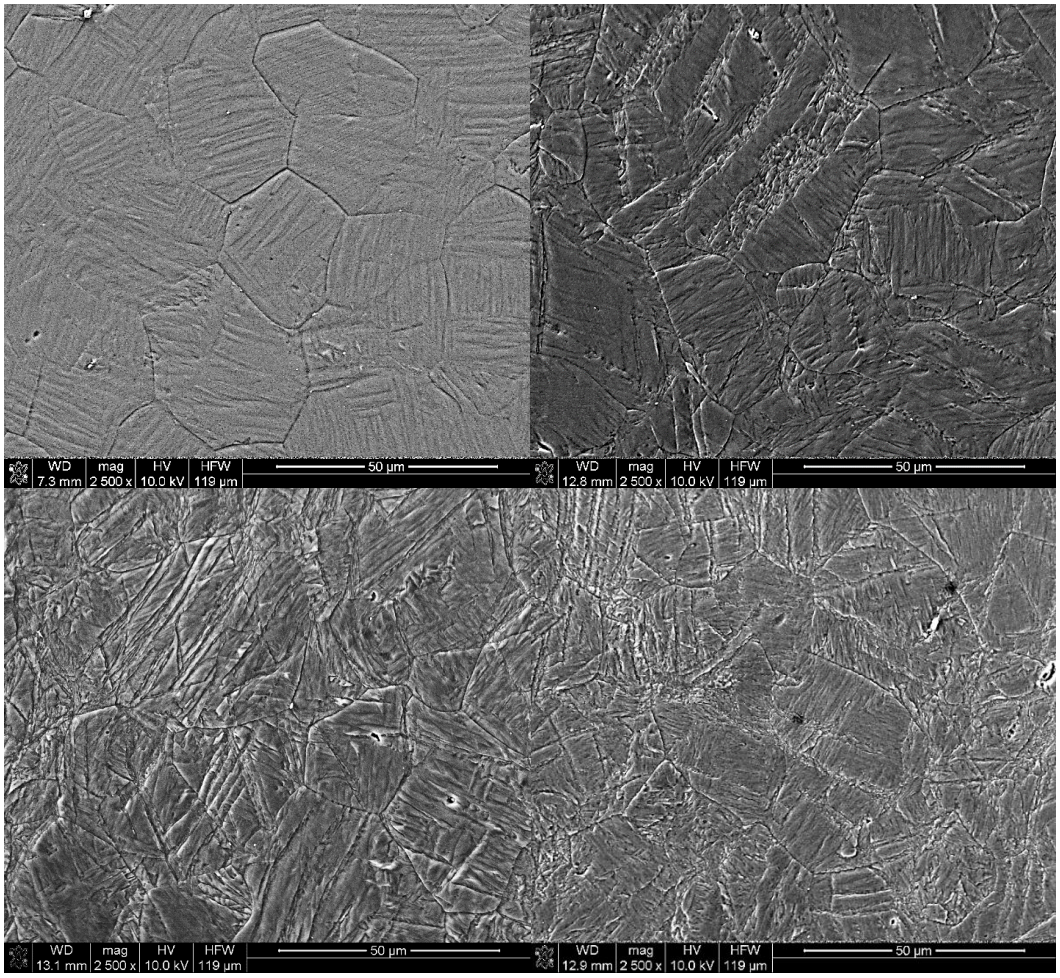


**Figure 4.35** Swaged samples to 0.1, 0.22, 0.63 and 0.69 strain levels.

Average diameter of new nuclei inside the twins in a 0.22 swaged sample given in Figure 4.36 was 450.1 ± 79.4 nm. Figure 4.37.a is a closer view of the interior of a twinned region, which is filled with recrystallized nuclei, a common feature of the microstructure. Figure 4.38 and 4.39 also show twinning and nucleation after different strain levels.

Twinning being the available deformation mechanism other than the basal slip system at the room temperature, it creates new orientations in the twinned regions

which are more suitable for new slip systems. Extra available and active slip systems helped the deformation to continue in these newly oriented (twinned) regions, increased their dislocation density and the stored energy so that the interior parts of the twins were ready for nucleation, preferentially. Nucleation was also seen in grain boundaries as it can be expected since they are preferential sites in regular recrystallization cases even when there is no prominent twinning.

In some grains the interior parts had also nuclei even though there was not an apparent twinning to accomodate nucleation inside it. Figure 4.37.b has few examples of such a case.

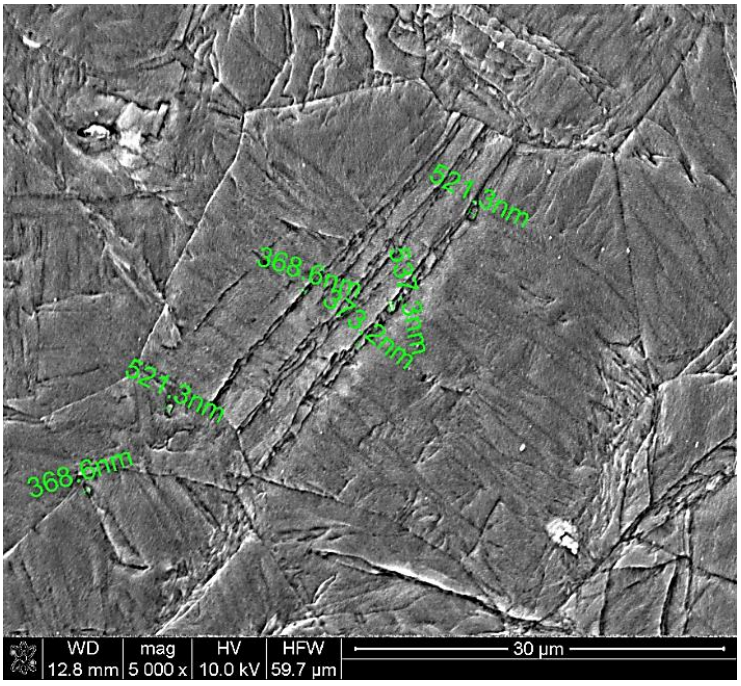


**Figure 4.36** Recrystallized nuclei inside twins, measurements are the diameters of the randomly selected nuclei.

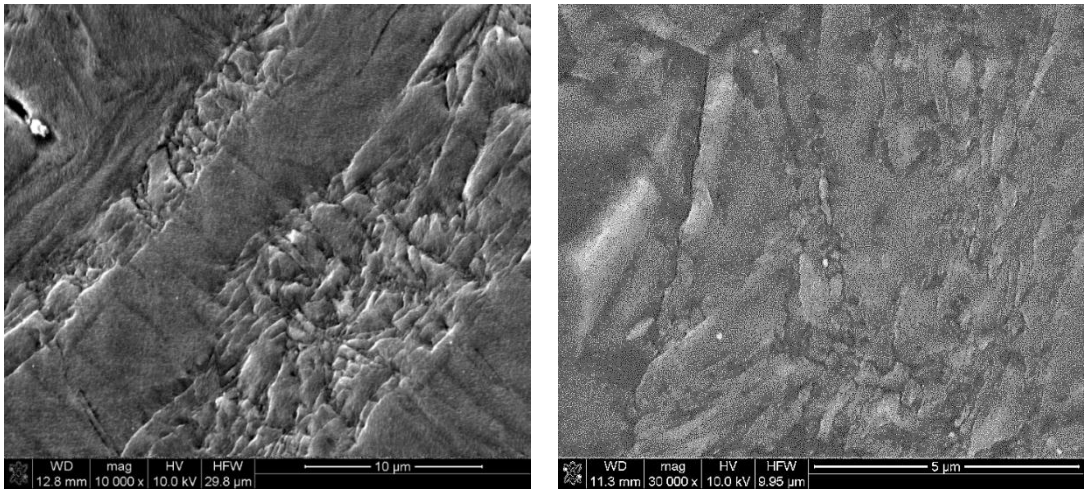


**Figure 4.37** a) Nuclei inside twins and b) nuclei inside the grain and at the grain boundary in the sample after 0.22 strain.

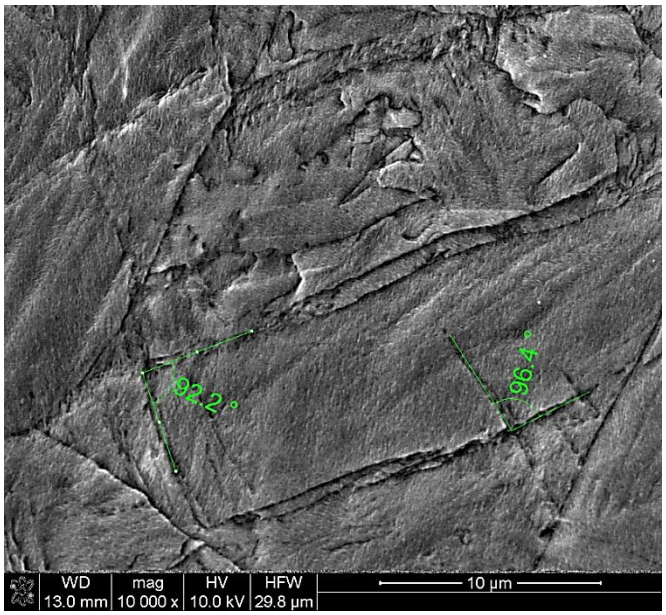


**Figure 4.38** Swaged samples to 0.22 strain, micrograph showing the twins and recrystallized nuclei.

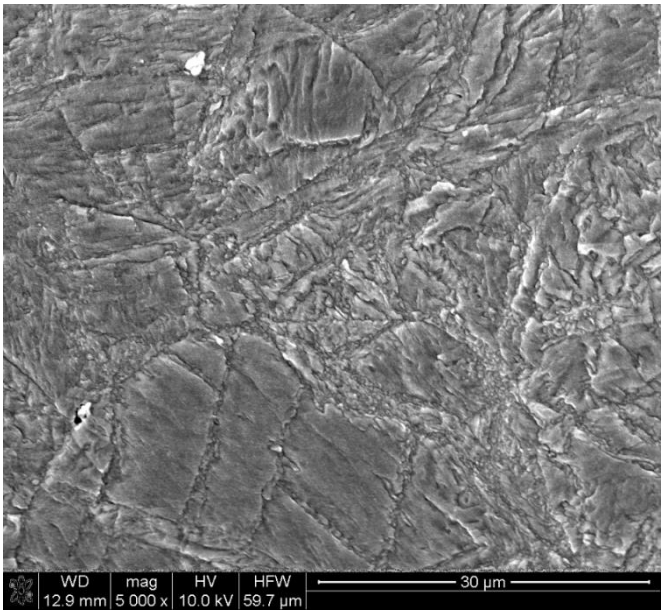


**Figure 4.39** Sample swaged to 0.69 strain. Highly increased number of recrystallized nuclei are occupying the structure.

Samples swaged to 0.63 and 0.69 strain both had cracks inside. Thus the mentioned strain values were not precise, they rather represent the observable dimension/shape change without considering the samples' deformability limit and the generated cracks. Those two swaging processes were above the samples' deformability limit.

Throughout this study, areas with highest density of new nuclei were taken as the areas subjected to the highest deformation.

### 4.5.2. Hardness

Rolling and swaging both resulted in hardening of the samples, however swaged samples had higher hardness values at all deformation values as it can be seen in Figure 4.40. This behavior can be expected due to the more complex deformation mode in swaging which forces material to deform in a variety of orientations resulting in a highly deformed and as a result strain hardened microstructure.

Since the swaged samples were incapsulated inside Cu pipes during swaging to adjust intermediate strain values other than allowed by the swager dies, complete fracture of the samples were only noticed after the cut-up and sample preparation steps. Cu pipes prevented samples from breaking in to pieces, however it was possible directly to notice crack initiations and interfere and stop the rolling process in rolled samples. Thus hardness data of rolled samples is only up to the strain corresponding to the initiation of fracture.

After approximately 0.36 strain, cracks were observed in almost all samples whether rolled or swaged and after the formation of cracks no further hardening was observed since the deformation energy probably expanded to make the cracks propagate instead of deforming the remaining matrix. Qualitative comparison of rolled or swaged samples after similar strain values show that, swaged microstructure contains higher density of twins.

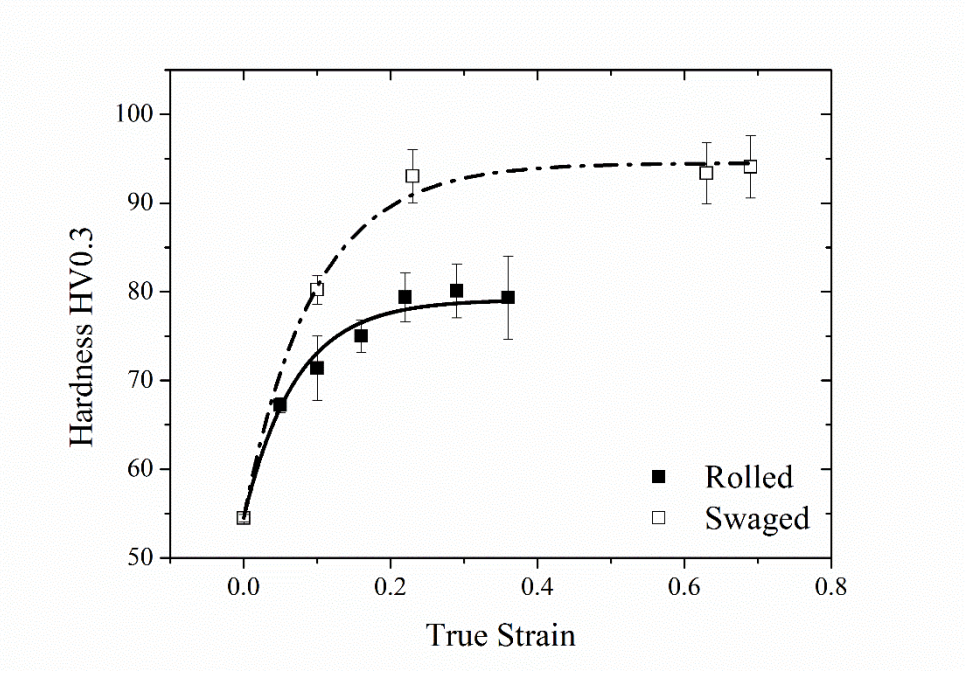


**Figure 4.40** Hardness change with deformation.

While the hardness distribution was almost uniform in rolled samples, swaged samples had a different hardness distribution; in all swaged samples surface hardness values were higher than that of center regions. This variation in hardness was taken as a proof of non-uniform deformation generated by swaging. When swaged samples were annealed, a gradient in the recrystallization fractions between surface and center of the samples was detected. Non-uniform hardness distribution was seen in all swaged samples. While the hardness distribution was similar along the longitudinal axis parallel to the swaging direction, it had a variation between edge and the center when the micro hardness measurements were done at the cross-section perpendicular to the swaging direction.

### 4.5.3. Texture

Texture of the swaged samples were similar to that of extruded AZ31 in literature [52]. Extrusion results in rod like texture where basal planes are aligned parallel to extrusion direction and no diffraction data from basal planes was seen in plane perpendicular to extrusion direction (Figure 2.14 (0002) pole figure for 0% strain). Figure 4.41 a) and b) are diffraction patterns of 0.1 swaged samples. Similar to extruded samples, in Figure 4.41, XRD pattern generated from plane perpendicular to swaging direction showed very small peak for (002) diffraction while an increase in the intensity of (100) and (110) was noticed.

Integrated intensity values for each peak were calculated. When the ratios for $I_{(002)}/I_{(101)}$ versus $(I_{(100)} + I_{(110)})/I_{(101)}$ were normalized with that of powder Mg and compared, it was seen that the calculated ratios in the surface perpendicular to transverse direction (TD) after annealing was closer to the ratios of powder Mg.

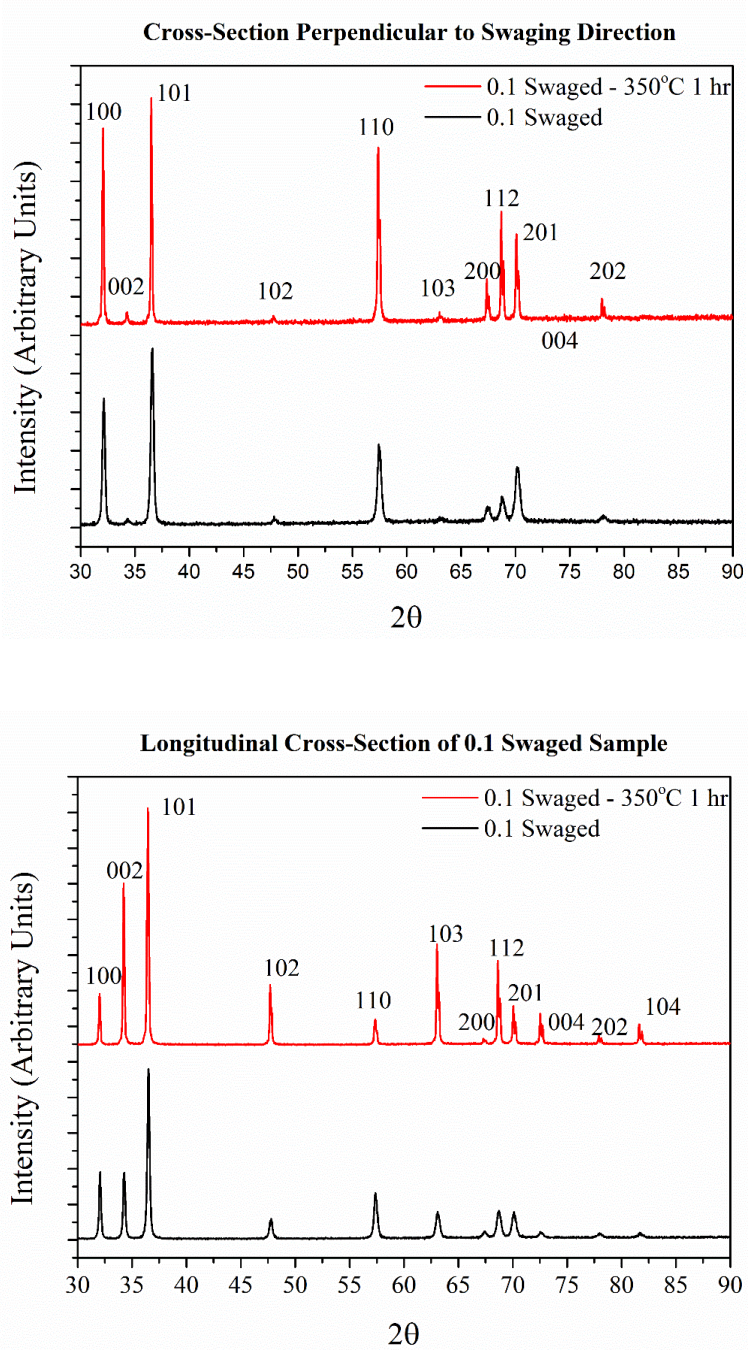


**Figure 4.41** XRD patterns or 0.1 swaged and annealed samples at 350°C for 1 hour. a) Diffraction patterns obtained from surface perpendicular to swaging direction and b) from surface perpendicular to transverse direction.

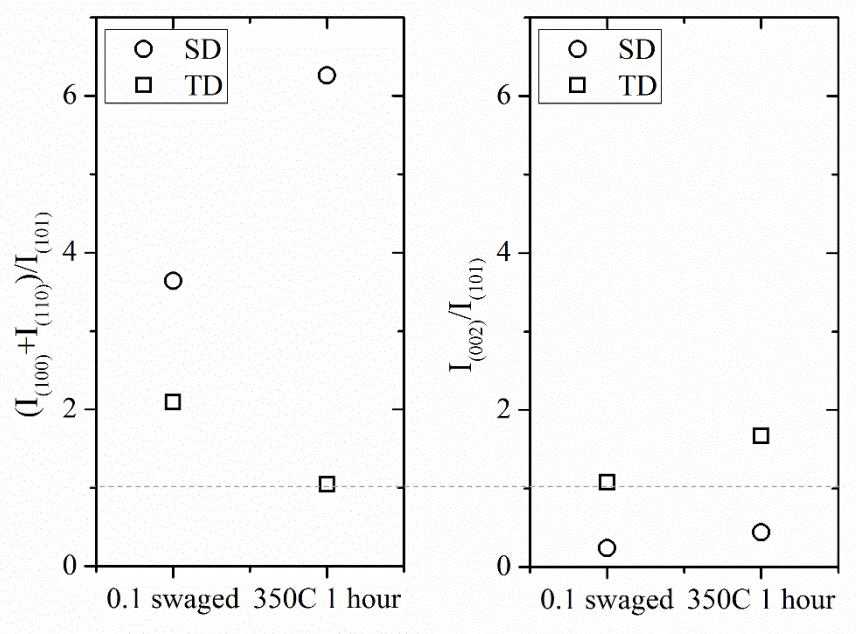


**Figure 4.42** Comparing Integrated and normalized intensity ratios of swaged and annealed samples to that of powder. Horizontal line represents powder data. Circles represent data collected from surface perpendicular to swaging direction (SD), squares represent surface perpendicular to transverse direction (TD)

### 4.5.4. Effect of Non-Uniform Deformation on Recrystallization

Non-uniform deformation due to swaging was detected with micro-hardness measurements and microstructural examinations. Highest hardness values were recorded at areas close to swaged surface, similarly highest nucleation rate was observed at these regions also. While higher hardness values indicate higher strain hardening, higher nucleation rate also shows higher stored energy, both confirm that outer surfaces parallel to swaging direction deforms more than the inner parts of the sample. Average hardness at the center line of the cylindrical 0.1 swaged samples was 85.6 ± 3.7. Hardness variations at the cross-section perpendicular to the swaging direction can be seen in Figure 4.43.

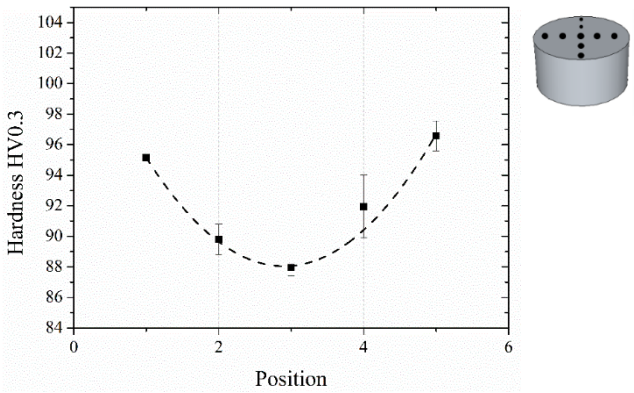


**Figure 4.43** Hardness distribution in the cross-section of a sample swaged to 0.63 strain.

After swaging to 0.1 strain, hardness variation at cross-section perpendicular to swaging direction disappears after 30 minutes at 220°C of annealing. Figure 4.44 shows the hardness distribution from one surface to another as the samples are being annealed. Homogenization of the hardness was completed after 30 minutes, however uniform microstructure in terms of grain size was not attained. Surface of the sample had smaller grain compared to rest of the sample.

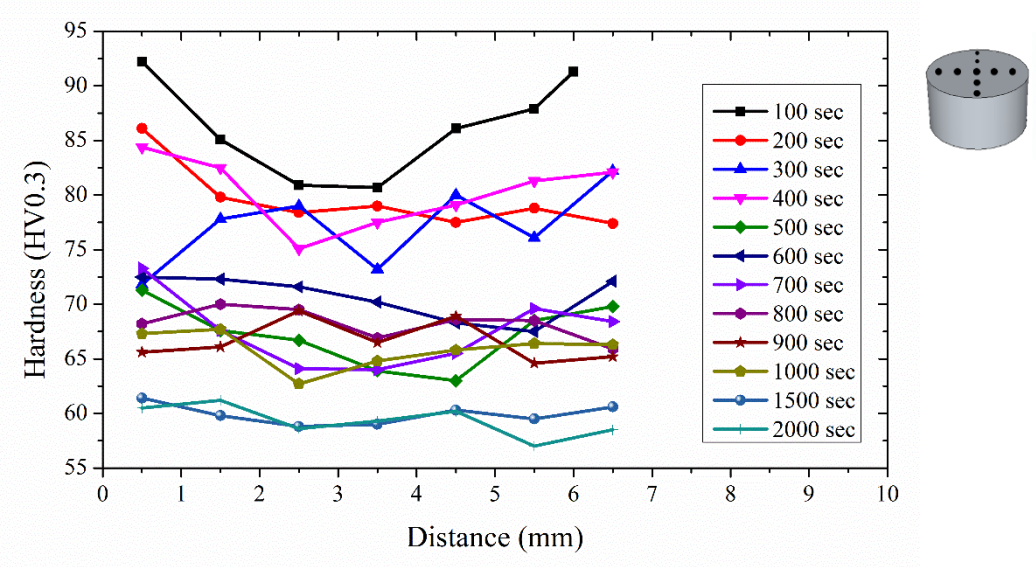


**Figure 4.44** Hardness distribution during recrystallization of 0.1 at 220°C.

Optical microscopy and polarized light microscopy examinations in these regions revealed the difference between recrystallization fraction between surface and core of the sample. As it can be seen in Figure 4.45 due to higher stored energy in highly deformed surface regions, nucleation rate was greater than the core parts of the samples. Figure 4.45 belongs to a sample swaged to 0.1 strain and held at 220°C for 400 seconds (~7 minutes). Polarized light microscopy images show the difference between edge and center parts, while edge contains tiny nuclei, center parts does not seem to show much recrystallization indications.

Non-uniform deformation created by swager enables the observation of different strains and a variety of recrystallization rates on samples. It was clear even by examining one single sample that the highly deformed regions, surface, preserved the completely recrystallized and fine grained structure while low strained regions, center parts have remained partially recrystallized with a wide variety of grain sizes.

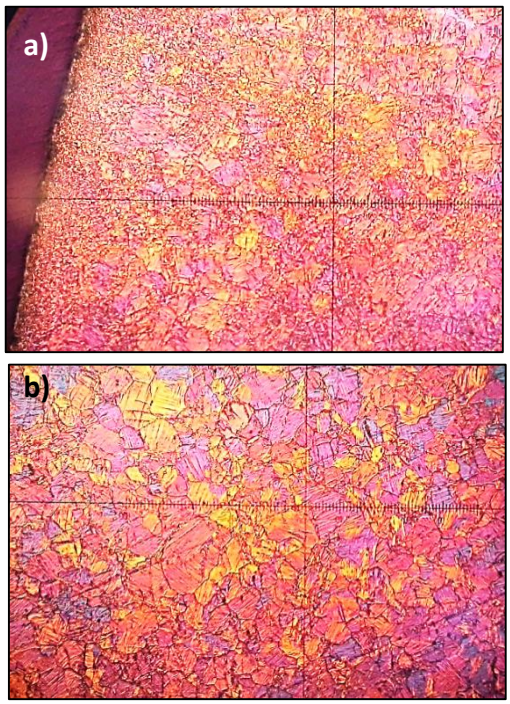


**Figure 4.45** Edge and center microstructure of the same 0.1 swaged samples annealed at 200°C per 400 seconds (both at 50x magnification).

The similar behavior was also seen in the fractured samples. Like hardness variations, localization of large number of nuclei was also an indication of non-uniform deformation. When fractured and annealed samples were examined, locations of tiny nuclei showed the highly strained areas. While regions near the cracks were completely recrystallized; regions far from the cracked zone contained far less number of new nuclei. Since cracks form at places with highest strain concentration, it was expected to see the highest rate of recrystallization at those regions as well.

Swaging caused cracking after approximately 0.22 strain, the area around the cracks probably strained to a degree sufficient for fracture. Figure 4.46 shows one such sample, sample fractured after 0.69 strain, triangular part between the cracks had the smallest grain size measured in this study. Area was filled with new nuclei and the recrystallization was complete. Grain size in this triangle region was 304 ± 39 nm, which was the smallest result recorded during this study.

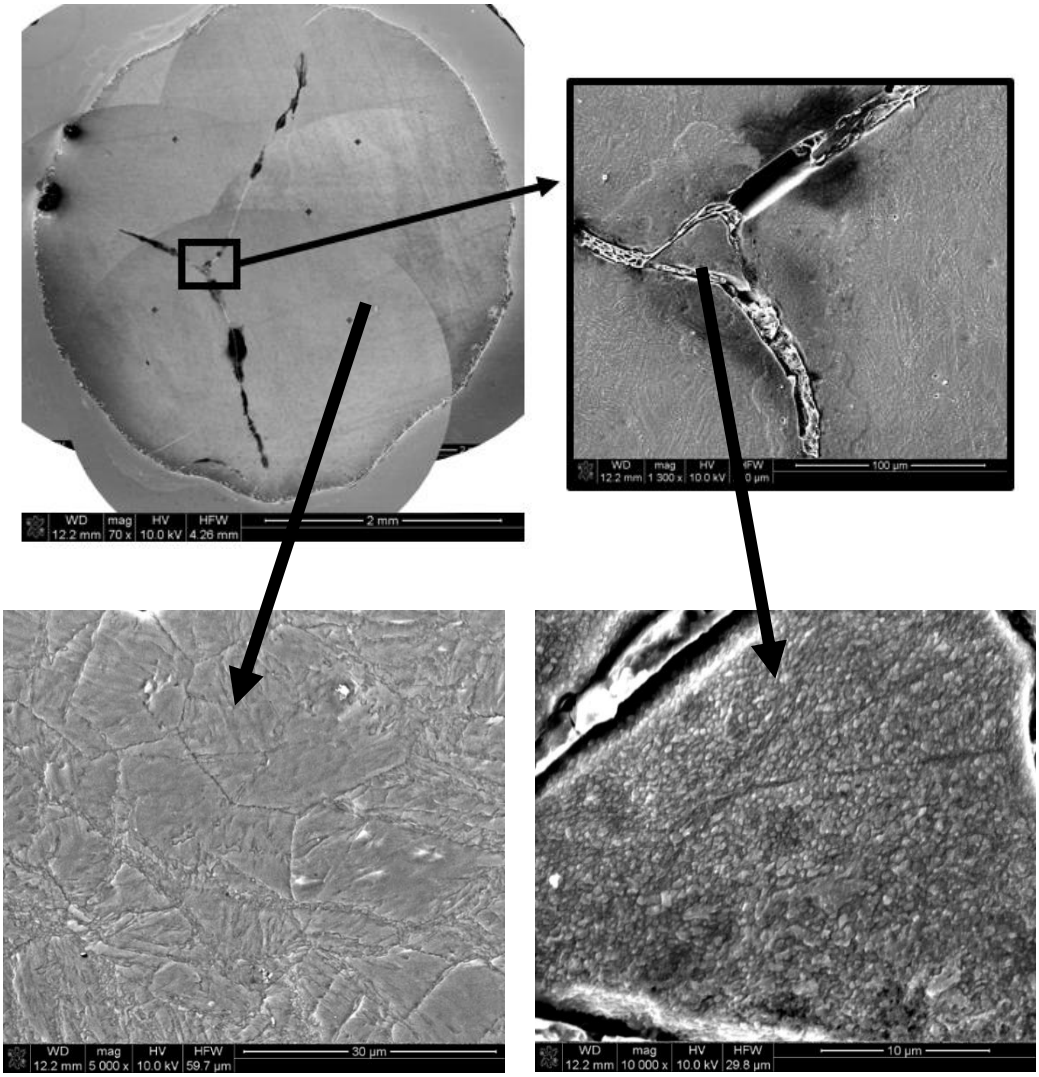


**Figure 4.46** Samples swaged to 0.69 true strain and annealed at 200°C for 3 minutes, effect of different amounts of deformation to recrystallization can be observed.

Areas far from the cracked zones showed partial recrystallization with nuclei inside twins or around grain boundaries.

### 4.5.5. Crack Initiation and Propagation in Swaged Samples

In swaged samples cracks were observed to be generated from the surface mainly. In Figure 4.47, polished and Nital etched surface shows the deformation structure and cracks can be seen in circular cross-section of the swaged sample.

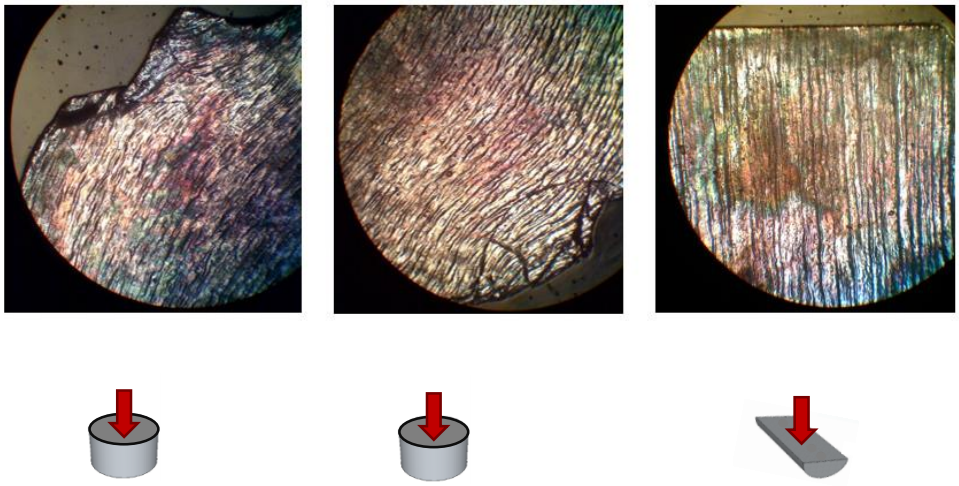

**Figure 4.47** Polished and etched (with 10% Nital) surfaces of samples swaged to 0.63 strain. Crack formations at the surface regions are visible.

In samples which were placed inside Cu pipes, cracks were seen both at the surface and in the center of the sample. Figure 4.48 below shows a sample swaged to 0.63 strain.

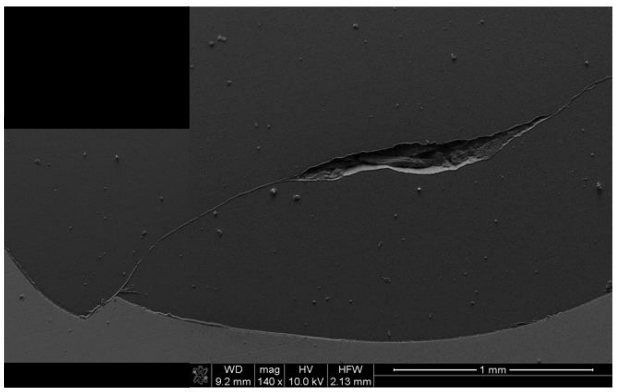


**Figure 4.48** Sample inside Cu pipe, crack with a step at the sample/Cu pipe interface.

In contast to the rolled samples which had an angular relation between crack orientation and rolling direction, no apparent pattern in the crack generation and propagation was observed in swaged samples but in general cracks were mainly generated at the outer surface that was in contact with the swager die and propagated through inner parts of the sample.

### 4.5.6. Recrystallization in As Swaged Samples

Either due to the heat generated during deformation or due to the deformation values that exceeds the critical limits, deformed samples had recrystallized nuclei even in the as deformed states. Similar behavior was also seen in the as rolled samples as well. As a result of this fact again, no incubation period was detected during the recrystallization studies of swaged samples. Nuclei formed during rolling and swaging can be seen in Figure 4.49.

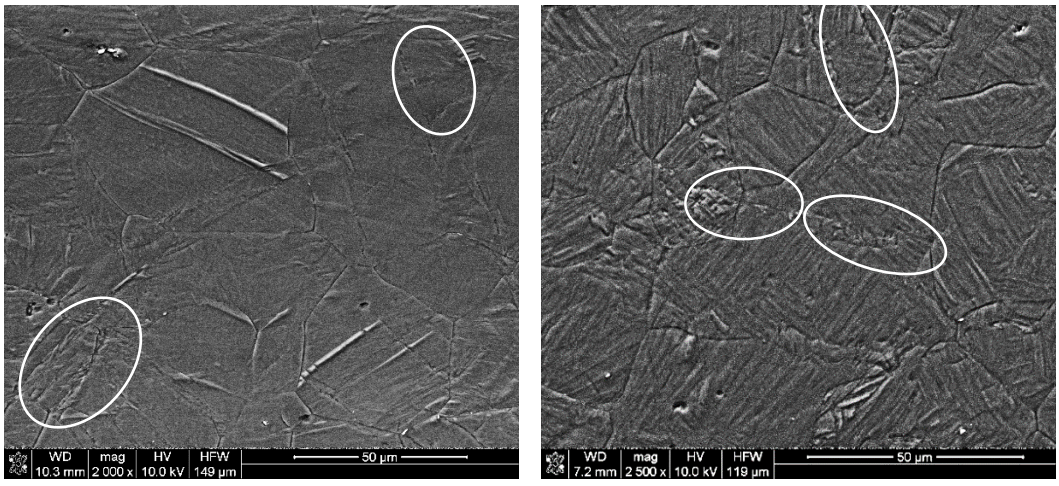


**Figure 4.49** Recrystallization nuclei in 0.1 rolled and swaged samples respectively.

In the 0.22 swaged samples, in which both the effect of higher and more complex multidirectional deformation can be seen, recrystallization was complete in 1 hour even at 200°C. At higher temperatures like 300°C required time for complete recrystallization decreased below 10 minutes. Figures 4.50 and 4.51 show the

sigmoidal and Avrami plots respectively, of swaged samples after being annealed at different temperatures.

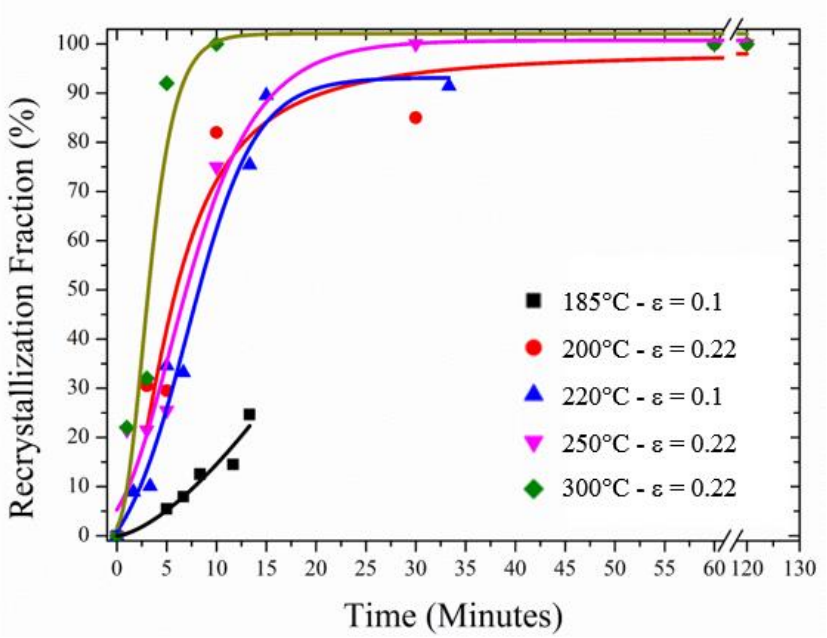


**Figure 4.50** Isothermal transformation graph for the recrystallization of swaged samples. Strain values are given.

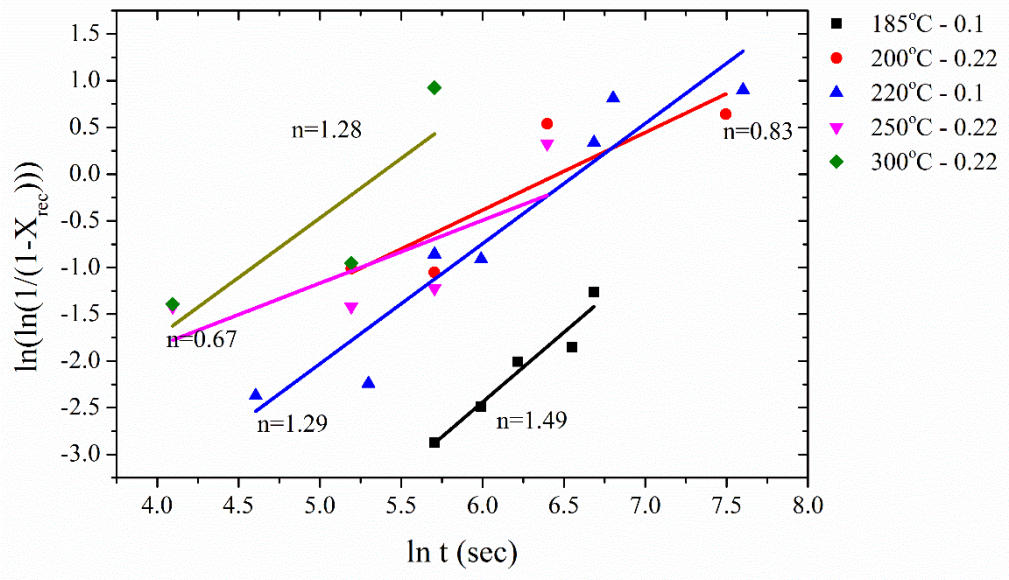


**Figure 4.51** JMAK plot of swaged samples after recrystallization processes at different temperatures. Strain values are given.

Due to the assumptions of Avrami Equation, such as homogeneous nucleation and constant nucleation and growth rate, Sigmoidal and JMAK plots for both rolled and swaged AZ31 samples do not follow regularly expected features. Lower n values than ideal (n=4) case and also the two-step curvature seen in the Avrami plot of rolled samples (Figure 4.25) are two examples to these deviations from regular recrystallization behavior. Such lower n values like 1.5 was also found in other studies in literature [82] as in Figure 4.52 and one of the explanations was the non-random nucleation sites in AZ31 during annealing.

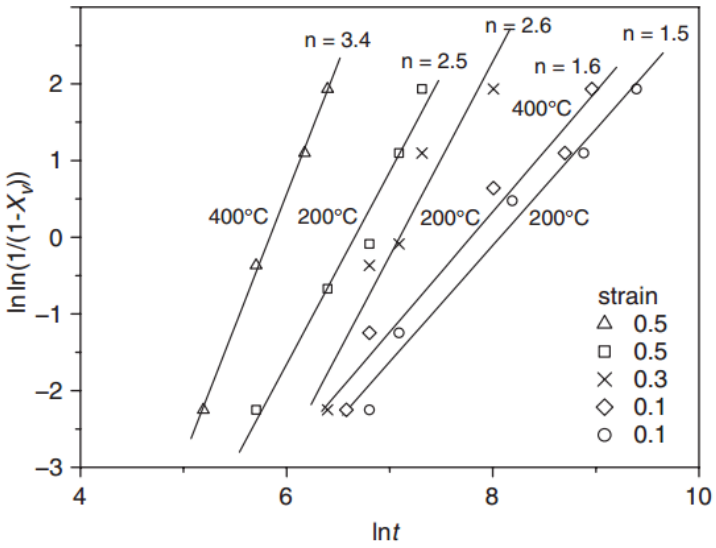


**Figure 4.52** Recrystallization kinetics of AZ31 shown by JMAK plot for isothermal annealing [82].

### 4.6. Swaging and Rolling Comparison

In order to understand the effects of deformation types such as unidirectional or multidirectional, recrystallization data of rolled and swaged samples were compared. While rolled samples were representing the products of unidirectional deformation, swaged samples were representing the products of multidirectional deformation. As expected their recrystallization behaviors were different. Recrystallization fraction versus time data of 0.1 rolled/swaged and annealed (at 185°C and 220°C) samples

were plotted in Figure 4.53. Their linear JMAK plot are also given in Figure 4.54. At 185°C, no big difference between the fraction versus time curves of rolled and swaged samples was observed probably due to low temperature kinetics, however at higher temperatures such as 220°C, the difference in recrystallization rate between rolled and swaged samples were more prominent.

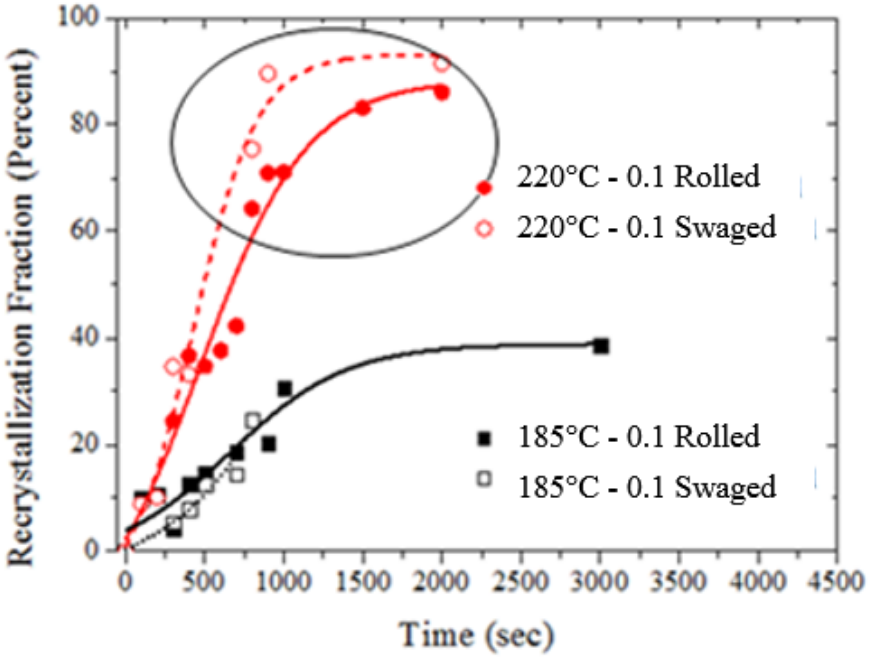


**Figure 4.53** Recrystallization fraction data versus time curves for 0.1 rolled and swaged samples.

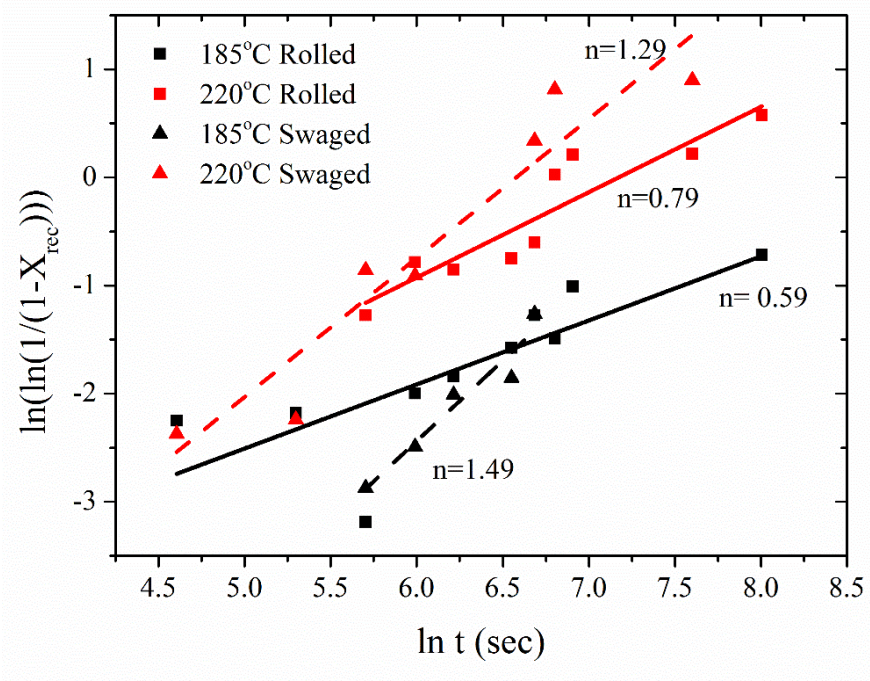


**Figure 4.54** JMAK Plot of 0.1 rolled and swaged samples at 185°C and 220°C.

The effect of deformation mode was more obvious when final microstructures were compared. Figure 4.55 shows the microstructures after approximately 33 minutes in 220°C, in terms of grain size swaged microstructure seems more homogeneous, where un-recrystallized areas are visible in both sample. Figure 4.56 shows the grain size distribution of these two microstructures. While 4% of the grains were larger than 20μm after being swaged and annealed, this ratio was 10% for the rolled and annealed samples.

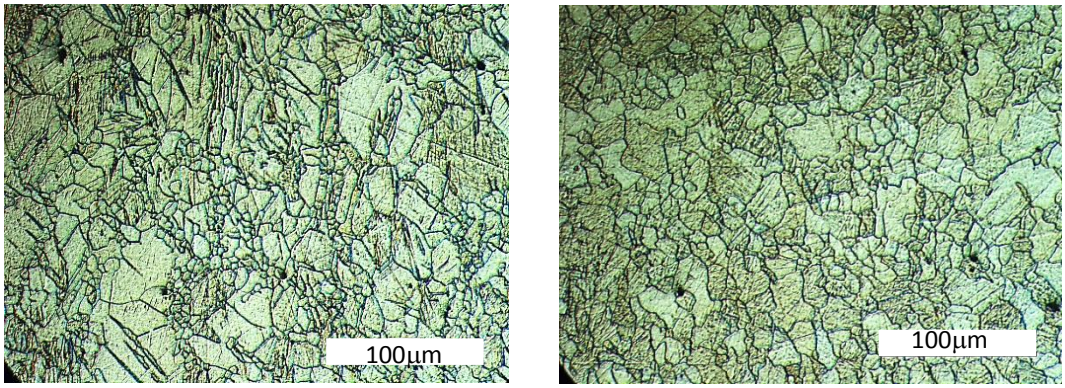


**Figure 4.55** Recrystallization microstructures of samples (a) rolled, (b) swaged to 0.1 strain, after 2000 seconds (~33 min) at 220°C.

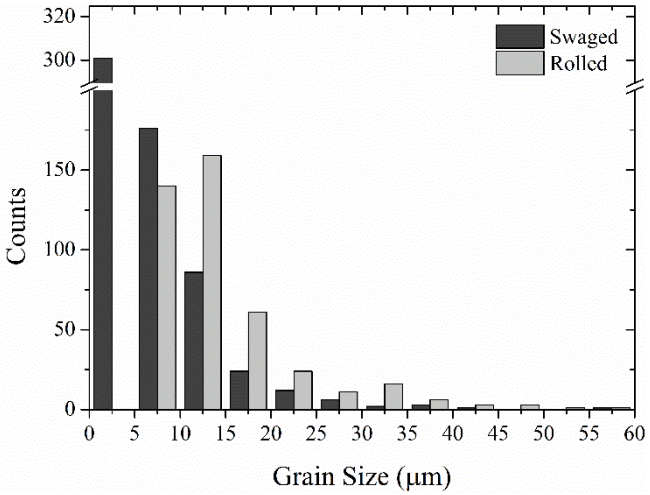


**Figure 4.56** Grain size distribution of the 0.1 rolled and swaged samples given in Figure 4.55.

### 3.10. Schmid Factor Calculations for Twinned Regions

Schmid factor calculations for the deformation mechanisms in magnesium may serve as a guide in determining which mechanisms can be active. Table 2.4 given previously shows the Schmid factor values calculated for magnesium. In order to use this table, loading direction during rolling can be taken as perpendicular to the rolling surface (θ=0-5°) for simplification. In the case where θ in Table 2.4 equals to zero, only pyramidal a+c slip and extension twinning appear to be active since all other Schmid factors are equal to zero; however once the structure is twinned orientation of this twinned region changes and in order to comment on what will happen inside the twins during loading, Re-indexation matrix for Mg given in the study of Niewczas [14] were used. During the calculations flowchart in Figure 4.57 was followed.

Schmid factors for the existing loading direction and for the newly formed twins were calculated. When the 'm' for the deformation mechanisms inside the twins are calculated, an increase in the number of mechanisms with higher Schmid factors is seen. Calculated schmid factors for the twinned regions can be seen in Figure 5.58.

When compared to starting basal texture in which only <c+a> slip and twinning has none zero Schmid factor, these new twinned regions have larger number of potentially active slip/twin mechanisms. As a result of this, increase in the dislocation density and also secondary twinning may be observed inside twins. More thorough texture analysis is required to precisely determine active slip/twin systems for the complete sample. This approximation helps to see that twins, due to their orientation, can deform more than the parent grain in which they form. As it was observed during microstructural examinations, these highly deformed regions, twins, also serve as preferential nucleation sites during annealing of cold deformed AZ31.

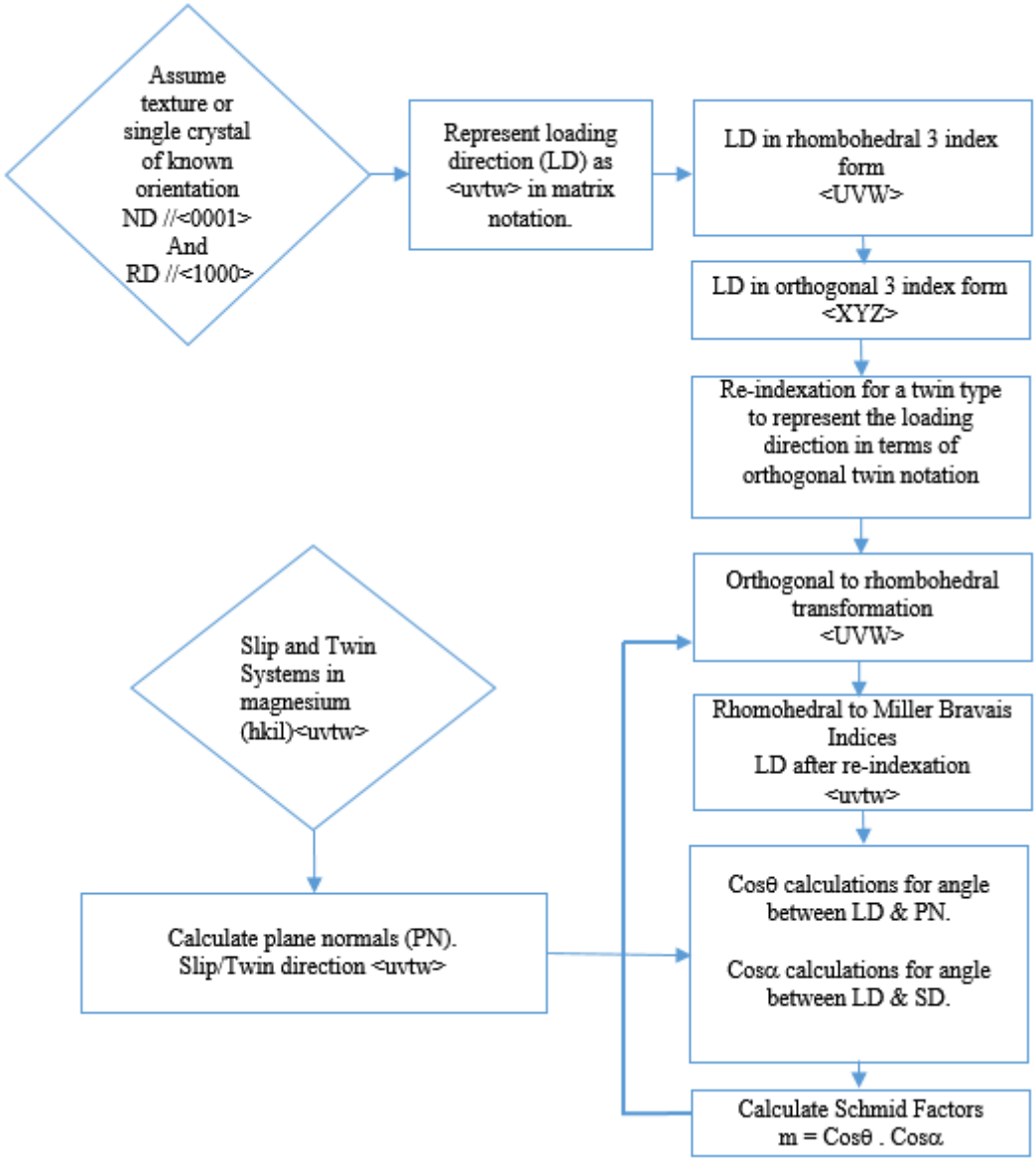


**Figure 4.57** Flowchart for Schmid factor calculations for twin in a crystal. Calculations explained in Appendix.

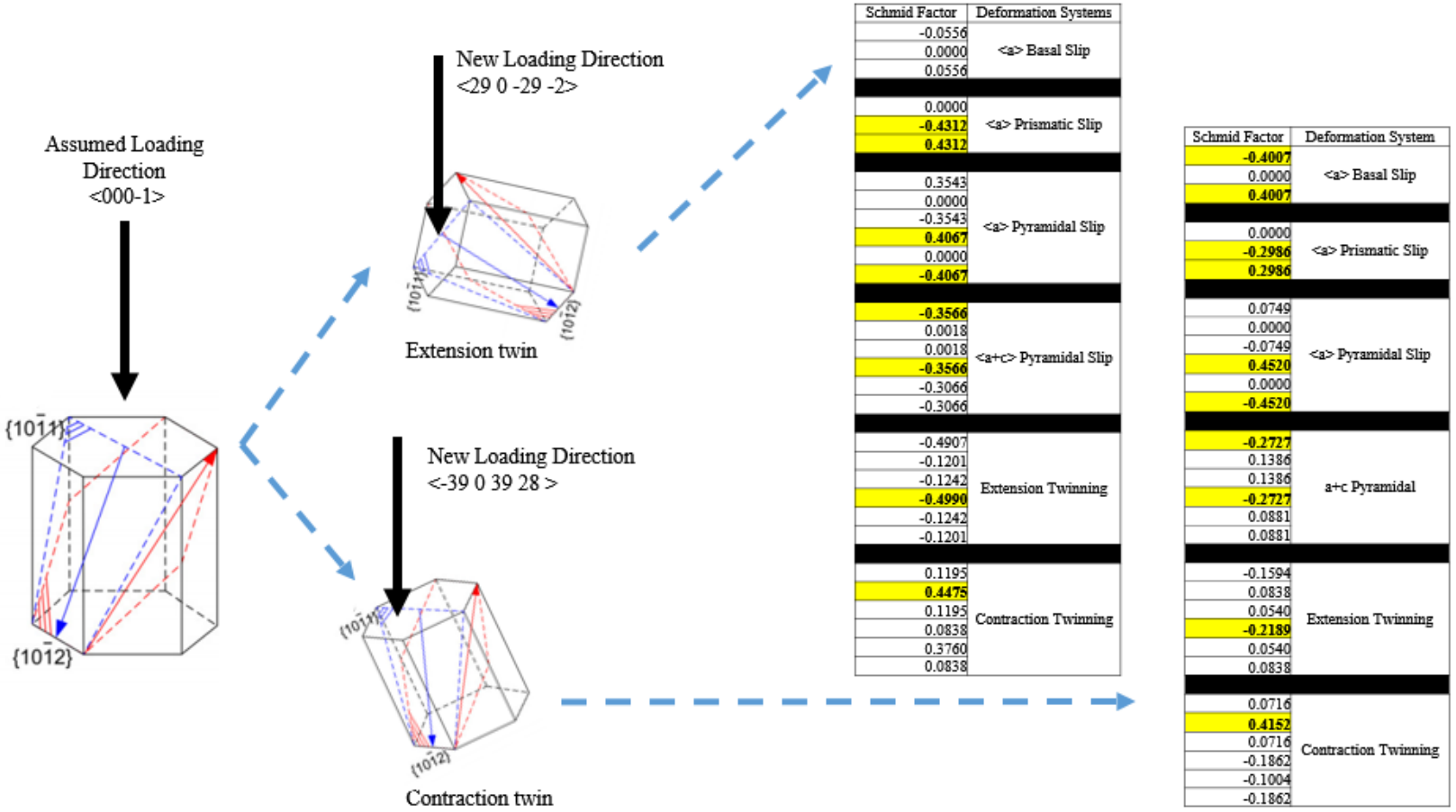


| Schmid Factor | Deformation Systems |
|---|---|
| -0.0556 | <a> Basal Slip |
| 0.0000 | |
| 0.0556 | |
| | |
| 0.0000 | <a> Prismatic Slip |
| **-0.4312** | |
| **0.4312** | |
| | |
| 0.3543 | <a> Pyramidal Slip |
| 0.0000 | |
| -0.3543 | |
| **0.4067** | |
| 0.0000 | |
| **-0.4067** | |
| | |
| **-0.3566** | <a+c> Pyramidal Slip |
| 0.0018 | |
| 0.0018 | |
| **-0.3566** | |
| -0.3066 | |
| -0.3066 | |
| | |
| -0.4907 | Extension Twinning |
| -0.1201 | |
| -0.1242 | |
| **-0.4990** | |
| -0.1242 | |
| -0.1201 | |
| | |
| 0.1195 | Contraction Twinning |
| **0.4475** | |
| 0.1195 | |
| 0.0838 | |
| 0.3760 | |
| 0.0838 | |

| Schmid Factor | Deformation System |
|---|---|
| **-0.4007** | <a> Basal Slip |
| 0.0000 | |
| **0.4007** | |
| | |
| 0.0000 | <a> Prismatic Slip |
| **-0.2986** | |
| **0.2986** | |
| | |
| 0.0749 | <a> Pyramidal Slip |
| 0.0000 | |
| -0.0749 | |
| **0.4520** | |
| 0.0000 | |
| **-0.4520** | |
| | |
| **-0.2727** | a+c Pyramidal |
| 0.1386 | |
| 0.1386 | |
| **-0.2727** | |
| 0.0881 | |
| 0.0881 | |
| | |
| -0.1594 | Extension Twinning |
| 0.0838 | |
| 0.0540 | |
| **-0.2189** | |
| 0.0540 | |
| 0.0838 | |
| | |
| 0.0716 | Contraction Twinning |
| **0.4152** | |
| 0.0716 | |
| -0.1862 | |
| -0.1004 | |
| -0.1862 | |

Figure 4.58 Results of Schmid factor calculations for slip and twin systems (for variants given in Table 2.1 and 2.2). Re-indexation performed for extention and contraction twinning. Yellow cells shows the highest calculated value among variants. HCP figures taken from [13].

# CHAPTER 5

# CONCLUSIONS

1. AZ31 Magnesium alloy was cold rolled and swaged for the investigation of deformation microstructure of the differently deformed states. Rolling represented the unidirectional deformation while swaging represents the more multi directional deformation. Microstructure after swaging was found to be more complex and a larger number of twinning was dominating the microstructure compared to rolling.

2. Strain hardening after both methods was monitored by micro-hardness measurements. Swaging was found to have the highest effect on hardening at the examined interval of deformation levels.

3. After 0.36 true strain, first micro-cracks at the surface and inside the sample were observed in cold rolled samples. 0.22 was the deformation limit to observe first micro-cracks at the surface of the swaged samples. Further deformation did not provide additional strain hardening, hardness was observed to be stable and only crack growth was noticed.

4. Swaging resulted in a highly non-uniform deformation and the effect of this heterogeneous deformation was observed by the difference in hardness distribution and recrystallization fraction variations along the samples. Such variations in hardness or recrystallization fractions were not observed in rolled samples.

5. Recrystallization of cold rolled and swaged samples, deformed to similar strains were compared. Swaged samples had a faster recrystallization kinetics and a final microstructure with finer grain size. Complete recrystallization was not achieved at many cases where unrecrystallized areas remained.

6. Deformation by cold rolling and successive annealing procedures were applied cyclically to sheet samples. Final grain size of 3 micrometers were obtained. Microstructure was homogeneous in contrast to what was obtained from the product of a regular one deformation and an annealing process. Time to reach complete recrystallization was decreased, deformability limit was increased to 0.48 without cracking.

7. Schmid factor calculations were performed to show that due to orientation changes, twins are can deform more than the parent grain in which they form.

## REFERENCES

[1] A.A. Luo, 8 - Applications: aerospace, automotive and other structural applications of magnesium, In Woodhead Publishing Series in Metals and Surface Engineering, edited by Mihriban O. Pekguleryuz, Karl U. Kainer and A. Arslan Kaya, Woodhead Publishing, 2013, Pages 266-316, Fundamentals of Magnesium Alloy Metallurgy, ISBN 9780857090881.

[2] C.L. Mendis and K. Hono, 4 - Understanding precipitation processes in magnesium alloys, In Woodhead Publishing Series in Metals and Surface Engineering, edited by Mihriban O. Pekguleryuz, Karl U. Kainer and A. Arslan Kaya, Woodhead Publishing, 2013, Pages 125-151, Fundamentals of Magnesium Alloy Metallurgy, ISBN 9780857090881.

[3] M.R. Barnett, 6 - Forming of magnesium and its alloys, In Woodhead Publishing Series in Metals and Surface Engineering, edited by Mihriban O. Pekguleryuz, Karl U. Kainer and A. Arslan Kaya, Woodhead Publishing, 2013, Pages 197-231, Fundamentals of Magnesium Alloy Metallurgy, ISBN 9780857090881, http://dx.doi.org/10.1533/9780857097293.197.

[4] B. L. Mordike and T. Ebert: Mater. Sci. Eng. A 302 (2001) 37–45.

[5] J. A. del Valle, M. T. Pe´rez-Prado and O. A. Ruano: Mater. Sci. Eng. A 355 (2003) 68–78.

[6] M. Hakamada, T. Furuta, Y. Chino, Y. Chen, H. Kusuda and M. Mabuchi: Energy 32 (2007) 1352–1360.

[7] R. Neelameggham, 1 - Primary production of magnesium, In Woodhead Publishing Series in Metals and Surface Engineering, edited by Mihriban O. Pekguleryuz, Karl U. Kainer and A. Arslan Kaya, Woodhead Publishing, 2013, Pages 1-32, Fundamentals of Magnesium Alloy Metallurgy, ISBN 9780857090881, http://dx.doi.org/10.1533/9780857097293.1.

[8] Liu, J., Liu, T., Yuan, H., Shi, X., & Wang, Z. (2010). Effect of cold forging and static recrystallization on microstructure and mechanical property of magnesium alloy AZ31. Mater Trans, 51, 341-346.

[9] F. Hollrigl-Rosta, 'Magnesium in Volkswagen', Light Metal Age, 1980 , 22–29.

[10] ASM HandBooks, Alloy Phase Diagrams Vol.3

[11] P. Okrutny, Master's thesis, McMaster University, 2010.

[12] Shenglong Liang, B.Eng. (2012). Deformation and Its Effect on Recrystallization in Magnesium Alloy AZ31, McMaster University, Hamilton, Ontario, Canada.

[13] Nan, X. L., Wang, H. Y., Zhang, L., Li, J. B., & Jiang, Q. C. (2012). Calculation of Schmid factors in magnesium: Analysis of deformation behaviors. Scripta Materialia, 67(5), 443-446.

[14] Niewczas, M. (2010). Lattice correspondence during twinning in hexagonal close-packed crystals. Acta Materialia, 58(17), 5848-5857.

[15] Chang, L. L., Shang, E. F., Wang, Y. N., Zhao, X., & Qi, M. (2009). Texture and microstructure evolution in cold rolled AZ31 magnesium alloy. Materials Characterization, 60(6), 487-491.

[16] J Koike, T Kobayashi, T Mukai, H Watanabe, M Suzuki, K Maruyama, K Higashi, The activity of non-basal slip systems and dynamic recovery at room temperature in fine-grained AZ31B magnesium alloys, Acta Materialia, Volume 51, Issue 7, 18 April 2003, Pages 2055-2065, ISSN 1359-6454, http://dx.doi.org/10.1016/S1359-6454(03)00005-3.

[17] P. Yang , Y. Yu , L. Chen , W. Mao , ' Experimental determination and theoretical prediction of twin orientations in magnesium alloy AZ31 ', Scripta Materialia, 50, 2004 , 1163 –1168.

[18] M. A. Meyers , O. Vohringer , V. A. Lubarda , Acta. Materialia, 49, 2001 , 4025–4032.

[19] M. Masoumi , F. Zarandi , M. Pekguleryuz , Scripta Materialia., 62(11), 2010 , 823–826.

[20] M. Masoumi , F. Zarandi , M. Pekguleryuz , Mater. Sci . Eng. A, 528, 2011 , 1268–1279.

[21] A.A. Kaya, 2 - Physical metallurgy of magnesium, In Woodhead Publishing Series in Metals and Surface Engineering, edited by Mihriban O. Pekguleryuz, Karl U. Kainer and A. Arslan Kaya, Woodhead Publishing, 2013, Pages 33-84, Fundamentals of Magnesium Alloy Metallurgy, ISBN 9780857090881, http://dx.doi.org/10.1533/9780857097293.33.

[22] M.H. Yoo, Metall. Mater. Trans. A 12A (1981) 409.

[23] M.R. Barnett, Z. Keshavarz, A.G. Beer, D. Atwell, Acta Mater. 52 (2004) 5093.

[24] W.H. Hartt, R.E. Reed-Hill, Trans. Metall. Soc. AIME 242 (1968) 1127.

[25] R.E. Reed-Hill, Trans. Metall. Soc. AIME 218 (1960) 554.

[26] L. Jiang, J.J. Jonas, A.A. Luo, A.K. Sachdev, S. Godet, Mater. Sci. Eng.: A 445–446 (2007) 302.

[27] L. Jiang, J.J. Jonas, R.K. Mishra, A.A. Luo, A.K. Sachdev, S. Godet, Acta Mater. 55 (2007) 3899.

[28] H. Miura, G. Yu and X. Yang. Mater. Sci. Eng. A 528 (2011) 6981.

[29] W. C. Liu, X. Y. Li and X. C. Meng. Scripta Materialia 60 (2009) 768–771.

[30] H. Conrad, N. Karam, S. Mannan, Scripta Metal. 18 (1984) 275–280.

[31] S. Sandlobes et al. Acta Materialia 59 (2011) 429–439.

[32] A. Styczynski, Ch. Hartig, J. Bohlen, D. Letzig, Scr. Mater. 50 (2004) 943–947.

[33] W.B. Hutchinson, M.R. Barnett, Effective values of critical resolved shear stress for slip in polycrystalline magnesium and other hcp metals, Scripta Materialia, Volume 63, Issue 7, October 2010, Pages 737-740, ISSN 1359-6462, http://dx.doi.org/10.1016/j.scriptamat.2010.05.047.

[34] S.R. Agnew, Magnesium Technology 2002, TMS Annual Meeting, Seattle, WA, 2002.

[35] S.R. Agnew, C.N. Tome ´, D.W. Brown, T.M. Holden, S.C. Vogel, Scripta Mater. 48 (2003) 1003.

[36] S.R. Agnew, D.W. Brown, C.N. Tome ´, Acta Mater. 54 (2006) 4841.

[37] O. Mura ´nsky, D.G. Carr, M.R. Barnett, E.C. Oliver, P. Sittner, Mater. Sci. Eng. A496 (2008) 14.

[38] M.R. Barnett, Z. Keshavarz, X. Ma, Metall. Mater. Trans. 37A (2006) 2283.

[39] A. Chapuis , J.H. Driver , Acta Materialia, 59, 2011 , 1986–1993.

[40] M.R. Barnett , ‘ Twinning and the ductility of magnesium alloys: Part I: Tension twins ’, Mater. Sci. Eng. A, 1–2(464), 2007 , 1 –7.

[41] J. J. Jonas, S. Mu, T. Al-Samman, G. Gottstein, L. Jiang, E. Martin, ‘ The role of strain accommodation during the variant selection of primary twins in magnesium ’, Acta Materialia, 59, 2011 , 2046 –2056.

[42] H. Li, E. Hsu, J. Szpunar, R. Verma , J. T. Carter , ‘ Determination of active slip/twinning modes in AZ31 Mg alloy near room temperature ’, JMEPEG, 16, 2007 , 321 –326.

[43] Fumiaki Hiura. Master’s thesis, McMaster University, 2010.

[44] D.W. Brown , S.R. Agnew , M.A.M. Bourke , T.M. Holden , S.C. Vogel , C.N. Tom é , ‘Internal strain and texture evolution during deformation twinning in magnesium ’, Mater. Sci. Eng. A, 399(1–2), 2005 , 1 –12.

[45] S.R. Agnew , D.W. Brown , C.N. Tom é , ‘ Validating a polycrystal model for the elasto-plastic response of magnesium alloy AZ31 using in-situ neutron diffraction ’, Acta Materialia, 54(18), 2006 , 4841 –4852.

[46] S.R. Agnew , C.N. Tom é , D.W. Brown , T.M. Holden , S.C. Vogel , ‘ Study of slip mechanisms in a magnesium alloy by neutron diffraction and modelling ’, Scripta Materialia, 48(8), 2003 , 1003 –1008.

[47] O. Mur á nsky , M.R. Barnett , D.G. Carr , Acta Materialia, 58, 2010 , 1503–1517.

[48] M.R. Barnett , Z. Keshavarz , A.G. Beer , D. Atwell , ‘ Influence of grain size on the compressive deformation of wrought Mg–3Al–1Zn ’, Acta Materialia, 52, 2004 , 5093 –5103.

[49] J.Koike, Metall. Mater. Trans. A-Phys. Metall. Mater. Sci. 36A (2005) 1689.

[50] T. Kobayashi, J. Koike, Y. Yoshida, S. Kamado, M. Suzuki, K. Maruyama, and Y. Kojima: J. Jpn. Inst. Met., 2003, vol. 67, p. 149

[51] O. Mur á nsky , D.G. Carr , P. Š ittner , E.C. Oliver , ' In situ neutron diffraction investigation of deformation twinning and pseudoelastic-like behaviour of extruded AZ31 magnesium alloy ', Int. J. Plasticity, 25, 2009 , 1107 –1127.

[52] Clausen, B., Tomé, C. N., Brown, D. W., & Agnew, S. R. (2008). Reorientation and stress relaxation due to twinning: modeling and experimental characterization for Mg. Acta Materialia, 56(11), 2456-2468.

[53] M.F.Ashby, Philos. Mag. 21 (1970) 399.

[54] F.E. Hauser, P.R. Landon, J.E. Dorn, Trans. AIME 206 (1956) 589.

[55] Jain, A., Duygulu, O., Brown, D. W., Tomé, C. N., & Agnew, S. R. (2008). Grain size effects on the tensile properties and deformation mechanisms of a magnesium alloy, AZ31B, sheet. Materials Science and Engineering: A, 486(1), 545-555.

[56] M.R.Barnett, Scripta Materalia, 59, 2008, 696-698.

[57] N.Hansen, Scripta Materalia, 51, 2004, 801-806.

[58] Beer, A. G., & Barnett, M. R. (2008). Microstructure evolution in hot worked and annealed magnesium alloy AZ31. Materials Science and Engineering: A, 485(1), 318-324.

[59] Lu, L., Liu, T., Tan, M. J., Chen, J., & Wang, Z. (2012). Effect of annealing on microstructure evolution and mechanical property of cold forged magnesium pipes. Materials & Design, 39, 131-139.

[60] M.R. Barnett, Mater. Trans. 44 (2003) 571–577.

[61] Galiyev, R. Kaibyshev, Mater. Sci. Forum 467–470 (2004) 1175–1180.

[62] R. Kawalla, N. Coung, A. Stolnikov, 6th International Conference Magnesium Alloys and Their Applications, Wiley-VCH, 2004, pp. 803–810.

[63] A. Yamamoto, et al., Mater. Sci. Forum (2004) 669–672.

[64] M. Eddahbi, et al., Mater. Sci. Eng. A 410–411 (2005) 308–311.

[65] E. Essadiqi, C. Galvani, V. Kao, 2nd International Light Metals Technology Conference, LKR, St. Wolfgang, Austria, 2005, pp. 155–160.

[66] N. Chetty , M. Weinert , ‘ Stacking faults in magnesium ’, Physical Review B, 56 (17), 1997 , 844 –851.

[67] A.E. Smith , ‘ Surface, interface and stacking fault energies of magnesium from first principles calculations ’, Surface Science, 601, 2007 , 5762 –5765.

[68] L. Wen , P. Chen , Z.-F. Tong , B.-Y. Tang , L.-M. Peng , W.-J. Ding , ‘ A systematic investigation of stacking faults in magnesium via first-principles calculation ’, Eur. Phys. J. B, 72, 2009 , 397 –403.

[69] H.Y. Wang , N. Zhang , C. Wang , Q.C. Jiang , ‘ First-principles study of the generalized stacking fault energy in Mg–3Al–3Sn alloy ’, Scripta Materialia, 65, 2011 , 723 –726.

[70] T. Uesugi , M. Kohyama , M. Kohzu , M. Higashi , ‘ Generalized stacking fault energy and dislocation properties for various slip systems in magnesium: a first-principles study ’, Materials Science Forum, 419 –422, 2003 , 225 –230.

[71] D. K. Sastry , Y.V.R.K. Prasad , K.I. Vasu , ‘ On the stacking fault energies of some cph Metals ’, Scripta Met., 3, 1969 , 927 –933.

[72] A. Couret , D. Caillard , ‘ An in situ study of prismatic glide in magnesium. II. Microscopic activation parameters ’, Acta Metall., 33, 1985 , 1455 –1462.

[73] Liang, S., Okrutny, P., Wang, X., & Zurob, H. (2012, July). Recrystallization Nucleation Sites in Deformed AZ31. In Proceedings of the Mg2012: 9th International Conference on Magnesium Alloys and their Applications, Vancouver, Canada (Vol. 9, pp. 663-668).

[74] T. Al-Samman , G. Gottstein , ‘ Dynamic recrystallization during high temperature deformation of magnesium ’, Mater. Sci. Eng. A, 490, 2008 , 411 –420.

[75] S.W. Xu , K. Oh-ishi , S. Kamado and T. Honma , ‘Twins, recrystallization and texture evolution of a Mg–5.99Zn–1.76Ca–0.35Mn (wt.%) alloy during indirect extrusion process, Scripta Materialia, 65, 2011 , 875–878.

[76] R. Ye Lapovok, M.R. Barnett, C.H.J. Davies, J. Mater. Proc. Technol. 146 (2004) 408–414.

[77] Jain, A., Duygulu, O., Brown, D. W., Tomé, C. N., & Agnew, S. R. (2008). Grain size effects on the tensile properties and deformation mechanisms of a magnesium alloy, AZ31B, sheet. Materials Science and Engineering: A, 486(1), 545-555.

[78] Clausen, B., Tomé, C. N., Brown, D. W., & Agnew, S. R. (2008). Reorientation and stress relaxation due to twinning: modeling and experimental characterization for Mg. Acta Materialia, 56(11), 2456-2468.

[79] R. Gehrmann, M.M. Frommert, G. Gottstein, Mater. Sci. Eng. A 395 (2005) 338–349

[80] Del Valle, J. A., & Ruano, O. A. (2008). Influence of texture on dynamic recrystallization and deformation mechanisms in rolled or ECAPed AZ31 magnesium alloy. Materials Science and Engineering: A, 487(1), 473-480.

[81] JUST LIKE A CLOCKWORK. (n.d.). Retrieved August 17, 2014, from http://www.felss.com/article/just-like-a-clockwork/

[82]Su, C. W., Lu, L., & Lai, M. O. (2008). Recrystallization and grain growth of deformed magnesium alloy. Philosophical Magazine, 88(2), 181-200.

# APPENDIX

## Lattice Correspondence in HCP Crystals

(Summarized from**:** M. Niewczas, "Lattice correspondence during twinning in hexagonal close-packed crystals", http://dx.doi.org/10.1016/j.actamat.2010.06.059)

When twinning occurs, the parent crystal is sheared to a new orientation determined by the operating twinning mode. The crystallographic relationship between parent and twin is described uniquely by the correspondence matrix: each vector or plane in the parent lattice is related unambiguously to a corresponding vector or plane in the twinned lattice

For numerical computations involving the hcp lattice, it is convenient to express the four-index Miller–Bravais indices of crystallographic planes and directions in terms of a three-index hexagonal Miller indices, which then represented by three-index orthogonal coordinate system and to carry out all computations in terms of the orthogonal system, performing the desired computations, and re-indexing into M-B hexagonal indices.

The forward and reverse transformation of indices of crystallographic planes and directions form hexagonal to rhombohedral to orthogonal coordinate systems are as follows:

Consider an arbitrary direction R with Miller–Bravais indices [u v t w] in hexagonal crystal system defined with respect to four basis vectors $a_1$, $a_2$, $a_3$, c can be expressed in a rhombohedral system defined with three basis vectors $a_1$, $a_2$, c using three-index Miller notation [U V W] such that:

$$R = ua_1 + va_2 + ta_3 + wc \quad \text{and} \quad R = Ua_1 + V\,a_2 + W\,c \tag{A.1}$$

The hexagonal [u v t w] and rhombohedral [UVW] indices satisfy following transformation relations between these axes systems:

$U = u - t \qquad V = v - t \qquad W = w$

$$u = 1/3\,(2U - V) \qquad v = 1/3\,(2V - U) \qquad t = -(u + v) \qquad w = W \tag{A.2}$$

The Miller–Bravais indices (h k i l) of a crystallographic plane n in hexagonal crystal system and Miller indices (HKL) of the same plane in rhombohedral axis system are expressed as components of a reciprocal vector defined with respect to the four reciprocal basis vectors of hexagonal crystal system or three reciprocal basis vectors of romboherdral lattice such that:

$$N \equiv g_{hkil} \equiv ha_1^* + ka_2^* + ia_3^* + lc^*$$

and

$$n \equiv g_{HKL} \equiv HA_1^* \; KA_2^* + LC^* \tag{A.3}$$

Here, $a_1^*$; $a_2^*$; $a_3^*$ and $c^*$ are reciprocal basis vectors for hexagonal system $a_1$, $a_2$, $a_3$, c and $A_1^*$; $A_2^*$; $C^*$ are reciprocal basis vectors for rhombohedral system $a_1$, $a_2$, c. The direct and reciprocal basis vectors in hexagonal and rhombohedral axis system, satisfy reciprocity conditions:

$a_i * a_j^* = \delta_{ij}$ i; j = 1 , 4 and $a_i * A_j^* = \delta_{ij}$ ; i , j = 1; 3, where $\delta_{ij}$ is Kronecker delta.

The Miller–Bravais and Miller indices of a plane in hexagonal and rhombohedral axis system satisfy following relations:

$H = h \qquad K = k \qquad L = l$

$$h = H \qquad k = K \qquad i = -(h + k) \qquad l = L \tag{A.4}$$

If the vector R belongs to the plane n, than in any reference system, the plane and the vector must satisfy orthogonality conditions, i.e.

$$R * n = 0 \;\text{ or }\; uh + vk + ti + wl = 0 \quad \text{and} \quad UH + VK + WL = 0. \tag{A.5}$$

The transformation from the rhombohedral $a_1$, $a_2$, c to orthonormal x, y, z coordinate system in which subsequent calculations are carried out (Figure A.1), is done by means of a transformation matrix A:

$$A = \begin{pmatrix} 1 & 1/2 & 0 \\ 1 & \sqrt{3}/2 & 0 \\ 0 & 0 & c/a \end{pmatrix}$$

where c and a are lattice parameters of the hexagonal lattice.

Indices of a vector R[xyz]_[x y z] in orthonormal x, y, z coordinate system are obtained by coordinate transformation of indices of a vector R[UVW] ≡ [U V W] in rhombohedral system such that:

$$R_{[xyz]} = R_{[U\ V\ W]} \qquad (A.6)$$

A is a transformation matrix from rhombohedral to orthonormal system, $R_{[xyz]}$ and $R_{[U\ V\ W]}$ are column vectors. Similarly, the indices of a plane $n_{[xyz]}$ ≡ (x y z) in orthonormal x, y, z coordinate system are obtained by coordinate transformation of indices of plane

$$n[HKL] \equiv (H\ K\ L) \quad \text{such that:} \quad n_{(xyz)} = n_{(HKL)}\, A^{-1} \qquad (A.7)$$

$A^{-1}$ is the inverse of the matrix A, whereas $n_{(xyz)}$ and $n_{(HKL)}$ are row vectors.

After transformation to x, y, z system, the vector $R_{[xyz]}$ and the plane $n_{(xyz)}$ must satisfy orthogonality conditions

$$R_{[xyz]} * n_{(xyz)} = 0. \qquad (A.9)$$

The reversible transformations of a vector and a plane from orthonormal to rhombohedral system are done as follows:

$R_{[UVW]} = A^{-1} R_{[xyz]}$ and $N_{(HKL)} = n_{(xyz)} A$ (A.10)

Calculation of an angle between vectors or planes in hexagonal lattice is required in Shmids factor calculations.The direction given by Miller–Bravais indices [u v t w] is the Cartesian four-dimensional vector v with components v = [u, v, t,λw]. Similarly, normal of a crystallographic plane given by Miller–Bravais indices (h k i l) is the Cartesian fourdimensional vector p with components p = [u, v, t, w/λ], where λ = (c/a)(2/3)$^{1/2}$, c and a are lattice parameters of hexagonal unit cell. Normals and reciprocals are related by relations:

□uvtw□□□□□hkil□□□□□hkil $\lambda^{-2}$□ and (hkil) = (uvtw)* = (uvt$\lambda^2$w) (A.11)

The angle Θ between two four-dimensional vectors is given by the standard formula

(A.12)

$$\cos(\boldsymbol{r_1} * \boldsymbol{r_2}) = \frac{\boldsymbol{r_1}}{|\boldsymbol{r_1}|} * \frac{\boldsymbol{r_2}}{|\boldsymbol{r_2}|} = \frac{\boldsymbol{u_1u_2 + v_1v_2 + t_1t_2 + \lambda^2 w_1w_2}}{\left(\boldsymbol{u_1^2 + v_1^2 + t_1^2 + \lambda^2 w_1^2}\right)^{1/2}\left(\boldsymbol{u_2^2 + v_2^2 + t_2^2 + \lambda^2 w_2^2}\right)^{1/2}}$$

the angle between the line direction $\mathbf{r_1}$ =□$u_1$ $v_1$ $t_1$ $w_1$□□and normal to plane $\mathbf{p_1}$ =□$h_1$ $k_1$ $i_1$ $l_{11}$□□is

(A.13)

$$\cos(\boldsymbol{r_1} * \boldsymbol{p_1}) = \frac{\boldsymbol{r_1}}{|\boldsymbol{r_1}|} * \frac{\boldsymbol{p_2}}{|\boldsymbol{p_2}|} = \frac{\boldsymbol{u_1h_1 + v_1k_1 + t_1i_1 + w_1l_1}}{\left(\boldsymbol{u_1^2 + v_1^2 + t_1^2 + \lambda^2 w_1^2}\right)^{1/2}\left(\boldsymbol{h_1^2 + k_1^2 + i_1^2 + \lambda^{-2} l_1^2}\right)^{1/2}}$$

When the load is applied with the direction of $\mathbf{r_1}$, the slip plane of $\mathbf{p_1}$ , slip direction of $\mathbf{r_2}$ **,** Schmid factor is given by equation.

(A.14)

$$\mathbf{SF} = \cos(\boldsymbol{r_1} * \boldsymbol{r_2}) \ \mathbf{x} \cos(\boldsymbol{r_1} * \boldsymbol{p_1}) = \frac{\boldsymbol{r_1}}{|\boldsymbol{r_1}|} * \frac{\boldsymbol{r_2}}{|\boldsymbol{r_2}|} = \frac{\boldsymbol{r_1}}{|\boldsymbol{r_1}|} * \frac{\boldsymbol{p_1}}{|\boldsymbol{p_1}|} =$$

$$\frac{\boldsymbol{u_1u_2 + v_1v_2 + t_1t_2 + \lambda^2 w_1w_2}}{\left(\boldsymbol{u_1^2 + v_1^2 + t_1^2 + \lambda^2 w_1^2}\right)^{1/2}\left(\boldsymbol{u_2^2 + v_2^2 + t_2^2 + \lambda^2 w_2^2}\right)^{1/2}} \boldsymbol{x}$$

$$\frac{\boldsymbol{u_1h_1 + v_1k_1 + t_1i_1 + w_1l_1}}{\left(\boldsymbol{u_1^2 + v_1^2 + t_1^2 + \lambda^2 w_1^2}\right)^{1/2}\left(\boldsymbol{h_1^2 + k_1^2 + i_1^2 + \lambda^{-2} l_1^2}\right)^{1/2}}$$

Type I twinning shear, as in the case of extension and contraction twins in magnesium, is accomplished by the homogeneous deformation of a crystal lattice described by a deformation gradient tensor in the form

S = | | | |
|---|---|---|
| $1 + sm_1n_1$ | $sm_1n_2$ | $sm_1n_3$ |
| $sm_2n_1$ | $1 + sm_2n_2$ | $sm_2n_3$ |
| $sm_3n_1$ | $sm_3n_2$ | $1 + sm_3n_3$ |

(A.15)

where s is the magnitude of the twinning shear, m = $[m_1,m_2,m_3]$ the twinning direction, and n = $[n_1,n_2,n_3]$ is the normal to the twinning plane K1. During twinning shear the volume of the material is unchanged and the determinant of the deformation gradient matrix S is 1.

Any vector $u_M$ = [u1,u2,u3] defined with respect to the orthogonal system in the parent lattice is sheared to the vector $v_M$ = [v1, v2, v3] in the same lattice, according to the linear transformation relation:

$$v_M = S \ u_M \tag{A.16}$$

where $u_M$ and $v_M$ denote column vectors and S is a 3 x 3 matrix built from the components of the second rank deformation tensor, all expressed with reference to the parent axis system. The transformation given by Eq. A.16. is affine, i.e., after

deformation collinear points remain collinear and coplanar lines remain coplanar. The peculiar feature of the twinning shear applied to the vector $u_M$ is that the sheared product vector, $v_M$, is located in the new twin lattice, defined by the new basis system.

The re-indexation matrix can also be devised from a general form of a three-dimensional rotation matrix around arbitrary direction q = [q1,q2,q3] and arbitrary angle Θ, given by:

(A.17)

$$R_{3D} = \begin{bmatrix} q_1^2(1-\cos\Theta)+\cos\Theta & q_1q_2(1-\cos\Theta)-q_3\sin\Theta & q_1q_3(1-\cos\Theta)+q_2\sin\Theta \\ q_1q_2(1-\cos\Theta)+q_3\sin\Theta & q_2^2(1-\cos\Theta)+\cos\Theta & q_2q_3(1-\cos\Theta)-q_1\sin\Theta \\ q_1q_3(1-\cos\Theta)-q_2\sin\Theta & q_2q_3(1-\cos\Theta)+q_1\sin\Theta & q_3^2(1-\cos\Theta)+\cos\Theta \end{bmatrix}$$

In our case the rotation axis q = [$q_1$,$q_2$,$q_3$] is the normal to the K1 plane and Θ, the rotation angle of a parent lattice around q required to obtain a twin lattice, is 180˚. In this formulation the re-indexation matrix reads:

(A.18)

$$U = \begin{bmatrix} -1+2q_1^2 & 2q_1q_2 & 2q_1q_3 \\ 2q_1q_2 & -1+2q_2^2 & 2q_2q_3 \\ 2q_1q_3 & 2q_2q_3 & -1+2q_3^2 \end{bmatrix}$$

The re-indexation matrix allows any vector or plane in the parent lattice to be expressed as its corresponding representation in the twin lattice. Thus, components of arbitrary vector $b_M$ or arbitrary plane $n_M$ of the parent, are expressed in the twin lattice by means of the re-indexation transformation such that:

(A.19)

$$b_T = U\, b_M$$

and

(A.20)

$$n_T = n_M\, U^{-1}$$

$b_T$ and $b_M$ are column vectors, whereas $n_T$ and $n_M$ are row vectors.
(-1 0 1 2)[1 0 -1 1] twinning mode in Mg is recognized from the 86.31 missorientation between parent and twin obtained by considering the angle between c-axis in the parent and c-axis in the twin, i.e., the angle between [0001] and its associate vector [29 0 29 -2]. The latter vector being $[0001]_M$ re-indexed in the twin lattice by means of Equation A.19. and the re-indexation matrix.
Comparing Equations A.15 and A.16 it is evident that

(A.21)

$$v_T = U\, S\, u_M = C\, u_M$$

It is now evident that vector $v_T$ in the twinned lattice is directly related to the original vector $u_M$ in the parent crystal through the correspondence matrix, C, and the linear transformation relation (A.21). Similarly, any crystallographic plane $n_M$ in the parent lattice is related to a plane $n_T$, in the twinned lattice according to relation

(A.22)

$$n_T = n_M\, C^{-1}$$

as before, $v_T$ and $u_M$ are column vectors and $n_T$ and $n_M$ are row vectors. Deformation, re-indexation and correspondence matrices are all unimodular, i.e., their determinant is unity. This means that a shear, a rotation, or a shear followed by rotation, produced by operation of these matrices on the crystal lattice, preserves the crystal volume. For conventional twinning modes associated with the rational twinning elements, the correspondence matrix is equal to its inverse .

Tables 2a–2d in [14] provide explicit forms of deformation, reindexation, and correspondence matrices for different twinning modes in Mg.

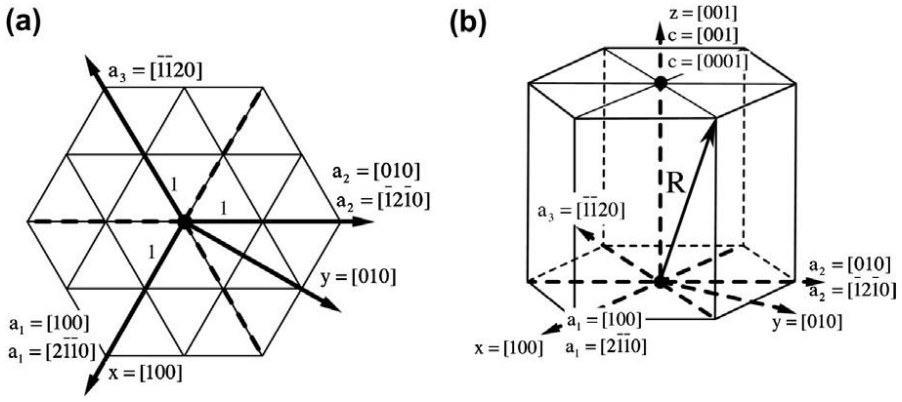


**Figure A1**. Relation between hexagonal $a_1$, $a_2$, $a_3$, c, rhombohedral $a_1$, $a_2$, c, and orthogonal x, y, z coordinate axis system in planar (a) and perspective view (b). Components of the vector R in (b) defined with respect to hexagonal, rhombohedral and orthonormal basis vectors are: R = [1, 1,-2, 1], R = [1, 1, 1] and R = [1,√3,2c/a].